Design and Fabrication of Optomechanical Formalin Fixation Monitoring Systems Integrated with a Millifluidic Device

Saniel Lim

A dissertation

submitted in partial fulfillment of the

requirements for the degree of

Doctor of Philosophy

University of Washington

2020

Supervisory Committee:

Eric J. Seibel, Chair

Ashley F. Emery

Gador M. Canton

Program Authorized to Offer Degree:

Mechanical Engineering

University of Washington

Abstract

Design and Fabrication of Optomechanical Formalin Fixation Monitoring Systems Integrated with a Millifluidic Device

Saniel D. Lim

Chair of the Supervisory Committee:
Eric J. Seibel
Mechanical Engineering

Engineering design is a multi-step process and becoming more challenging when it comes to a translational system that requires new information framework for interdisciplinary fields such as medicine. The translational research is initiated from identifying a clinical niche and followed by conceptual design, simulation, prototyping, preliminary experiments, evaluation, and future design suggestion. In this dissertation, two independent projects for the design and development processes of translational opto-mechanical systems are presented to suggest a feasible medical device design, which can benefit clinical workflow and performance. The first project (Chapter 2, 3, and 4) is to develop a tissue quality monitoring system for an automated millifluidic system for pathology and the development cycle includes design, fabrication, testing, and evaluation of the systems. In our lab, a novel automated millifluidic system for cancer diagnosis using core needle biopsy (CNB)

was under development to overcome the clinical needs in the conventional tissue preparation which are time and labor consuming. The millifluidic system for CNB will automate tissue preparation and imaging processes more rapidly and reliably with all-in-channel millifluidic flowing and non-contact monitoring systems. Especially, the formalin fixation step that is the most time consuming but less known tissue preparation step should be well assessed. The three primary aims are presented for this first project.

The first aim was to design a low-cost but efficient SW elastography device for the CNB submerged in a millifluidic chamber, which simulates the process for the automated CNB microfluidic device. We choose the low-cost and less complicated laser speckle imaging (LSI) technique for SW visualization and velocity measurement, and the SW-LSI system consisting of a 532nm laser, a piezo-actuator and a camera was constructed for this study. The stiffness changes of phantoms and chicken breast tissues during formalin fixation are investigated for different sizes of the samples. We present the distinct temporal change of the tissue's mechanical property by formalin fixation, where the plateau of the fixation level is shown within the time range of optimal fixation time in histopathology.

The second aim was to evaluate the optical property of CNB by formalin fixation over time. This study was originated from the speculation of the prior study, where the visualization of CNB was greatly altered during formalin fixation. We performed a preliminary study of optical attenuation measurement for CNB using a broadband light source and spectroscopy. The relative optical attenuation changes of gelatin-based tissue phantom and various porcine tissues were evaluated. The optical attenuation data in broadband spectrum demonstrated different effects of fixation for various tissues.

The third aim was to fabricate the 3D printed prototype of the optical attenuation monitoring station. For an effective unsophisticated configuration, a pair of laser diode and photodiode was employed. The single wavelength at 808nm was selected to enhance the mean optical path length to avoid blood-specific changes during formalin fixation. Both fused deposition modeling and stereolithography were used to fabricate the optical station framework and other optical components were embedded. The testing and calibration were conducted, and the pilot experiments were performed with porcine breast tissue to verify the feasibility of the proposed approach.

The second project (Chapter 5) was to establish the product design framework for release of a novel photo-sensitive medical tape. Medical tape removal process is painful and causes medical adhesive-related skin injury (MARSI). We have introduced a photothermal sensitive medical tape by which an easy and painless tape removal is allowed while the initial strong adhesion provides a critical device securement. The prototype system consisting of off-the-shelf components was previously fabricated. This chapter focused on the analyses of preliminary testing and thermal performance data. The feasibility of the new medical tape system was evaluated with heat transfer simulation, and the design parameters for the future clinical system were proposed.

In summary, two different projects of opto-mechanical device design and development are presented. For formalin fixation monitoring for the novel millifluidic system, the preliminary feasibility studies lead to the robust design and development of the SW-LSI system (Project 1-Aim1) and optical transmittance monitoring system (Project 1-Aim 2) for CNB formalin fixation. The 3D printed optical station fabricated (Project 1-Aim 3) demonstrates the product-level practicability of the CNB quality monitoring feature, which can potentially reduce the turn-around time from taking a biopsy to making a diagnosis, and to standardize the fixation and tissue handling

processes in pathology workflow. The separate product design study (Project 2) of the photosensitive high adhesion medical tape suggests clinically practical design of the system, which considers potential users, use environments, and safety issues in addition to opto-mechanical operating parameters.

TABLE OF CONTENTS

LIST OF FIGURES

LIST OF TABLES

LIST OF ABBREVIATION

ARFI	acoustic radiation force impulse
ASCO	American Society of Clinical Oncology
ASME	American Society of Mechanical Engineers
CAP	College of American Pathologists
CNB	core needle biopsy
CNB	core needle biopsy
DC	decay constant
ER	estrogen receptor
ERG	ETS-related gene
FFPE	formalin fixation paraffin embedded
FISH	fluorescence *in situ* hybridization
FNA	Fine needle biopsy
GUI	graphical user interface
HER2	human epidermal growth factor receptor 2
IHC	immunohistochemistry
IR	infrared
ISH	*in situ* hybridization
IT	Intelimer® Tape
JTEHM	Journal of Translational Engineering in Health and Medicine
LD	laser diode
LED	light emitting diode
LSI	laser speckle imaging
MARSI	medical adhesive-related skin injury

MRI	Magnetic resonance imaging
NBF	neutral buffered formalin
NDF	neutral density filter
NIR	near infrared
OCE	optical coherence elastography
OCT	optical coherence tomography
PBS	phosphate-buffered saline
PgR	progesterone receptor
PID	proportional–integral–derivative
PoC	point of care
PT	prototype tape
PTEN	Phosphatase and tensin homolog
QD	quantum dot
RTemp	release temperature
STemp	switch temperature
SW	shear wave
SW-LSI	shear wave laser speckle imaging
SWV	shear wave velocity
TOF	time of flight
TTP	Time to peak

ACKNOWLEDGEMENTS

I would like to thank my advisor, Professor Eric J. Seibel, for giving me a great opportunity to begin my PhD research in your lab. Your inspiration, guidance, and encouragement through my doctoral years helped me to move forward with my research. And I appreciate your patience and dedication that finally make my degree possible. I would also like to thank my committee members, Professor Ashley F. Emery, Professor Matthew O'Donnell, and Professor Maria de Gador Canton for their supportive guidance. With those special committee members, I was able to make several milestones over the course of my graduate research.

To our big HPL community, being a part of the multidisciplinary team was certainly one of my best gifts for the graduate research. Not only can I receive knowledgeable and helpful feedback, but I also enjoy learning a lot of innovative things in different fields. On the top of that, I would like to acknowledge the supportive atmosphere among the past and present lab members, which is the most valuable of our lab.

I deeply thank all of those who have supported me throughout my long journey. Learning together, studying together, talking together, laughing together, drinking coffee and beer together, I have to say I am so lucky to have such amazing friends inside and outside of the campus.

Lastly, I would like to thank my family, who prayed for me and believed in me, who supported and encouraged me, and who is growing and crying for me. This journey would not have been possible without the love, support, and expectation of my family.

DEDICATION

To my parents for their unconditional love and unlimited support

Chapter 1. INTRODUCTION

1.1 CORE NEEDLE BIOPSY

Biopsies are routinely performed to investigate an abnormality in a body, e.g., cancer. Biopsies also provide important prognostic and therapeutic information. There are several million needle biopsies from various organs performed each year in the USA: 1.6 million breast biopsies [1], 1 million prostate biopsies (only in the Medicare population) [2], 0.6 million thyroid biopsies [3], plus lung biopsies, liver biopsies, pancreatic biopsies, etc. Different techniques can be used to obtain a biopsy: a fine needle, core needle, or surgical removal. Surgical biopsy is cutting of the entire lesion (excisional) or a part of a lesion (incisional) through skin. Highly invasive surgical biopsy leaves scars and often requires a few days of uncomfortable recovery time. There is a higher risk infection and bruising than other biopsies, but the diagnosis is accurate with fewer false negative results. Fine needle biopsy (FNA) became an alternative to surgical biopsy since the early 1990s because FNA is inexpensive and minimally invasive. However, FNA is subject to higher false negative results due to sampling errors, which delays diagnosis. FNA also requires cytopathologic evaluation, but it gives limited information due to a lack of histological architecture. Therefore, core needle biopsy (CNB) was introduced as an alternative to surgical biopsy and FNA. CNB offers less complications and a shorter recovery time than surgical biopsy. In addition, CNB obtains histologic samples that provides more specific diagnostic information than FNA. Although surgical biopsies and FNA are still performed for certain organs, such as breast and thyroid, CNB technique is increasingly replaced as the procedure of choice as it is simple, quick, safe, and relatively painless. In the future, there will be an increase in making a diagnosis *in vivo* and *in situ*. But as this trend develops, the need for tissue for “omics” analysis in

personalized medicine, such as genomic, proteomic, immunomics, metabolomics, etc [4] is expected to rise even faster. At this time minimally invasive CNB for breast tissue diagnosis is the "optimal initial tissue-acquisition method and the procedure of choice for image-detected breast abnormalities" and has been advocated to become the standard of care [5]. Most likely thin CNB will also become the gold standard for prostate, thyroid, liver, pancreatic, and other organ cancers.

1.2 FORMALIN FIXATION FOR BIOPSY

Fixation has been served as an essential step of tissue preparation in histology, pathology, and biology for over a century in order to preserve *ex vivo* cells and tissue from autolysis and putrefaction. 10% neutral buffered formalin, 4% of formaldehyde, is the widely used fixative. It is known to crosslink proteins with methylene bridges between adjacent amino acids in the proteins, preserving fine tissue structure and protein conformations and inactivating enzyme decay within the tissue [6]. Formalin fixative penetrates tissue relatively fast due to a small molecule of formaldehyde, however the binding (covalent cross-linking) process between proteins by formaldehyde is quite slow [7]. As a general guideline, formalin penetrates tissue at 0.5 – 1.0 mm/hour without clinical complexity. However, the fixation time is highly dependent on tissue size, type, and other environmental factors, such as temperature and pH, so that additional hours or overnight formalin fixation is typically recommended to avoid inadequate fixation. When fixation is not properly completed, mostly underfixed, the tissue cannot be restored and the results of histological and molecular pathological diagnosis can be erroneous, e.g., tissue distortion, poor quality of staining. Moreover, it is also known that the excessive formalin fixation results in loss of immunohistochemical antigenicity by irreversibly masking or destroying target epitopes. For those reasons, both under-fixation and over-fixation should be prevented [8]. Although

preanalytical variables of biopsy tissue have gained a great attention due to its importance for accurate and consistent diagnosis, the tissue preparation protocols established with a lack of standardization has not been changed over decades [9]. Each lab has established their own protocols and systems for daily pathology practice, the different protocols within loose guidelines are mostly accepted. Therefore, the importance to standardize the tissue formalin fixation protocol has been emphasized [10].

1.3 RESEARCH PATH

1.3.1 *Motivation and Objective*

In our lab, a CNB millifluidic system has been developing to promote the development of rapid point-of-care (PoC) pathology. In this millifluidic platform, the tissue preparation process will be automated such that the CNB is transported, preserved, stained, and imaged along the millifluidic channel. Therefore, a CNB transported from a biopsy needle is chemically fixed, stained, imaged, and further processed up to the point where it can be seamlessly accepted into traditional pathology workflows. The concept of the millifluidic device using a CNB was initiated and developed by Das and Seibel [11,12]. The novel purposes were to provide 3D microscopic visualization and hand-free tissue processing of a CNB for accurate and rapid PoC diagnosis. The CNB procurement and insertion, pressure-driven CNB transportation, tissue chemical and staining processes, and the fabrication of a monolithic silicon-based millifluidic channels were demonstrated at a proof-of-concept level [11–13]. However, this automated millifluidic system also needs to overcome the problem associated with non-standardized formalin fixation (described in Section 1.2) to offer rapid tissue-specific and biomarker-specific diagnostic evaluation. Therefore, **our specific research objective is to study chemical fixation monitoring for a CNB to provide non-contact**

real-time quality control and assurance features to the automated tissue processing in a fully enclosed millifluidic device.

1.3.2 *Preliminary research*

The preliminary feasibility studies for the automated millifluidic system, which led to the main research topics in this dissertation, are briefly introduced. 1) Millifluidic CNB transport based on the velocity and pressure of eccentric annular pipe flow, and 2) Shear wave (SW) elastography to measure the biopsy's mechanical property in a millifluidic tube. For millifluidic tissue transport, we performed the numerical simulation using COMSOL Multiphysics software and attempted to compare with the experimental data from a CNB surrogate. The eccentric annular flow patterns near a CNB surrogate was also demonstrated to understand the fluidic pressure buildup. Because the flow control to transport a soft and adherent biopsy is extremely complex, the new approach using pulsatile flow is under investigation by another group in our lab. For the formalin fixation, monitoring feature using SW elastography was inspired by the fact that the stiffness of tissue increases by formalin fixation, of which perceptual evaluation was reported by clinicians. Therefore, we have collaborated with the bioengineering department groups who are capable to provide the sub-micrometer resolution imaging of SW elastography using optical coherence elastography (OCE). This feasibility test showed the four-fold difference between fresh and fixed porcine pancreas tissues, indicating that the mechanical property change possibly evaluates the chemical fixation level of CNB [14]. The formalin fixation conditions of CNBs in a silicon-based millifluidic device were clearly identified in terms of the mechanical property change, i.e., Shear wave velocity (SWV).

1.3.3 *Potential impacts*

The accurate real-time formalin fixation monitoring system will not only eliminate redundant tissue preparation time and reduce the labor costs, it also has a potential to standardize fixation protocols to avoid weak immunoreactivity. Furthermore, time efficiency is especially needed for a slow cold-formalin fixation method which preserves DNA and RNA [15]. Most importantly, the optimization of the CNB processing can help guarantee that the highest quality and greatest amount of information can be generated from these small and very valuable tissue specimens. In addition, there is a great need for standardized tissue processing protocols in comparative cancer studies to determine optimal therapies based on pathology findings. For example, the emerging studies in immunohistochemistry biomarker discovery using the archived formalin fixed paraffin embedded (FFPE) tissue slides require the standardization for both therapeutic purpose [16] and proteomic analysis [17].

In this dissertation, two different approaches for formalin fixation monitoring are presented. The first approach (Chapter 2) [18] was to track the change of the mechanical property of biopsy in terms of SWV during formalin fixation. Using a sensitive real-time laser speckle imaging system, a SWV induced by a piezo actuator was monitored while the small biopsy was submerged in a millifluidic chamber. Although the robust fixation level measurement was demonstrated, the SW-LSI system still required a direct contact to the CNB in a millifluidic chamber. Acoustic radiation force impulse (ARFI) can replace the piezo-driven SW generation to avoid the direct contact to the CNB in the millifluidic chamber, but with additional cost and complexity. We proposed another new approach (Chapter 3) that evaluates the fixation level of a CNB in a completely non-contact way using optical transmittance change. The illumination light monitoring to account for inherent variations in a multi-hour process can successfully track the fixation level of a CNB

without vibration or temperature control. We also demonstrated the fabrication and testing of a low-cost manufacturing (3D printing) fixation monitoring system using low-cost components and simplistic data analysis. This 3D printed modular system can be integrated with any millifluidic chamber or channel in the middle of the automated millifluidic system. Our new low-cost real-time in-line monitoring for formalin fixation will assure the optimized turnaround time of tissue processing for the rapid and high-throughput PoC diagnosis delivered by the CoreView millifluidic system [19]. Our device can also serve as a novel supplementary tool for the standardization of CNB handling and fixation protocols in routine histopathological diagnosis. Future developments (Chapter 4) of a robust CNB shipment while processing and monitoring will allow a robust shipping strategy for a CNB in remote PoC testing including tough rural areas, where in-depth healthcare assessment is lacking.

Chapter 2. FORMALIN FIXATION MONITORING USING A SHEAR WAVE LASER SPECKLE IMAGING SYSTEM

2.1 ABSTRACT

Chemical fixation is the slowest and often the most uncontrolled step in the multi-step process of preparing tissue for histopathology. In order to reduce the time from taking a core needle biopsy to making a diagnosis, a new approach is proposed that optically monitors the common formalin fixation process. A low-cost and highly-sensitive laser speckle imaging technique is developed to measure shear wave velocity in a biospecimen as small as 0.5 mm in thickness submerged in millifluidic channels. Shear wave velocity, which is the indicator of tissue mechanical property and induced by piezoelectric-actuation, was monitored using gelatin phantom and chicken breast during fixation, as well as post-fixed liver and colon tissues from humans. Fixation levels in terms of shear wave velocity increased by approximately 271.0% and 130.8% in gelatin phantom and chicken breast, respectively, before reaching the plateaus at 10.91 m/s and 7.88 m/s. Within these small specimens, the plateau levels and times varied with location of measurement, and between gelatin and chicken breast. This optical-based approach demonstrates the feasibility of fine-tuning preanalytical variables, such as fixation time, for a rapid and accurate histopathological evaluation; provides a quality metric during the tissue preparation protocol performed in most pathology labs; and introduces the millifluidic chamber that can be engineered to be a future disposable device that automates biopsy processing and imaging.

2.2 INTRODUCTION

In medical practice, multiple trends are modernizing pathology, such as (1) increasing reliance on biopsy tissue processing for diagnostic and therapeutic, (2) obtaining biopsies from more minimally invasive procedures like needles, and (3) providing more rapid and less destructive tissue analysis of these smaller specimens from coring needles.

Histopathologic study of clinical tissue biopsies from suspicious lesions is considered the gold standard to identify and confirm disease diagnosis (e.g., cancer). Regardless of the size or type, currently all tissue biopsies are chemically-fixed to satisfy three primary criteria: specimen handling, absorptive/fluorescent staining, and antigen retrieval for immunohistochemical analyses. 10% neutral buffered formalin (NBF) has been most commonly used and best characterized in the pathology laboratories for more than 100 years [20,21]. Formalin fixation is the slowest step in biospecimen preparation process in which formalin fixative penetrates tissue relatively fast due to a small molecule of formaldehyde. However, the binding (covalent cross-linking) process between proteins by formaldehyde is quite slow [7]. Without clinical complexity, the speed of formalin fixation is generally recognized at 0.5 - 1.0 mm/hour, which is oversimplified. For example, there are recommended fixation times for human tissues, such as 6 to 72 hours of fixation for estrogen receptor (ER), progesterone receptor (PgR), and human epidermal growth factor receptor 2 (HER2) testing for breast cancer [22], and more than 8 hours for quantum dot (QD) *in situ* hybridization (ISH) in prostate needle biopsy [23]. However, in most cases, pathology laboratories develop the effective preanalytical factors in tissue handling, such as fixation time, through empirical approach based on their infrastructure, tissue geometry, and target biomarkers, presumably because of a lack of standardized fixation parameters. Some experts present conflicting results to the consensus recommendations [24–26] and even claim that those consensus

recommendations describe largely “faith-based” exercises, and are not based on the scientific evidence [27]. When fixation is not properly completed, mostly underfixed, the tissue cannot be restored, and the results of histological and molecular pathological diagnosis can be erroneous, e.g., tissue distortion, poor quality of staining, while over-fixation can be partially reversed by antigen retrieval [23,28–30]. In addition, more efforts to understand the preanalytical variables, especially fixation approach, in conventional biospecimen process are being made as cancer immunotherapy techniques are being translated into the clinic, which requires the high-quality nucleic acids for molecular diagnosis [31–33].

Minimally-invasive biopsy, such as core needle biopsy (CNB), is becoming more common as a tissue sampling method in cancer management because of the great benefits of being cost-effective, less painful, easier sampling, and lower postoperative morbidity compared to a surgical biopsy [1,34,35]. Each year in the United States, several million needle biopsies from various organs are procured: 1.6 million breast biopsies [1], 1 million prostate biopsies (only in the Medicare population) [2], plus lung biopsies, liver biopsies, pancreatic biopsies, etc. Now, minimally invasive CNB for breast tissue diagnosis is the “optimal initial tissue-acquisition method and the procedure of choice for image-detected breast abnormalities” and has been advocated to become the standard of care [5].

The small size of CNB makes the tissue specimen valuable because of tissue scarcity for diagnostics, and also chemical processing times are reduced with such small volumes (typically 10 - 40 mm^3). Since chemical fixation is the slowest step in the established process of histopathology, speeding up this process has been the focus of numerous studies. One approach is enhancing the fixation process with or without NBF, such as rapid two-temperature fixation [36], elevated pressure fixation [37], ultrasound-facilitated fixation [38], microwave fixation [39].

Alternatively, there have been persistent studies on alcohol-based fixatives, which offers faster fixation and longer preservation of protein, DNA, and RNA while having a similar histomorphology by NBF [40–43]. Implementation of all these different techniques requires a highly flexible laboratory environment, while manually handling CNBs is tedious and overnight tissue batch preparation with a tissue processor is needlessly slow. Instead, the small specimen size lends itself well to an enlarged version of microfluidics or millifluidics where Lab-on-a-Chip technologies can process small biospecimens. This novel millifluidic device, which is under development in our lab [11,12,44], may aid clinicians in the rapid assessment of CNBs. Once imaged within the device, the specimen may be seamlessly passed into the standard pathology workflow and conventional histopathological evaluation.

Thus, the previous listed three multiple trends modernizing pathology may soon require the development of process control of the CNB sample preparation, which would include real-time monitoring of chemical fixation. There has been a study to quantitatively monitor the fixative diffusion using an ultrasonic time-of-flight technique [45]. However, the fixative diffusion is not correlated to the structural modification by fixation, which cannot be solely evaluated by compressional wave transport, especially in two-phase (liquid-solid) interfaces. In contrast, a shear wave, which can only propagate in solids, is feasible to detect the real-time structural changes of the biospecimen while submerged in fixative. For the shear wave propagation, laser speckle imaging (LSI) is a highly sensitive and relatively low-cost configuration without experimental complexity compared to other imaging modalities (e.g., ultrasound, OCT and MRI). Furthermore, LSI can be used on a small CNB sample in a millifluidic chamber.

In this paper, we propose the shear wave laser speckle imaging (SW-LSI) configuration to measure the SW velocity (SWV) of a CNB-sized specimen in NBF-filled millifluidic channels, by

which the dimensional and temporal changes of the fixation level were evaluated in terms of the stiffness indicator, the shear wave. The approach uses non-destructive optical light scattering which can be conducted on these small specimens within a small millifluidic chamber or channel. Low cost and portability are also requirements since these fixation monitors are designed to be ultimately used at the point-of-care. In this preliminary study, the SWV at different depths of a sub-centimeter-scale submerged gelatin phantom and chicken breast sample are measured to quantitatively track the biopsy-sized specimen's fixation level during formalin-fixation in millifluidic channels. The results of SW-LSI measurement in biological tissue, including any animal tissue, is presented for the first time. In addition, monitoring the formalin fixation using SW-LSI, to the best of our knowledge, has not been reported previously. The ancillary measurements of fully fixed human liver and colon biopsy are also added to the comprehensive results from 6% gelatin phantom and chicken breast. In conclusion, we propose that this noninvasive fixation monitoring system helps to eliminate redundant tissue preparation time in avoiding underfixation, eventually reduce the labor costs of manual processing, and have the potential to finely engineer fixation protocols for tissue size, type, and specific molecular biomarkers as well as other fixatives.

2.3 Materials and Methods

2.3.1 Optical-Based Apparatus for Shear Wave Velocity Measurement

Elasticity measurement can be achieved through two methods: strain ratio and acoustic wave velocity measurement. The strain ratio measurement under static or dynamic compression is a simple and straightforward method. However, this technique is not able to measure Young's modulus quantitatively because the applied local stress is difficult to measure. The properties of

acoustic waves can also be used for elasticity. Wave propagation speed is characterized by the acoustic impedance which depends on the mass and elasticity of tissue. The speed of compression wave is determined by the bulk modulus (the inverse of the compressibility) and density of both solid and fluid media. In contrast, the speed of shear wave is dependent on the shear modulus and density of a solid. Therefore, the measurement of shear wave is more suitable to determine the mechanical property change of tissue, ignoring the effect of the proportions of interstitial fluid and other solutions, i.e., fixative. Another advantage of shear wave is that the broad range of its velocity compared to that of compressional wave which differs less than one-thousandth of the velocity in different tissue types [46]. The shear wave is expressed by Newton-Laplace equation in terms of the shear modulus and density of a medium; $v_s=\sqrt{(G/\rho)}$, where G is shear modulus, v_s is shear wave speed, and ρ is solid's density.

LSI detects and evaluates dynamic motions in a scattering medium using the spatiotemporal change of local 2D speckle patterns [47–49]. Speckle pattern is the interference pattern formed by the illumination of scattering particles, and the series of the temporal speckle patterns are similar in appearance to the video of fast-moving objects captured by a camera. And those movements (i.e., the shear wave) are shown as the temporal change of local speckle patterns with a short camera exposure time or the local blurring with long exposure time. The speckle pattern series,

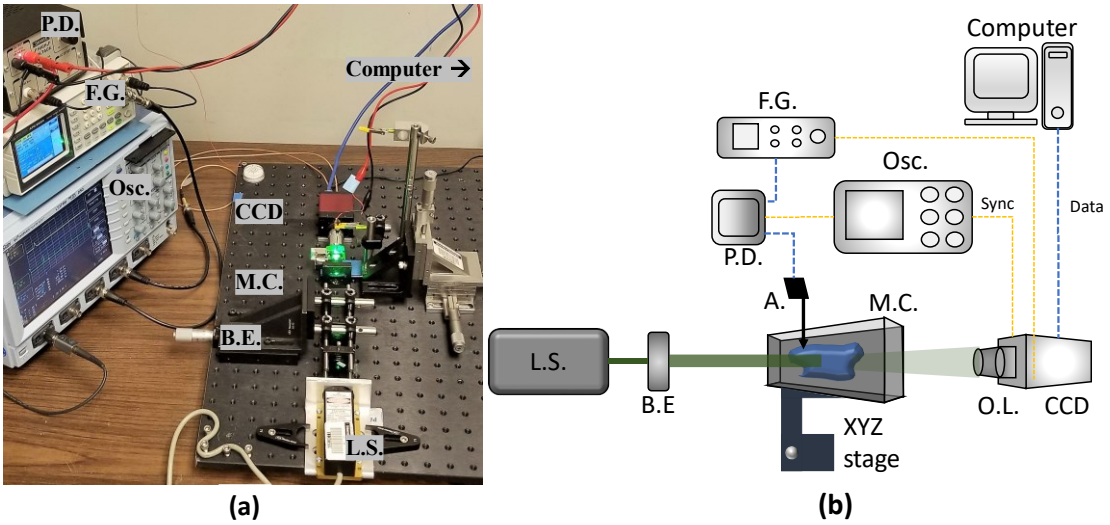

Fig. 2.1 (a) An experimental apparatus (b) A schematic of experimental setup on left. L.S.: laser source, B.E.: beam expander, M.C.:milifludic chamber, O.L.:objective lens, A.:actuator, P.D.:piezo driver, F.G.: function generator, Osc.:oscilloscope

therefore, reveal the spatiotemporal distribution of shear wave. High-resolution speckle patterns can be monitored through magnification (i.e., a 5X objective) and at substantially higher SNRs as pixel (px) sizes for machine vision cameras are continuously trending to smaller sizes (7.4 µm). LSI systems are additionally simple to set up as a benchtop apparatus (Fig. 2.1)

2.3.2 Sample Preparation

This formalin fixation study was divided into two parts: a dimensional study and a temporal study. The dimensional study aimed to evaluate the fixation level change at different depths in a thick specimen (width = 15 mm). In the temporal study, the average fixation level change in a thin specimen (width = 1.5 mm) was investigated over time. Gelatin phantom used in both studies was not only chosen for a rapid and easy way to control the phantom characteristics, but also to mimic the chemical fixation process in soft tissue by formalin [50]. The gelatin phantoms were fabricated

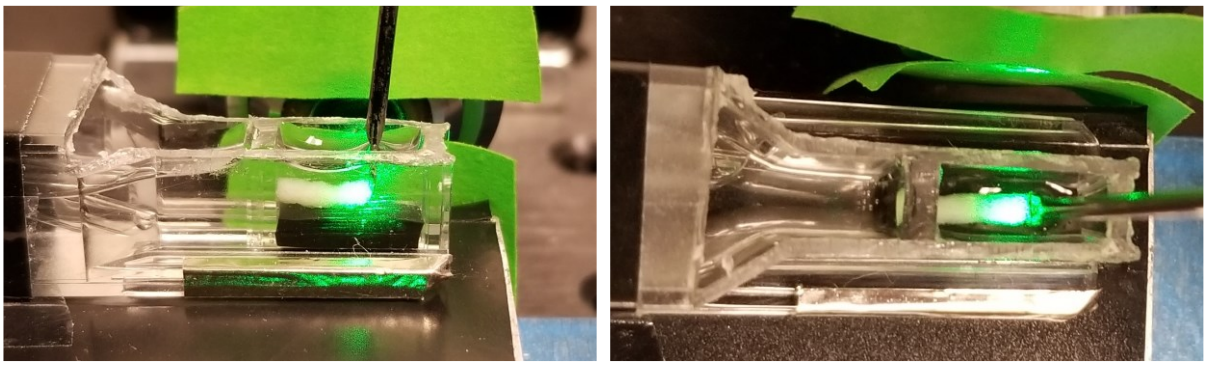

(a) (b)

Fig. 2.2 Chicken breast tissue located in a cuvette channel filled with formalin. (a) Side view and (b) Top view

with the gelatin powder (Sigma-Aldrich, 300 Bloom) at the mass concentration of 6% and Titanium Oxide (US Research Nanomaterials, Inc., TiO2 18nm) at the mass concentration of 0.3% to enhance optical scattering. In addition, fresh chicken breast was prepared to compare the fixation behavior with gelatin phantom. The human liver and colon tissue after prolonged formalin fixation were also prepared to be benchmarks for clinical translation.

Dimensional Study

Gelatin phantom and chicken breast cut in a cube shape, at 15mm×15mm×15mm, were used during formalin fixation and later sliced into a biopsy sample for imaging. A single specimen cube was required for every hour of image acquisition, e.g., fresh, 1 hour, 2 hours, and so on. The prepared cubic samples were immersed within a 15 times greater volume of NBF. Each hour during fixation, one cube was sectioned into CNB cross-sectional size, approximately 1.5mm×2mm×2mm, for three different depth points of interest (i.e., 1.5mm, 4.5mm, and 7.5mm in depth from surface) and placed in a custom-designed water-filled open-top cuvette (Fig. 2.2). The sliced specimen was completely submerged, and the focal plane of the sensor was placed at the middle of the slice, which was the specified depth from the surface of the block. In order to

have consistent sample specimens at the initial condition, the gelatin phantom cubes were made from a single mold of a gelatin mixture batch. The chicken breast cubes were obtained from the single piece of a large chicken breast after removing fat and connective tissues.

Temporal Study

To evaluate the mechanical property change of a 2mm biopsy-sized specimen by NBF, SWV measurement was conducted within short time intervals (10-15 minutes) over 3 hours (up to 5 hours with a longer time interval, around 30 minutes) for gelatin and 4 hours for chicken breast. The specimen was not moved during the entire experiment after it was positioned in the millifluidic channel. The channel holds 20 times more volume of NBF than the specimen.

Human Tissue Measurement

Human liver and colon extra tissue samples were also acquired from University of Washington Northwest Biotrust. IRB approval was already obtained by the principal investigators (Eric Seibel and Rodney Schmidt, retired Pathologist). The tissues, in about 10 mm^3 block size, were kept in NBF more than three months, which were considered as prolonged fixation. Both tissue types were cut down to 0.5mm and 1mm in thickness for liver and colon tissues to allow for strong optical scattering. Positioning and measuring protocols were the same as above.

2.3.3 System Operation

A 532nm 10mW laser (B&W Tek, BWN-532-10E) was expanded to a 3mm-diameter collimated beam and transmitted through a tissue biopsy sample orthogonal to the propagation direction of the shear wave, thus producing a speckle pattern image. Polarizing and neutral density filters were introduced after the beam expander to adjust speckle pattern intensity variation based on specimen thickness and camera exposure time (Fig. 2.1). A machine vision camera (Allied Vision, Prosilica

GE1650, 1.9MP CCD) was precisely positioned opposite the laser beam to capture the speckle pattern over time. Phantom or tissue in a millifluidic channel attached to an XYZ-translation stage was located between the laser and camera. The dimension of the open-top millifluidic channel is 4mm × 5mm × 15mm (width × height × length), allowing placement of thick CNBs up to 9-gauge needle size. A disposable cuvette is customized for millifluidic channels because of low cost and easy reproduction, however, glass-based channels can also be used. A flat-headed needle tip of a stack piezoelectric actuator (STEMiNC, SMPAK15553D4, 3 × 3 × 5mm, 0.15uF) provided vertical force to the sample in the millifluidic channels. The displacement of the force was set to 0.5 μm, and a single cycle of 1 kHz sinusoidal signal was applied. The laser speckle pattern was recorded by the camera with a magnification of 5 power (5×) through an objective lens. The minimum speckle size (S) is estimated by the relationship, $S = 2.44\frac{(1+M)\times\frac{f}{\#}}{\lambda}$, where λ is a laser wavelength, M is the imaging magnification, f/# is the f-number of the imaging system. And, our system has a minimum speckle size of 38.5 μm and equivalent to 5.2 pixels (N = 5.2). The spatially oversampled speckle patterns have slightly better resolution than the Nyquist sampling criteria, N = 2 [51].

Once the specimen was inserted in the millifluidic channel, the field of view (FOV) of the camera and the contact position of the piezoelectric actuator (piezo) tip on the specimen contact were adjusted to locate the point of piezo force on the top side edge of the FOV to maximize the distance of shear wave propagation within FOV (d = 1.8 mm). The midplane of the specimen, the identical plane of the piezo tip, was then focused by the objective lens and sensor. MATLAB image acquisition toolbox was used to acquire image data and operate the camera, which was synchronized with a piezo amplifier (A.A. Lab Systems, A-301HS), a function generator (GW Instek, AFG-2225), and an oscilloscope (LeCroy, LT374M).

2.3.4 Data Acquisition

The region of interest for the CCD sensor was cropped to 400 px × 1200 px for fast data acquisition which increased the frame rate from 30 to 50 frames/second. The 12-bit sampling depth of an analog to digital converter was selected to record over 8-bit to increase the sensitivity of speckle pattern imaging as the speckle images suffer from significant noise. Due to the restriction of the frame rate, sequential equivalent-time sampling was employed to increase the effective camera frame rate [52]. For example, when the camera frame rate was set to 50.00 Hz the excitation pulse

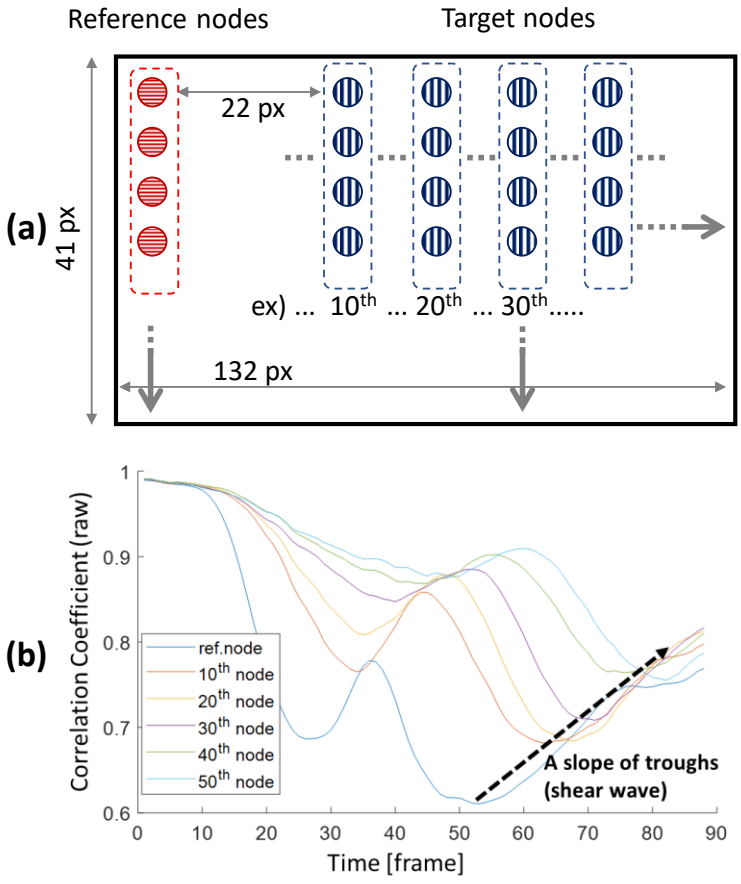

Fig. 2.3 (a) A grid of reference and target nodes. (b) Example correlation coefficient signals of fresh 6% gelatin over time at the reference and target (every 10th) nodes averaged along the vertical dotted box shown in (a).

was repeated at the slightly faster frequency, 50.05005 Hz (period = 19.98 ms). The incremental time delay between camera frame rate and mechanical excitation frequency was registered in every camera frame such that the effective frame rate of the system corresponded to 50.00×10^3 frames/second.

2.3.5 Image and Signal Processing

Image Processing

The local speckle change, or disturbance, due to shear wave propagation was visualized after computing speckle correlation. A unique speckle pattern in a 2D kernel was compared to the one at the same location in a later frame interval, returning correlation values. 2D kernel size was 22 px ×11 px of which twice larger size in the vertical direction parallel to the piezo tip alignment was specified to better detect the up and down movement of shear wave. The correlation computation for 2D kernel was conducted on a uniformly spaced grid over an image, a node per 9 pixels, to decrease the computation time down to 45 seconds per a single set of 600 speckle images (Intel i7-4820K, parallel computing), hence, the pixel dimension of the correlation coefficient images was decreased to 41 px ×132 px (Fig. 2.3 (a)). To increase signal-to-noise ratio by rejecting background low-frequency noise, the reference image of the speckle kernels kept a constant time interval (i.e., 100 frames) from the processing image frame. The set of correlation coefficient images then visualized shear wave propagation as shown in Fig. 2.4 (a). In Fig. 2.4 (c), a spatiotemporal plot from the correlation images by averaging in the vertical direction and the actual

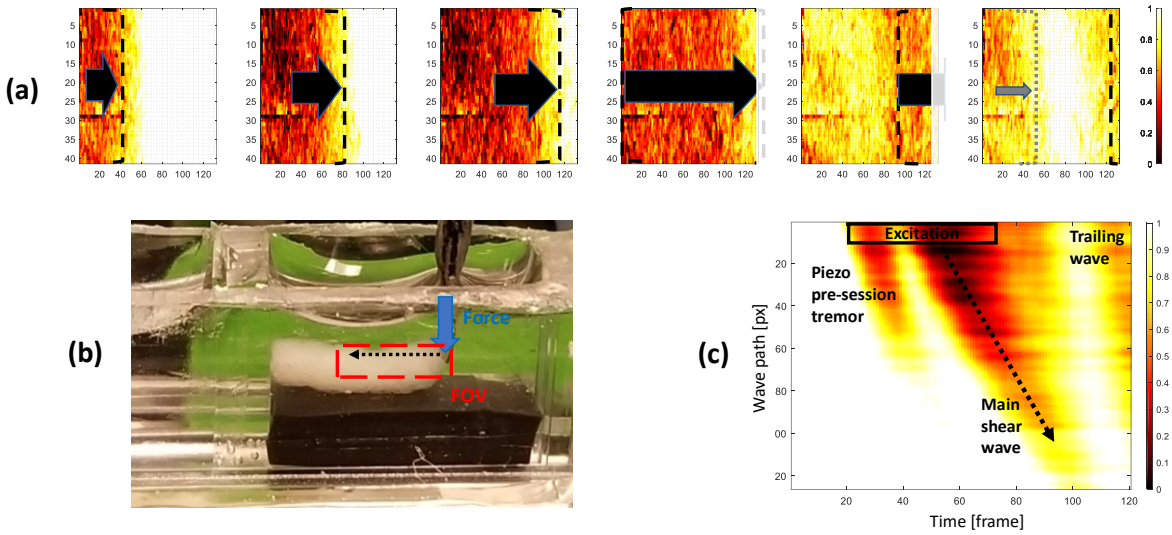

Fig. 2.4 (a) Example shear wave propagation in speckle correlation maps (41px × 132px) at 0μs, 172.6μs, 345.3μs, 517.9μs, 690.9μs, 863.2μs, respectively. Low values of correlation coefficient indicate the shear wave (black arrow) and the last screen shows the following wave (small gray arrow). (b) Field of view (red box) in a chicken breast specimen. Shear wave propagation direction (black arrow) from the piezo excitation (blue arrow). (c) Spatiotemporal map of the specimen same location of FOV in (b). The excitation duration was 1ms (single pulse at 1kHz) as shown with the black box (1ms is equivalent to 50 frames at the sampling frequency of 50kHz). The weak waves before and after the shear wave are presumably due to the inertial mass of the piezo actuator and tip.

location and the direction of the shear wave were shown in Fig. 2.4 (b). The slope of the shear wave, the dotted arrow in Fig. 2.4 (c), represents the SWV (SWV $= \frac{dx}{dt}$).

Signal Processing

Time to peak (TTP) cross-correlation method is the most common approach with shear wave elasticity imaging [53]. We implemented the TTP method with multiple improvements to suppress

very strong noise in laser speckle images from unevenly-accumulated laser scattering, sample inhomogeneity, viscoelasticity, and external vibrations. Shear wave estimation was calculated between the excitation region and detection region. The minimum distance between regions was set to 22 px in the correlation map (equivalent to 200 px in a raw speckle image) to avoid significant error resulting from cross-correlation within a very short interval of time and distance. The detection region was not selected within a specific distance from the excitation area but chosen in multiple locations with gradual distances from the excitation to apply a linear fitting over the image. Fig. 2.3 (a) shows the diagram of the node grid. The main shear wave area, the most decorrelated area, was zoomed in for further signal processing. In Fig. 2.3 (b), the signals along the wave propagating direction were plotted; the deep troughs represented the main shear wave and the time delays were shown at every 10^{th} node from the reference location. Instead of simply estimating TOF of wavefront of the peak, we used the cross-correlation between reference and target signals so that the signal distortion due to wave attenuation and dispersion effects was partially compensated. The signals at nodes were normalized and processed with a low-pass (<20kHz) and high-pass (>100Hz) filters to reject other vibrations except for excitation wave. The correlation process also made use of a zero-phase crossing technique which overcomes the limit of the discrete temporal resolution, which was a frame. From the result of time delay and distance with the node grid, a straight-line robust regression with the bisquare weighting function determines the shear wave group velocity excluding measurement errors or significant outliers.

2.4 RESULTS

2.4.1 Dimensional Study

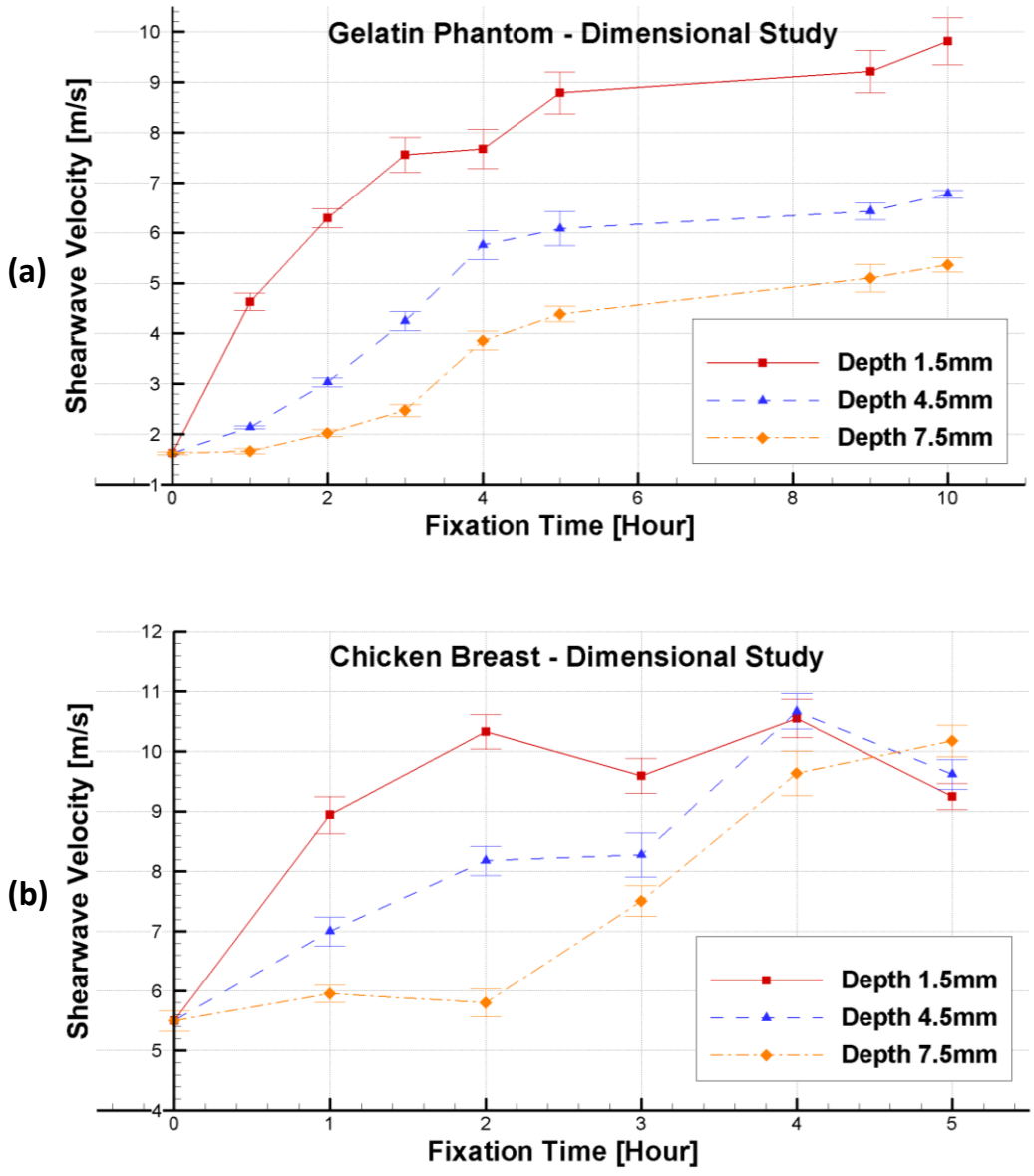

Fig. 2.5 Change of shear wave in the dimensional study. The error bars represent the plus and minus of the standard deviation from the mean SWV. (a) 6% gelatin phantom (b) Chicken breast

Table 2.1 Summary of SWV in the dimensional study: 6%(w/w) Gelatin and Chicken breast

SWV ± SD [m/s]									
		Fixation hours							
Specimen	Depth	0	1	2	3	4	5	9	10
6% Gelatin	1.5mm	1.62±0.04	4.63±0.18	6.29±0.19	7.55±0.35	7.67±0.39	8.78±0.42	9.21±0.42	9.81±0.46
	4.5mm	1.62±0.04	2.14±0.03	3.03±0.09	4.25±0.19	5.75±0.28	6.09±0.34	6.43±0.17	6.77±0.08
	7.5mm	1.62±0.04	1.67±0.06	2.03±0.07	2.47±0.12	4.36±0.19	4.39±0.15	5.10±0.27	5.36±0.15
Chicken Breast	1.5mm	5.50±0.17	8.94±0.31	10.32±0.28	9.59±0.29	10.55±0.32	9.25±0.22	-	-
	4.5mm	5.50±0.17	7.00±0.25	8.18±0.25	8.27±0.37	10.67±0.30	9.62±0.25	-	-
	7.5mm	5.50±0.17	5.96±0.14	5.80±0.23	7.51±0.26	9.64±0.37	10.17±0.26	-	-

The spatiotemporal change of SWV in 6% gelatin phantom and chicken breast under formalin fixation are presented in Table 2.1 and Fig. 2.5. The SWV prior to fixation was measured once for all depths. During formalin fixation of gelatin phantom, the SWV increases rapidly during the first 3 hours at 1.5mm depth before the stiffening rate slows down. The stiffening at 4.5mm and 7.5mm depths are slower than the outer area, but they also become sluggish after 4 hours of fixation. The SWV of chicken breast shows similar stiffening behavior up to 3 hours fixation, however the SWVs at all depths reach the equivalent level of the plateau.

2.4.2 2mm Biopsy Temporal Study

Fig. 2.6 shows the change of the SWV over time in 2mm size of 6% gelatin and chicken breast. The changes in SWV with gelatin phantom shows the gradual increase up to 3 hours of fixation, while the chicken breast specimen rapidly stiffens within an hour and becomes stationary. A small drop, about 10%, is observed in the chicken breast case as it is also shown in the dimensional study.

2.4.3 Fixed Human Tissue Measurements

Prolonged-fixed (more than 3 months) human normal liver and colon tissue were also observed in our setup. Fig. 2.7 displays the SWVs of 3-hour fixed 2mm gelatin and chicken breast in addition

to fixed human liver and colon. Human liver and colon tissue yield 12.5 ± 0.27 m/s and 9.6 ± 0.53 m/s of SWV, respectively.

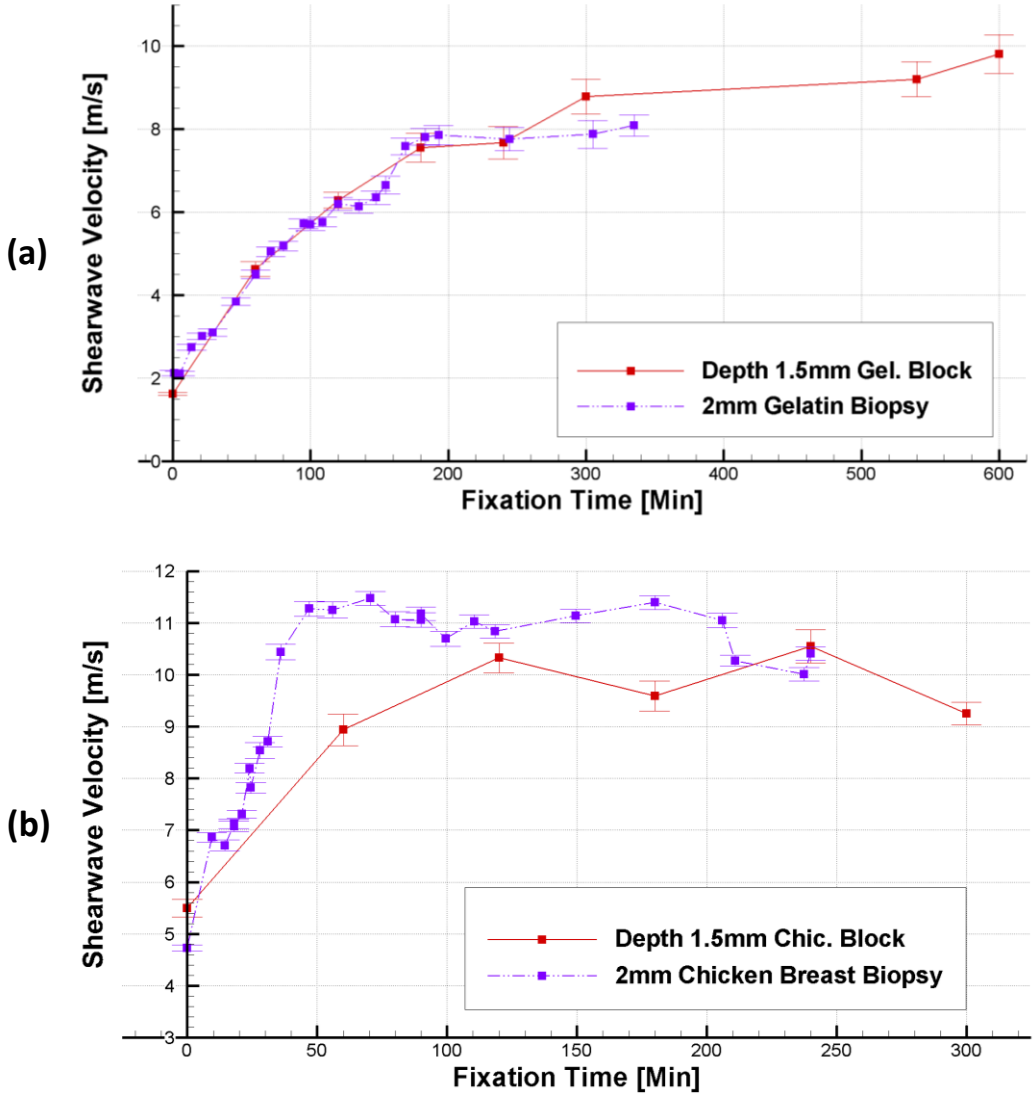

Fig. 2.6 Change of shear wave in the 2mm biopsy study (Purple point and line). The error bars represent the plus and minus of the standard deviation from the mean SWV. (a) 6% gelatin phantom (b) Chicken breast. The SWVs of the outer area (1.5mm depth from the sample block surface) in dimensional study are overlaid (Red point and line).

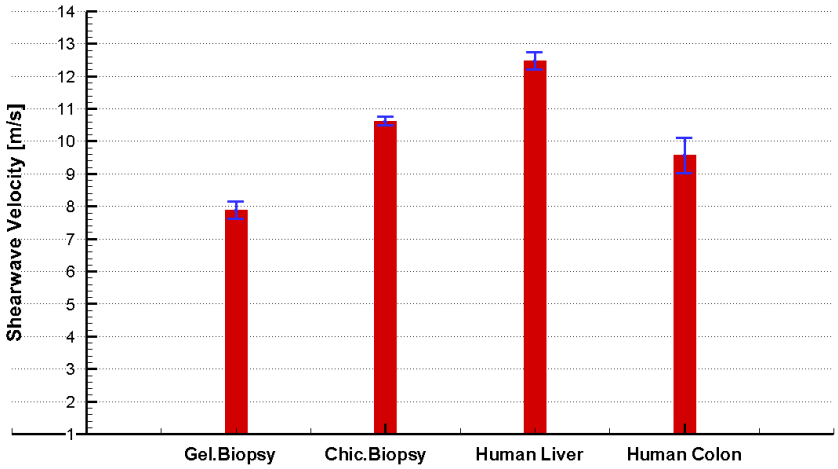

Fig. 2.7 Prolonged-fixed human tissue measurements compared to fixed 6% gelatin and chicken breast biopsies

2.5 DISCUSSION

The SWV changes of gelatin phantom and chicken breast during formalin fixation were investigated using the LSI system in this study. The specimen's thicknesses ranged from sub-millimeter using human tissue to two millimeters using chicken breast and 1 to 4 mm using tissue-mimicking phantoms. The use of small specimen size is unlike other LSI studies [47,54,55], where the size of the tissue-mimicking phantom ranged from 12 mm to 40 mm. In our LSI visible light system, the image processing for SWV measurement requires a minimum FOV of 150 µm × 450 µm (height × length), which sets the minimal specimen thickness. Thus, all CNBs and possibly even fragmented CNBs can be monitored for fixation within a millifluidic channel of diameter 1-5 mm.

The SWV of 6% gelatin phantom is in good agreement other gelatin studies; SWV at 2 ± 0.5 m/s estimated by Orescanin and Insana in 2010 [56] is within 22% error of our results (averaged SWV

of fresh gelatin), and the SWV at 1.63 m/s reported by Manapuram et al., in 2012 [57] is within 0.6% of our results. In addition, according to the extensive literature review by Sarvazyan et al. in 2013 [46], various shear wave velocities in human breast, liver, kidney, lung, and spleen are within a range of 0.85 m/s and 3.54 m/s, which fall into the SWV range of fresh or fixed 6% gelatin. There is little stiffness information for fixed human tissues, however, animal tissues (chicken breast, cartilage, and tendon, and porcine fat and liver) are known to be stiffened approximately by 50-170 % [58], which are also within our SWV measurement range, 2-13 m/s.

Chemical fixation (covalent crosslinking) begins at the exposed surfaces where the formalin is diffusing through. However, the fixation levels inside the specimen were varied by the different specimen structure; homogeneous (6% gelatin) and heterogeneous (chicken breast). Fig. 2.8 shows the graphical illustration of the fixation level comparison between isotropic and anisotropic specimens, which is discussed in the following section.

In the dimensional study of the gelatin phantom (Fig. 2.5 (a) and Fig. 2.8 (a)), the fixation rates which is the slopes of SWV increases were differentiated at each depth as the supply of formalin was controlled by the fixation process. As the outer area contacted with sufficient formalin is stiffened rapidly and acts as a barrier to subsequent inward formalin diffusion [59]. The fixation process in the inner core of the sample is then gradually restricted by the formaldehyde supply. Therefore, the SWV plateau of inner sides was reached at different values from the outside. Because the long-term fixation of gelatin phantom with a small portion (about 0.4% of formalin mass fraction) showed that the stiffness of the gelatin took about 100 days to reach its equilibrium [50], it is not yet clear whether the 6% gelatin block becomes more stiffened after this sufficient exposure to formalin. However, the smooth slope change of SWV up to its plateau was demonstrated and any significant hardening was not shown after 10 hours. It should be also noted

that the similar trend, being plateaued after constant increments, of clinical Q score of estrogen receptor over the mean fixation times for human breast CNB was presented in Goldstein et al. study [28]. Chicken breast in Fig. 2.5 (b), however, exhibited the dissimilar behavior that SWVs at three different depths reached the similar value (9.47 ± 0.97 m/s) after 4 hours formalin fixation. Although it is difficult to interpret too much from these preliminary results, the structural anisotropy in chicken breast muscle tissue likely facilitates the inward formalin diffusion, resulting in more rapid and spatially uniform SWV, see Fig. 2.8 (b). The structure of fresh chicken breast looked heterogeneously stratified but dense and well-bonded, however, those layers become loosened as formalin is introduced after about an hour. For that reason, the delaminated chicken breast layers appear to allow formalin to flow inside the tissue resulting in the uniformly fixed condition at t4 (Fig. 2.8 (b)). These observations may also explain the small (< 10%) SWV fluctuation once the SWV was plateaued, which was not shown in the gelatin measurements.

The results from the temporal study with 2mm-biopsy sized specimens in Fig. 2.6 (purple lines) also showed graphical correspondence to the results of the outer surface of the large block in Fig. 2.5, which is overlaid in Fig. 2.6 (red lines). Although the gelatin phantoms correspond very well between two measurements, the chicken breast shows a large discrepancy (2.2 times faster rate increase of SWV in 2mm biopsy) during the first hour of fixation. However, this could be explained by the structure of chicken breast as explained above. In addition, although the cautious handling with a fresh razor blade or sharp scalpel was necessary to avoid the coarse roughness or torn-like surfaces of raw tissue specimens, the preparation of the 2mm-sized raw chicken breast specimen was challenging which causes damage on the small sample, while preparing the larger fresh tissue block required much less effort, causing less damage.

In the human fixed tissue measurement (Fig. 2.7), fully-fixed human liver and colon samples were measured with our apparatus. The fixed liver specimen showed the strong scattering at 532nm laser wavelength. So, the thickness for measurements was adjusted down to 0.5 mm until the current apparatus was able to acquire useful speckle pattern images (SNR > 2.6, in speckle correlation images). In contrast, the colon specimen in 2mm thickness was measured at the similar scattering of our 6% gelatin with TiO^2. Although relative fixation level was not measured, these pilot data suggest the feasibility of our shear wave LSI setup for human organ tissues.

It should be noted that the SWV measurement offers a quantitative evaluation of specimen's mechanical property, in which SWV is proportional to the square root of shear modulus (or elastic modulus) assuming a linear elastic behavior and small deformations. Although soft tissue is generally viscoelastic, this assumption is broadly accepted in the elastography fields [60] for short response time at small displacements. Because of its simple and straightforward unit conversion, our results are presented with SWV in [m/s] instead of shear or elastic modulus in [kPa].

Throughout this report, we simply employ the group velocity of shear wave propagation, while the actual mechanical wave in a thin specimen undergoes multiple wave modes (Lamb or Rayleigh waves) based on the boundary conditions and the geometry of the medium. In the recent study using OCT with an acoustic tapping technique [61], the shear wave generated in thin tissue such as cornea showed multiple Lamb modes and was significantly influenced by various factors such as the frequency range, excitation conditions, and the ratio of the layer thickness to wavelength of the propagating wave. However, the evaluation of fixation using SWV changes does not focus on the comparison between other tissue types or processing conditions, hence, we only consider the change of group velocity of shear wave, which provides enough information of the temporal and relative change of fixation level on each specimen. For the same reason, other parallel studies

using the standard measurements for hardness such as durometer, or Young's modulus from uniaxial tensile testing are not necessary for the goals of this study.

The SW-LSI measurement is vulnerable to noise from environmental factors such as room temperature and light as well as external vibrations. The room temperature was kept at 22˚C and checked in advance of the experiments. The electronic equipment and optical breadboard were

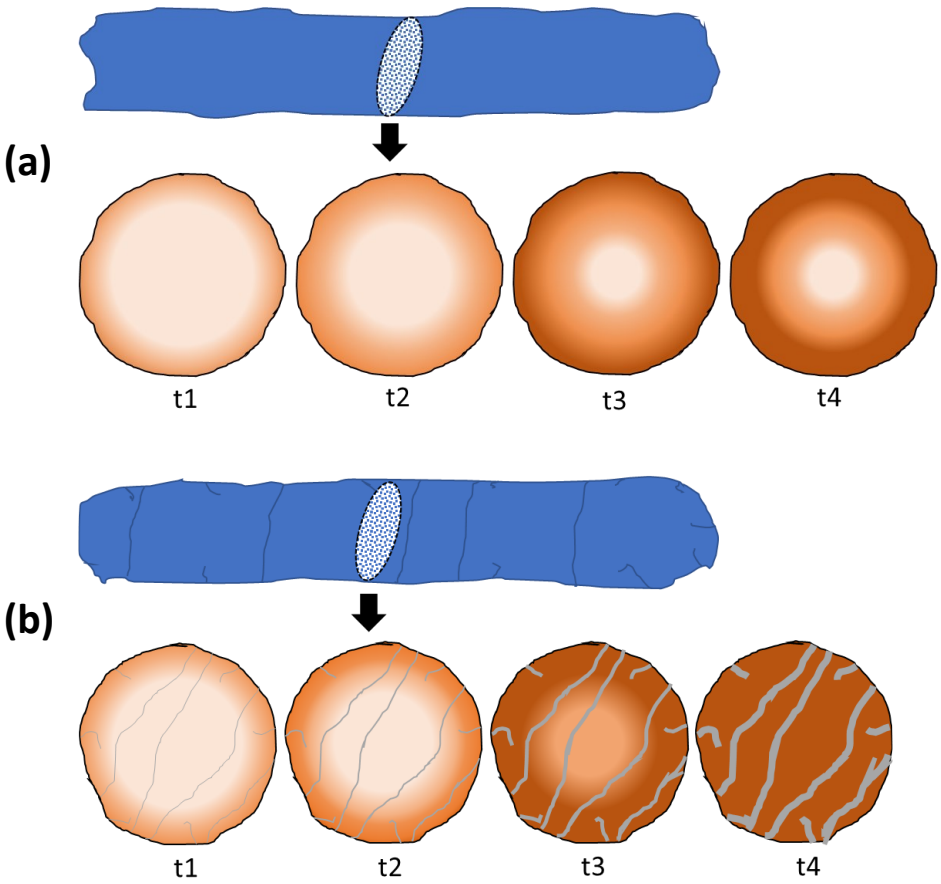

Fig. 2.8 Illustration of fixation progress in (a) An isotropic model for 6% gelatin and (b) An anisotropic model for chicken breast. Gradient color represents the level of fixation and fixation time elapses from t1 to t4. The heterogeneous divisions, such as delamination and cracks, are displayed in (b), widening over time. For visual purpose, three discrete annular regions for fixation level are depicted in the cross-sectional area of CNBs

mechanically isolated independently with Sorbothane (Sorbothane, Inc., Kent, OH), and the piezoelectric actuator and millifluidic chamber were also padded with Sorbothane. Thus, the noise level in the correlation images was suppressed to less than 5% regardless of shear wave excitation. In addition, the camera exposure time (50μs) was short enough to not be sensitive to changes in ambient lighting.

Our measurements with gelatin phantom and chicken breast showed good repeatability that all standard deviations were less than 10% of the measured SWV. That error variance in mechanical property among the fresh gelatin phantoms was presumably attributed to the phantom fabrication in each individual experiment, while the heterogeneous structures (such as fat, connective tissue, and stratified layers) of the fresh chicken breast was believed to contribute to the measurement variability.

The systemic restriction of this study is the limited performance level of the experimental equipment that was borrowed from previous studies. A camera sensor with a faster frame rate and shorter exposure time than the current setting (50Hz and 50μs, respectively) may improve the sensitivity on laser speckle pattern changes. A stabilized laser source at near-infrared wavelength was unavailable, but, would be expected to avoid larger optical absorption of hemoglobin [62] and demonstrate significantly better penetration in tissues [63,64].

Another limitation of our systems is that the shear wave was induced by physical contact with a piezo actuator. This simple system was chosen because the local shear wave could be efficiently generated, and the SWV measurement could be achieved while the biospecimen was submerged in formalin. In the future, a remotely induced shear wave by an ultrasonic transducer [48] can be applied to develop a closed channel monitoring system which is superior in reducing manual handling requirements and allows full automation with lower risk of contamination.

Clinical impact

Rapid and optimal tissue fixation has been of great interest in pathology and there have been numerous attempts in clinical studies as described in the introduction. Unfortunately, formalin fixation is still not well understood or controlled to the optimal fixation level in terms of results from further tissue processing protocols; staining, sectioning, and diagnosis [42,65,66]. For example, in breast cancer, the ASCO/CAP Task Force recommends more than 6 hours fixation for breast cancer biomarkers, ER, PgR, and HER2 [22]. On the other hand, the recent clinical studies, with the goal of speeding up the pathology and hence breast cancer diagnosis, investigated the potential of rapid CNB fixation regarding the sensitivity of essential biomarkers. Sujoy et al. in 2014 [25] reported that no negative effect on ER-IHC with only 30 minutes fixation. And in 2017, Halilovic et al. [26] presented good agreement of ER, E-cadherin IHC, and HER2 fluorescence *in situ* hybridization (FISH) between 60-90 minutes fixation with CNB and a traditionally fixed resection. Those breast cancer clinical guidelines and studies indicate that there is a large gap between the acceptable fixation level in some pathology labs (as short as 30 minutes) and the recommended guideline. In other biomarkers tissue studies, consensus is not achieved; thus, generally described with a broad spectrum of fixation times, (e.g., 6 to 48 hours for lung cancer diagnosis [67] and 8 to 72 hours for multiplexed QD ISH assay of ERG and PTEN in prostate cancer [23]). Hence, the significant advantage of our proposed approach of real-time monitoring of fixation level may be supplemented within the streamlined protocols of tissue preparation to investigate the gray area of optimized fixation time, from 0.5 to 6 hours of sample immersion in NBF. Meanwhile, this fixation monitoring system can also offer significant improvement in quality assurance for current histopathology lab environments in which programmed overnight tissue batch processing with an automated tissue processor is common. For example, one sample

of hundreds of tissue cassettes can be extracted from the tissue processor to confirm an optimal fixation level or a small set of CNBs in channels can be monitored during formalin fixation. In addition, our system is also adaptable to the use of a wide range of fixation chemicals from NBF to alcohol mixtures. Although characterizing optimal fixation levels based on the various types, sizes, and heterogeneous nature of tissue in addition to IHC staining methods requires more extensive clinical studies, it is believed that the shear wave LSI system can provide important tissue fixation information for pathologists without making compromises in their clinical timelines and protocols.

2.6 CONCLUSION

We demonstrated the feasibility of the LSI system to measure the change of SWV due to formalin fixation in gelatin phantom and chicken breast. To our best knowledge, the LSI system for SWV measurement in biological tissue, which is strongly scattering and even more during fixation, has not been reported. Furthermore, this is the first reported use of LSI for quantitative monitoring the formalin fixation process, which is a highly sensitive and relatively low-cost optical configuration without experimental complexity of other imaging modalities, such as ultrasound, OCT and MRI. The potential clinical importance of our system is efficiently and reproducibly controlling the gray area of formalin fixation (from the initial 0.5 to 6 hours of tissue immersion) which lays the framework for point-of-care histopathological evaluation in addition to omics biomarker analyses.

Chapter 3. DESIGN AND TESTING OF AN ALL-OPTICAL, LOW-COST FORMALIN FIXATION MONITORING SYSTEM FOR CORE NEEDLE BIOPSIES

3.1 ABSTRACT

Core needle biopsy (CNB) is an important minimally-invasive routine for the diagnostic and therapeutic decisions for cancer. However, the testing results are suffered from the less-standardized and manual tissue processing. Our lab is developing a novel automated millifluidic system, called CoreView [19], which can fulfill the recent trends of low-cost, personalized, and point-of-care testing. In this study, we introduced a new design of a modular device for simple, non-contact, and all-optical measurement to determine full formalin fixation of a CNB. The proof-of-concept study with gelatin phantoms and various porcine tissues successfully showed the feasibility of the real-time in-line monitoring for crosslinking fixation with illumination in a sealed millifluidic chamber, designed for a small CNB. We also fabricated the low-cost and low-manufacturing (3D printing) device that accounts for variations inherent in a multi-hour process without vibration or temperature control. Our new approach and device design can allow low-cost and high-throughput point-of-care diagnostic testing by optimizing turnaround time and standardizing testing results.

3.2 INTRODUCTION

In diagnostic histopathology, the morphological features and immunohistochemistry (IHC) of suspicious disease conditions are routinely performed and adopted as the gold standard, such as

for definitive cancer diagnosis and prognosis. Although the preanalytical variables, such as tissue handling and fixation, are known to adversely affect the diagnostic biomarkers [68], the influence of variations in tissue processing is little known. Biopsies undergo widely different institute-specific protocols because of the different lab environment and workflows. Therefore, non-standardized tissue preparation protocol can yield "false-negative" results [10] and hinder the comparative studies across other facilities. A few guidelines for breast tissue preparation do exist for achieving accurate cancer biomarker labeling. However, the range of allowable processing time is not precise, e.g., 6-72 hours of 10% neutral-buffered formalin fixation for human epidermal growth factor receptor 2 (HER2), estrogen receptor (ER), and progesterone receptor (PgR) labeling [69], resulting in the interlaboratory variations [31,36,70,71]. The research literature has conflicting studies [24–26] , and one claims that the consensus recommendations are not based on the scientific evidence [27]. In order to assess accurate, rapid, and reproducible diagnostic results from biopsy, the standardization of fixation time is strongly recommended [10]. The novel automated core needle biopsy (CNB) millifluidic device under development in our lab [11,12] will provide not only the rapid and less labor-intensive tissue processing and diagnostic features for pathologists but also allow for the control of preanalytical factors. The automated millifluidic device with a completely-enclosed structure will eliminate the contact with biohazardous materials (i.e., formalin and diseased human tissue) during manual CNB handling.

There are a few studies that monitor formalin fixation for biological tissues. Bauer et al. [72] developed an ultrasonic time-of-flight monitoring system that can track the diffusion of formalin. Formalin diffusion was characterized by a decay constant for various human tissues with cold formalin [65]. However, this device was designed to monitor formalin diffusion for a 4 ~ 6 mm-sized biopsy tissue in cold formalin, so it is not feasible for crosslinking monitoring for a CNB.

Ling et al. [58] demonstrated monitoring elasticity changes of 16G CNBs during formalin fixation using optical coherence elastography (OCE). Although the temporal changes of elasticity were obtained from micrometer-resolution OCE images, the biopsy needed to be taken out of formalin and placed on agar gel for the mechanical vibration in direct contact [73]. In our previous study [18] (presented in Chapter 2 in this dissertation), a shear wave laser speckle imaging (SW-LSI) method was introduced to monitor formalin fixation of a CNB in a millifluidic chamber. The mechanical property of a small biopsy tissue was quantitatively measured in terms of shear wave velocity, however, surface contact by a piezo-actuator was required to trigger shear waves in the tissue. Although acoustic radiation force impulse (ARFI) [74] and air-coupled ultrasound [61] may require minimal or no direct contact with a biopsy, the additional components and electronics raise the system cost and complexity.

In our previous study of shear wave laser speckle imaging (SW-LSI) to monitor the fixation level in millifluidic channels [18], the change of the optical property was observed during formalin fixation. Other studies also reported related findings from different measurement systems. Hsiung et al. [75] used optical coherence tomography (OCT) imaging at 800nm to demonstrate the effect of formalin fixation in the hamster cheek pouch *in vivo*. The shrinkage and optical scattering change for the microstructure of the cheek pouch tissue after formalin fixation of 30 minutes, 1, 2, 4, 8, 12, and 16 hours were examined qualitatively. Wood et al. [76] reported the bulk optical properties of porcine myocardium and liver tissues. The linear retardance and depolarization as well as scattering at 635nm were increased by the effect of 1 and 6 days formalin fixation. Pitzschke et al. [77] presented long-term fixation effect on rabbit brain at 635nm, 671nm, and 808nm, and the overall effective attenuation coefficients were increased by 5 to 15% after 6-weeks of formalin fixation. Anand et al. [62] investigated the optical property changes in brain tumor

tissues after 1-week of formalin fixation using diffuse reflectance spectroscopy. Authors reported that the hemoglobin bands at 540nm and 580nm in the fresh brain tissue disappeared due to hemolysis by formalin, and the spectrum greater than 650nm showed increased scattering in formalin-fixed samples. These prior studies investigated the effect of formalin fixation for limited fixation durations, tissue types, or optical spectra. All previous measurement methods required the surface of tissue specimens to be exposed to an open space [62,75–77], by which formalin fixation either stops or pauses after certain times. The direct contact of one [62] or multiple probes [77] to the tissue were even needed for the optical property measurements. Most importantly, none of previous approaches are suitable for the spectro-temporal study of a CNB during continuous formalin fixation. Therefore, in this study, we design and test a non-contact all-optical monitoring for "bulk optical transmittance" for a CNB during formalin fixation within a millifluidic chamber. We first conducted a spectral optical transmittance measurement for tissue mimicking phantoms and various porcine tissues during formalin fixation. And to demonstrate the feasibility for integration with the automated millifluidic device, a 3D printed prototype system was designed and fabricated with a minimal set of optical components: a laser diode (LD) module, a beam splitter, pinholes, neutral density filter (NDF) and photodiodes.

3.3 MATERIALS AND METHODS

3.3.1 *Sample preparation*

We chose gelatin tissue phantom and various porcine organ tissues. The gelatin tissue phantom was made of dried gelatin from porcine skin (Sigma-Aldrich, 300 Bloom) at the mass concentration of 6%, mixing with distilled water and titanium dioxide (TiO_2 18nm, US Research Nanomaterials, Inc.). The mixture was heated to 80 degC with a magnetic stirrer until all gelatin powder was completely dissolved. The mixture was cooled to 37degC before pouring into a small petri dish. In order to minimize the settlement of insoluble TiO_2 particles, the petri dish was kept in a freezer for 3 minutes for rapid congealing. The porcine organs (mammary, liver, spleen, pancreas, and lung) were supplied from the Harborview Research & Training Veterinary Services at the University of Washington. Discarded fresh organs were collected and kept in a refrigerator up to three days before used for this study. The portions of the porcine tissues were stored in a freezer and the mammary tissues were later thawed and used for a CNB procurement that was used for the feasibility test of a 3D printed prototype system.

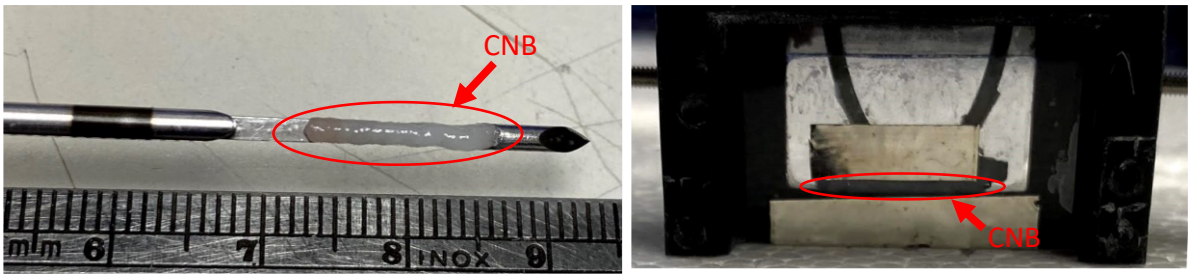

(a) (b)

Fig. 3.1 (a) Porcine breast CNB sat in the 14G biopsy needle (nominal inner diameter: 1.6mm) after procurement (b) The CNB placed in the millifluidic cartridge. The lid with legs guided the CNB to the bottom of the chamber where the laser beam passes through.

The thickness of tissue and phantom samples was controlled to 3mm (± 10 %), and the samples were placed in a formalin-filled chamber within 30 seconds after sectioning. The transmittance data were recorded every 10 minutes up to 10 hours (porcine tissues) and 20 hours (gelatin phantoms).

To test the 3D printed optical station, we used porcine breast CNBs from frozen tissues. The frozen tissue was thawed and warmed at 30 degC for a similar body temperature condition. A 14G spring-fired biopsy needle (1416MS, Bard14G core needle biopsy, C. R. Bard, Inc.) was used to procure a CNB from porcine breast tissues. Fig. 3.1 (a) shows the CNB taken by the biopsy needle. The fatty areas were mostly taken for the CNBs, but a small portion of glandular and connective tissues was appeared.

3.3.2 *Broadband optical transmittance measurement setup*

For the optical transmittance measurement of a CNB in millifluidic chamber, we set up the testing station using a tungsten-halogen light source (LS-1, Ocean Optics, Inc) and a spectrometer (USB

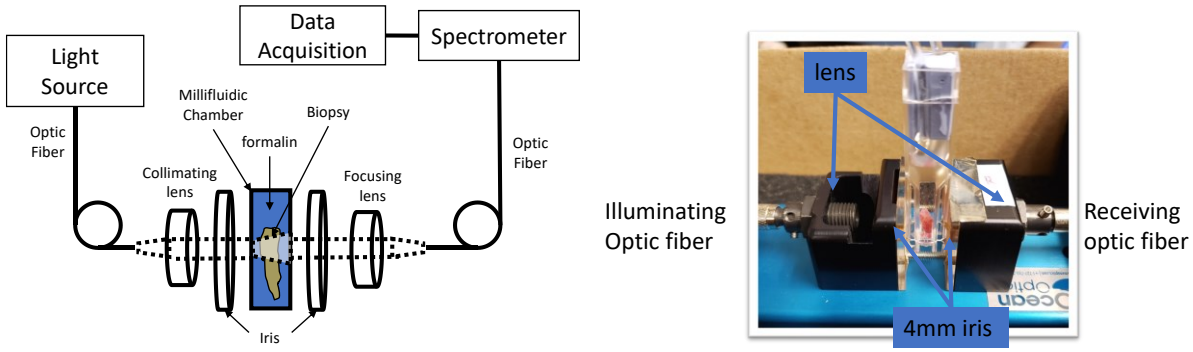

Fig. 3.2 (a) A schematic of optical transmittance measurement setup. (b) A breast biopsy was placed in the millifluidic chamber. The optic fibers connected to both ends with lenses. The top cap of the chamber included the tubes for formalin circulation.

2000, Ocean Optics, Inc). Fig. 3.2 shows the experimental setup for this preliminary study. The light beam focused into a 200um optical fiber cable, which collimates and cut out to a beam diameter of 4mm. The beam passed through a 4mm sample slot is collected by a 1mm optical fiber

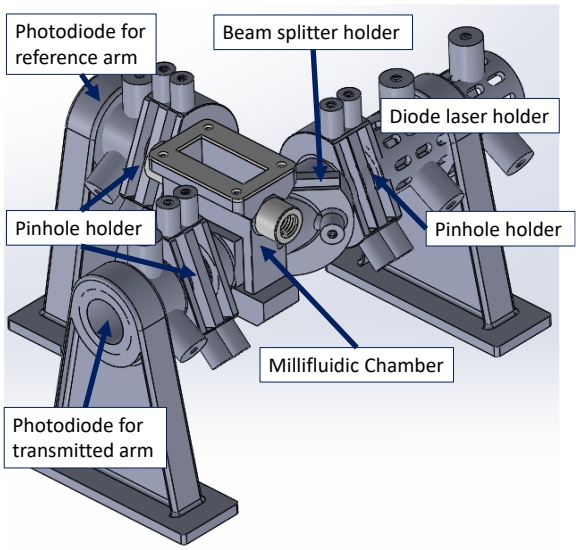

(a)

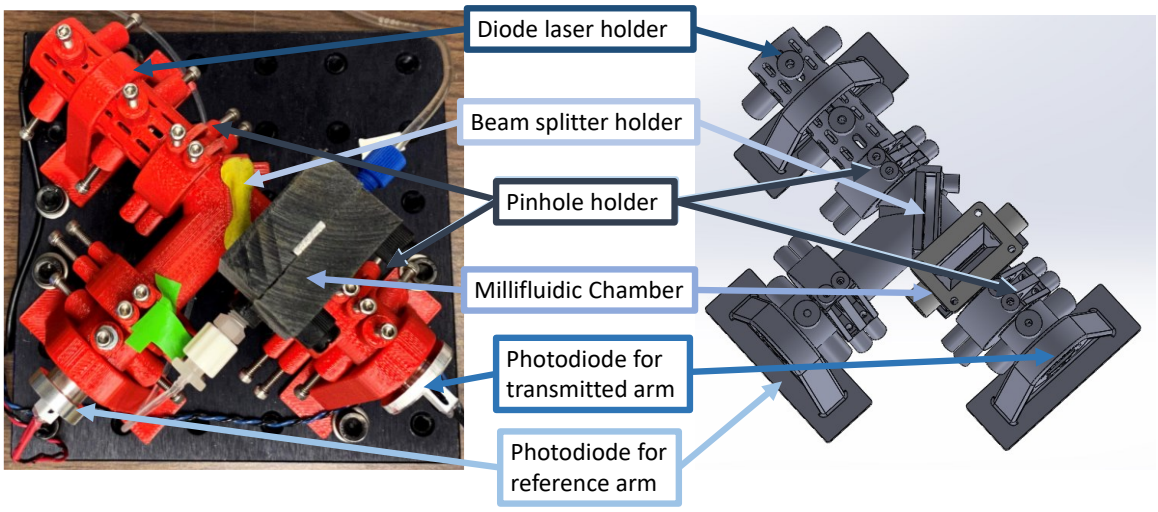

(b) (c)

Fig. 3.3 The 3D printed millifluidic fixation monitoring system. (a) A rendering work of the optical station for 3D printing. (b) The 3D printed optical station (c) The front view of the millifluidic chamber

cable for the spectroscopy. For the data acquisition and processing, a custom MATLAB-based graphical user interfaces (GUIs) were generated.

3.3.3 *3D printed optical station for prototyping*

Based on the preliminary experiments with the broadband light source and spectroscopy, we designed a low-cost and rapid prototyped optical transmittance monitoring system for a CNB in millifluidic channels. Using off-the-shelf optical components and 3D printing techniques, we rendered the optical station design, shown in Fig. 3.3 (a), and fabricated the 3D printed optical transmittance monitoring system for CNB fixation, shown in Fig. 3.3 (b-c). The main body of the optical station was fabricated by fused deposition modeling (F170, Stratasys, Ltd.), and the millifluidic cartridge was printed via stereolithography (Photon, Anycubic, Shenzhen, China) process. A single wavelength LD module (808MD-300-1245, Laserlands, Wuhan, China), two PIN photodiodes (SFH-203-P, Osram Opto Semiconductors GmbH, Regensburg, Germany), and a beam splitter (#68-368, Edmond Optics, Barrington, NJ) were embedded in the optical station. The LD module emitted a collimated rectangular beam at 808nm, which was trimmed down to 1mm in diameter. A beam splitter reflected a reference beam by 90 degrees for compensating for laser intensity instability in real time. The transmitted beam passed through the optical cartridge in which a 2.2mm wide millifluidic chamber was placed. Both reflected and transmitted beams were each aligned to a silicon PIN photodiode detector. Photodiode signals were amplified by op amp circuits and digitized with a 14-bit analog-to-digital converter (USB-6009, National Instruments Corporation, Dallas, TX), using customized LabVIEW codes for data acquisition and system control.

The millifluidic cartridge included two fluid ports, which enabled formalin circulation during the experiments. A piezoelectric diaphragm pump (mp6, Bartels Mikrotechnik GmbH, Dortmund,

Germany) with a micropump controller (mp-x, Bartels Mikrotechnik GmbH, Dortmund, Germany) circulated total formalin volume of 4 ml at the rate of 2 ml/minute. The lid of the cartridge was designed to secure a CNB on the bottom of the chamber. The prototype millifluidic chamber can be replaced with a square millifluidic glass channel for the automated millifluidic device.

3.3.4 *Relative change measurement of optical transmittance*

In our study, the relative change of optical transmittance of a CNB was measured over the time course of formalin fixation. The optical properties including absorption and scattering that vary by the geometry and the preparation condition of tissue are not our focus here. Therefore, our aim was to pursue the measurement of relative temporal changes in optical transmittance. We conducted the monitoring measurements for 10-hour fixation for porcine tissues and 20-hour fixation for gelatin phantoms to characterize the bulk chemical and physical effect of formalin fixation. In order to compare the formalin fixation effects among other phantoms and tissues, we have closely examined the near-infrared (NIR) region, primarily at 808nm, for optical transmittance within the 3D printed system.

3.4 Results and Discussions

3.4.1 *Optical transmittance changes by formalin fixation*

3.4.1.1 Gelatin phantom

The temporal change of optical transmittance spectrum during formalin fixation is shown in Fig. 3.4. The rapid increase of the optical transmittance for the first 32.5 ± 8.3 minutes was observed. The peak transmittance after the rapid increasing period was chosen as a reference. The spectral change of transmittance profiles at every 100 minutes were shown for 20-hour formalin fixation. The gelatin phantom did not show particular spectral characteristics during fixation except for a gradual opacification, which was expected from a homogeneous gelatin mixture with a single scattering agent, TiO2. The fixed phantom showed less transmittance changes in the longer wavelength region (27.5% decrease at 550nm, 24.6% decrease at 808nm, and 22.4% decrease at 950nm. We then looked at the NIR region at 808nm (averaged between 800nm and 816nm) as shown in Fig. 3.4 (b). Four experiments were conducted, and the relative spectral change of

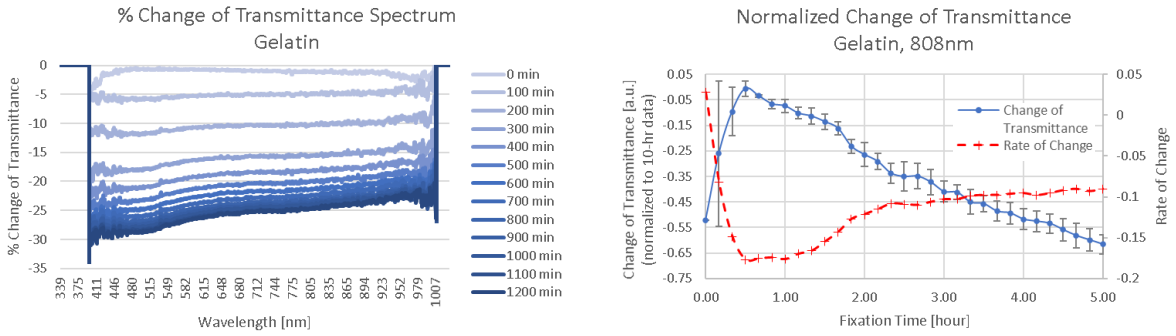

(a) (b)

Fig. 3.4 (a) The temporal spectrum of the change of transmittance for typical gelatin phantom. 20-hour spectra are shown at the interval of 100 minutes. (b) The temporal change of transmittance at 808 nm (blue). The slope of the temporal change (red).

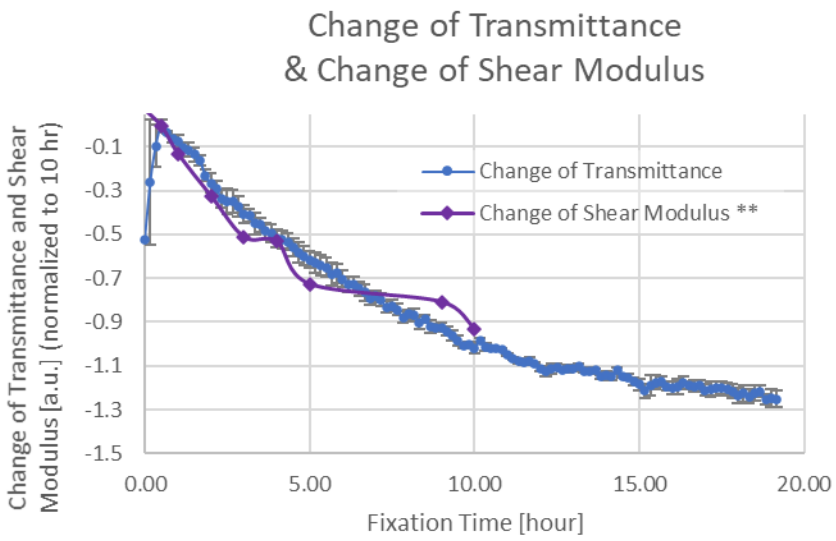

Fig. 3.5 Comparison between the change of transmittance and the change of shear modulus from [15]. Shear modulus was converted from shear wave velocity and then normalized with respect to the 10-hour fixation. The intercept for the change of shear modulus was introduced (0.14 at t=0) in order to offset the diffusion time.

transmittance was normalized to the time point of 10-hour fixation gelatin phantoms. The formalin fixation quickly reached the peak of transmittance, and gradually decreased. It was not obvious that the transmittance change slowed down over time. However, the rate of change (a red line) in Fig. 3.4 (b) indicated that the further fixation after 2 hours occurred at a slower speed. The optical transmittance did not reach the plateau after 20-hour fixation, but the speed of change gradually decreased. This slow and continuous effect of formalin (the rate of transmittance < 0.1 after 3-hour fixation, < 0.05 after 10-hour fixation) was in agreement with our previous study that assessed the mechanical property change in a 6% gelatin phantom [18]. The shear wave velocity measurement study during formalin fixation is presented in Chapter 2 Fig. 2.5 (a). Fig. 3.5 compares the change of transmittance with the change of shear modulus from [18]. The change of shear modulus was converted from the shear wave velocity values that were measured from a 6% gelatin phantom at

the depth of 1.5mm, which is equivalent to the half-thickness of a 3mm thick gelatin, up to 10-hour formalin fixation. The number of data points and the time range may be insufficient to demonstrate a high degree of correlation for the entire fixation process (Fig. 3.5); however, the change of optical transmittance appears to follow the normalized change of mechanical property in a gelatin phantom. It is shown that formaldehyde crosslinking alters both mechanical and optical properties of the tissue to the comparable levels in the normalized measurements. Further study on the physical mechanism of chemical crosslinking is, however, required to explain this finding.

3.4.1.2 Porcine tissues

The transmittance changes for the porcine tissues at 3mm thickness were also measured in the same way as described for the gelatin phantom. The transmittance was changed at a rapid rate for the first 1 to 5 hours and reached to the plateaus before 10-hour fixation. Fig. 3.6 shows the temporal spectra of the change of transmittance for porcine organ tissues: (a, f) Pancreas (three datasets), (b, g) Breast (one dataset), (c, h) Liver (three datasets), (d, i) Spleen (two datasets), and (e, j) Lung (two datasets).

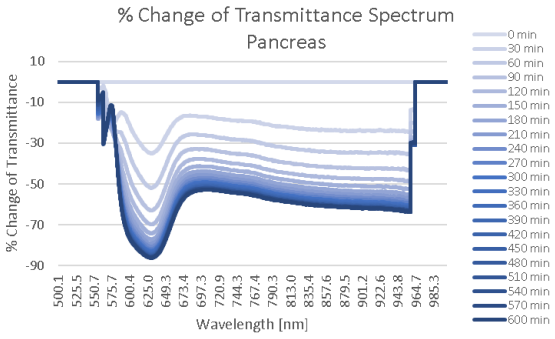

(a)

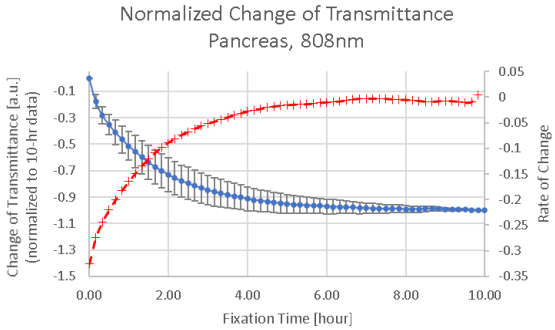

(f)

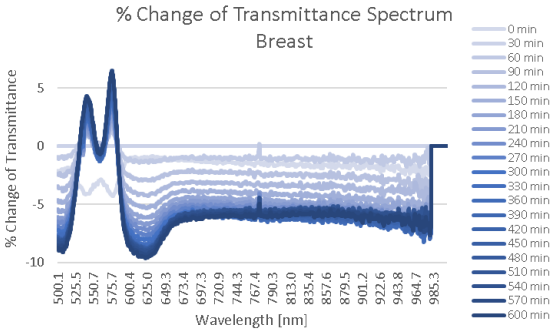

(b)

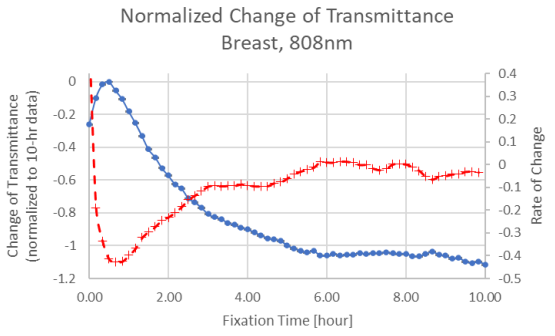

(g)

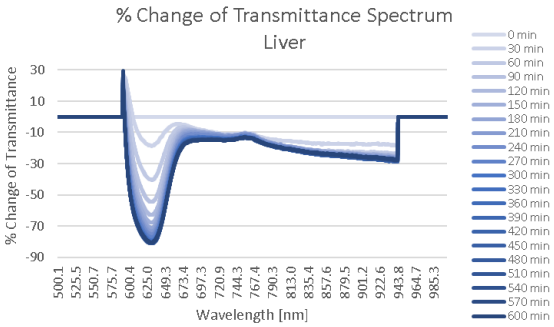

(c)

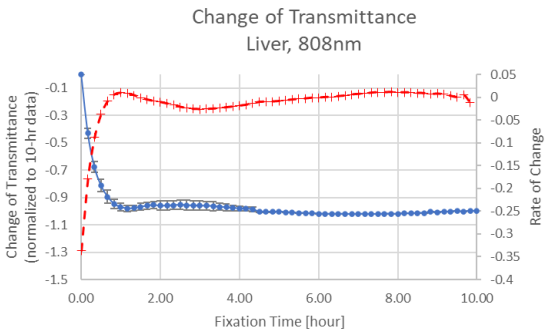

(h)

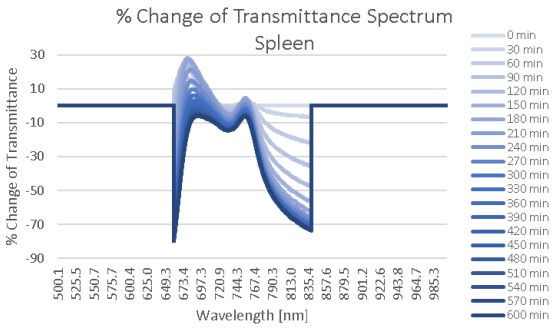

(d)

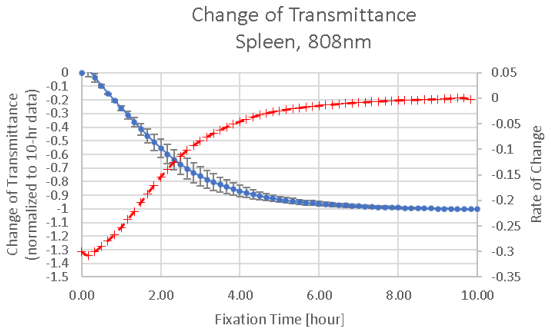

(i)

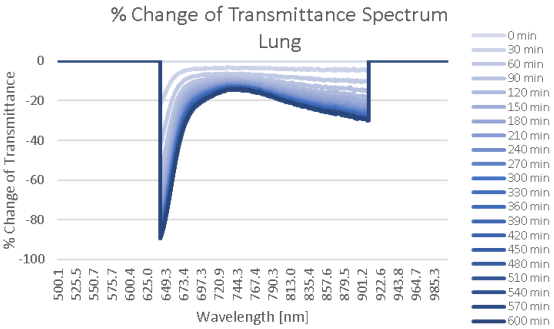

(e)

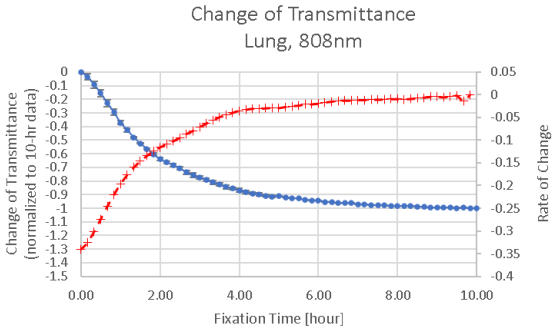

(j)

Fig. 3.6 (a-e) The temporal spectrum of the change of transmittance. 10-hour spectra are shown at the interval of 30 minutes. (f-j) The temporal change of transmittance at 808 nm (blue). The slope of the temporal change (red); (a,f) Pancreas, (b,g) Breast, (c,h) Liver, (d,i) Spleen, (e,j) Lung.

3.4.2 *Diffusion*

The gelatin phantoms showed the initial optical clearing in the first 32.5 ± 8.3 minutes (a magnified version of Fig. 3.4 (b) is shown in Fig. 3.7 (a). When a gelatin phantom made of gelatin powder, distilled water, and optical scatterers is first exposed to formalin, the formalin diffuses quickly due to a high osmotic pressure gradient. The physical artifacts and slight dehydration during the sample sectioning and handling may also contribute to some extent.

The similar phenomenon can be also found from porcine breast tissue in Fig. 3.6 (g). The breast biopsy was mostly made up of fatty tissue, which is less scattering than other tissues. Other than breast, porcine tissue samples did not show the initial transmittance improvement. Lerch et al. [65] reported the first-order decay constants collected for various 6mm-sized human tissues using a

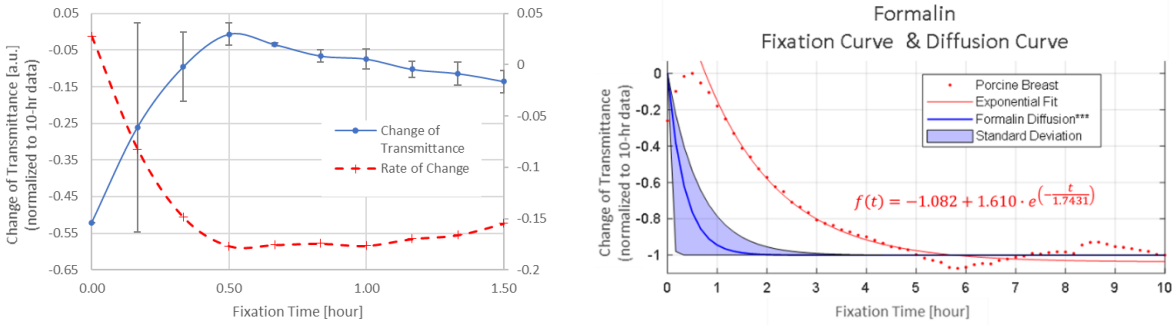

(a) (b)

Fig. 3.7 (a) A magnified version of Fig. 3.4 (b). The temporal change of transmittance of the gelatin phantom at 808 nm (blue). The slope of the temporal change (red). The first 1.5 hours graph is shown for a diffusion step. (b) The change of transmittance of porcine breast tissue and the formalin diffusion curve of human breast tissue. The change of transmittance graph (red dot) from Fig. 3.6 (g) with an exponential fitting curve and equation (red line and font). The formalin diffusion curve (blue line, [65]) and the standard deviation (blue shade) of human breast tissue are overlaid.

time-of-flight (TOF) monitoring system [72] for temporal formalin diffusion progress in tissue. In Fig. 3.7 (b), the decay constant and its standard deviation from normal human breast tissue [65] were overlaid with the normalized change of transmittance data from porcine breast (Fig. 3.5 (g)). The decay constant presented by Lerch et al. was measured from 6mm-sized samples, therefore, the adjustment for a 3mm-sized sample was made by the Fick's 2nd law, which describes the proportional relationship between diffusion depth and time for the same change of formalin concentration, $DC_b = DC_a \cdot \left(\frac{{\delta_a}^2}{{\delta_b}^2}\right)$, where DC is a decay constant and its subscript (a or b) represents the different thickness, δ, of a sample. The decay constant for human breast at 6mm thickness is 1.38 [hour] [65], and the adjusted decay constant in Fig. 3.7 (b) is 0.345 [hour]. The time for 95% of formalin diffusion was estimated to occur after 1.03 hours, shown as a black dot in Fig. 3.7 (b). Although it is not fully explained only by formalin diffusion, the overlapped time frame of formalin diffusion profile in Fig. 3.7 (b) implies that the refractive index change by formalin diffusion may play a significant role during the initial optical clearing. And based on the implication, a peak point after the initial rapid diffusion was chosen for the starting reference data point.

The porcine breast datapoints were then fit in to an exponential fitting curve, $f(t) = C + A \cdot e^{(-\frac{t}{\tau})}$, after the completion of 95% diffusion of formalin (a red line in Fig. 3.7 (b)). The exponential curve was a good fit at the R-squared of 0.984, which represents that the temporal progress of formalin fixation without the effect of diffusion also follows the exponential decay. It should be also noted that there are sampling errors from the comparison between porcine and human tissues and the different breast compositions (fibrous, fatty, and glandular tissues).

3.4.3 *PBS rinsing effect*

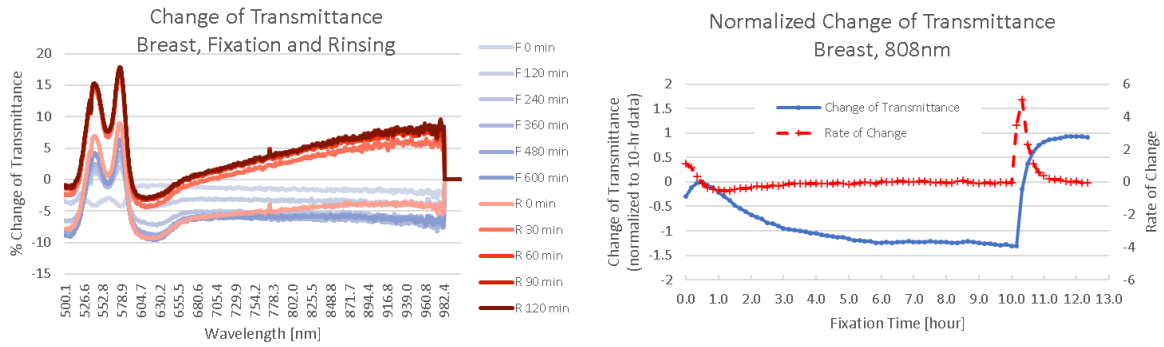

(a) (b)

Fig. 3.8 (a) The temporal spectrum of the change of transmittance. Formalin fixation step in blue and PBS rinsing steps in red. 10-hour spectra are shown at the interval of 120 minutes for formalin fixation and 30 minutes for PBS rinsing. (b) The temporal change of transmittance at 808 nm. After 10-hour fixation, formalin was replaced with PBS.

Formalin fixation has been known as a two-step process of diffusion and crosslinking. For the crosslinking step, the formation of reactive hydroxymethyl side groups (-CH_2-OH) and its adducts are closely involved in a short-term relatively weak crosslinking (hours to days) while the strong and stable crosslinks take significantly longer fixation time (weeks to months) [78,79]. Such early stage fixation was confirmed to be reversed by long-term rinsing [80]. In order to explore whether reversing fixation by rinsing can be shown in our measurement, we performed phosphate-buffered saline (PBS) rinsing to the 10-hour fixed breast tissue (Fig. 3.6 (g)). After 10-hour formalin fixation, the formalin in the millifluidic chamber was replaced five times with PBS by a micropump. The change of transmittance was rapidly reversed in direction as shown in Fig. 3.8 (a), and the effect of rapid PBS rinsing was stabilized within 90 minutes in all wavelengths. The time to plateau took roughly 60 minutes, 80 minutes, and 90 minutes for 550nm, 808nm, and

950nm, respectively. The overall spectrum profile shape was not significantly changed, indicating that the highly absorbing hemoglobin bands permanently disappeared during the formalin fixation. The optical transmittance was also increased more than the pre-fixed condition by 9% due to the absence of blood, which was denatured and diluted by formalin. Any changes in transmittance by switching over from formalin to PBS, such as refractive index change, would immediately occur, therefore, the overall spectral changes up to 90 minutes of PBS rinsing may be explained by fluid replacement in tissue. The rapid formalin diffusion time of 30 minutes in porcine breast (Fig. 3.6 (g)) was driven by strong osmotic pressure (about five times that of physiological salt solution) [20], therefore, up to 90 minutes of PBS rinsing for the fixed tissue seems a reasonable time period for diffusion. The reversal of chemical fixation (crosslinking) by rinsing takes over days and weeks [80]. Therefore, the rinsing result of the optical transmittance which reaches the plateau within 90 minutes seems to be largely due to the refractive index change (fluid replacement) while both diffusion and crosslinking were measured during the early stage of formalin fixation. However, further investigation will be needed to find how the effect of short-term rinsing on the tissue's optical transmittance may also be affected by the crosslinking condition and structural change (e.g., swelling) in addition to the refractive index change of the tissue.

3.4.4 *Absorption of various solutions*

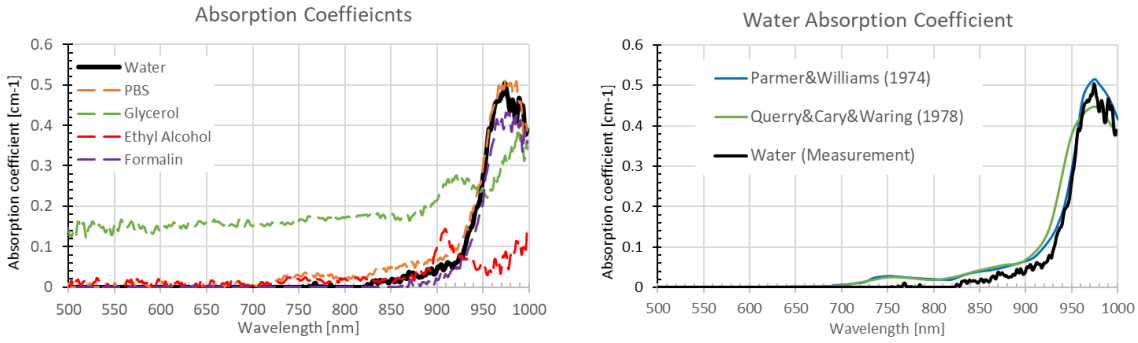

(a) (b)

Fig. 3.9 (a) Attenuation coefficients of various lab solutions (b) Water attenuation coefficient comparison with previous reference data

Our measurement system was designed for relative bulk optical property measurement during formalin fixation, not for the absolute optical properties such as absorption or scattering coefficients. However, we attempted to check the sensitivity and validity of the system for optical property measurement. The attenuation coefficients of various solutions were estimated from optical transmittance using Lambert-Beer Law. Fig. 3.9 shows (a) the attenuation coefficients for water, PBS, glycerol, ethyl alcohol, and formalin, and (b) the attenuation coefficient of water with the references [81,82]. Although the spectral attenuation coefficient plot for water is close to the references, it does not indicate that our system can measure absolute optical properties for bulk tissue or other materials. For a bulky biopsy sample, the beam passed through a sequence of media, i.e., optical window - formalin - sample - formalin - optical window. Therefore, our results are not comparable to other studies that used the double-integrating sphere or diffusive reflectance methods.

3.4.5 *Variation between samples*

The thickness of biopsy samples was set to 3mm for optical transmittance experiments. However, the variation in actual thickness about ± 10% was unavoidable during sample preparation due to the viscoelasticity, heterogeneity, and deformability of tissues in the *ex vivo* condition (no internal stress). And the heterogeneous tissue structures, especially connective tissue, were also observed in all tissue types, which yielded structural distortion in a post-fixation condition, shown in Fig. 3.10. Gelatin phantoms showed a more homogenous structure, however, its adhesiveness and fragility often generated fragmented surfaces or cracks. Thus, absolute transmittance value may be unpredictable due to those various factors originated from the nature of samples and the structural uniqueness from sample preparation. In these measuring circumstances, a relative change analysis, which focuses on the gradual change of the optical transmittance over time, can effectively reject uncontrolled errors, and provide a valuable monitoring capability of our system for the chemical and physical conditions of CNB in millifluidic channels. For example, the

Fig. 3.10 Various porcine tissue after 10-hour formalin fixation (above) and the color of used formalin (below). All tissues with clean cut before fixation demonstrated the shrunk shapes after fixation. The connective tissue appeared to produce a significant distortion.

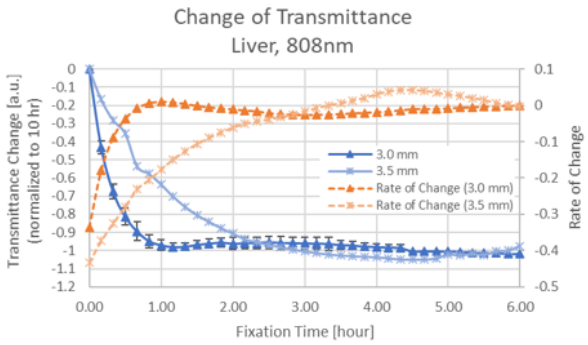

Fig. 3.11 Temporal change of transmittance at 808nm for porcine liver tissues at different thickness. The rate of change for each thickness is in orange dashed line.

substantial CNB motion artifacts were simulated by repositioning the CNB during the optical transmittance measurement. The temporal change of optical transmittance (i.e., Fig. 3.6 (a)-(e)) varied by up to 10% after the sudden position change. However, the slope of temporal change (i.e., the rate of change in red lines in Fig. 3.6 (f)-(j)) shows the motion-insensitive results except for an impulse outlier at the time of motion artifact. The robustness of relative change analysis can be shown with different thickness of samples. Fig. 3.11 shows the example of formalin fixation monitoring for different sizes (3.0 mm and 3.5 mm) of liver tissues. The thickness difference of 0.5mm was distinguished in the results as the thicker sample took more time to reach the plateau after 2-hour fixation (vs 1-hour fixation for the 3mm thickness sample).

3.4.6 *3D printed prototype optical station*

3.4.6.1 System Testing - Breast (Porcine)

Fig. 3.12 shows the change of transmittance data from three porcine breast CNBs. External noises from the laser source instability and background environment were compensated by the reference photodiode. The transmitted signal in volts was normalized with respect to 3-hour fixation data

point, where the definite plateaus of the signals were presented. The average and standard deviation of three CNBs were also plotted in Fig. 3.12. For the plotting purpose, the 10-hour experiments were truncated to 3-hour data and the interval of data points was increased to 5 minutes from 1 minute.

3.4.7 *Spectral Characteristics*

Our spectrum data for the change of transmittance demonstrated similar and dissimilar profiles among the various porcine tissues. To the best of our knowledge, little has been investigated for the spectral effects on tissue due to formalin fixation. One study by Anand et al. [62] presented the reflectance spectra between freshly excised and formalin fixed brain samples. Anand et al. reported

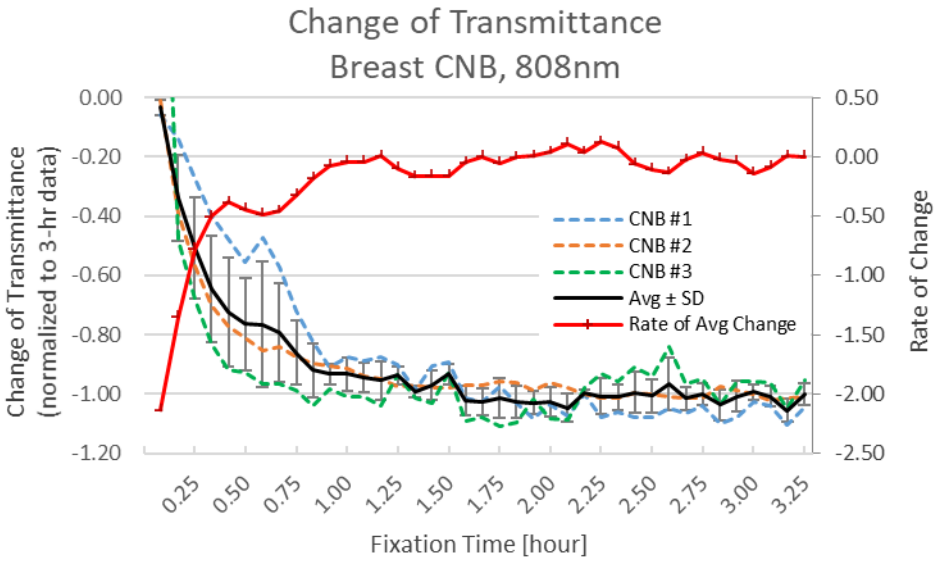

Fig. 3.12 The temporal change of transmittance from three porcine breast CNBs. The average with standard deviation (error bars) is plotted in a black line. The slope of the temporal change for the average is shown in a red dotted line. The time interval of the data was down-sampled to 5 minutes from 1 minute and from 10 hours total.

that the characteristic bands of hemoglobin between 540 and 580nm completely disappeared after formalin fixation, which was also demonstrated in our porcine breast cases (Fig. 3.6 (b) and Fig. 3.8 (a)). The significant transmittance losses between 600 and 650nm were observed in all porcine tissues. It is likely that denatured red blood cells are absorbing because the transmittance drops between 600 and 650nm were considerably greater in the tissues with high blood content (-88% in pancreas, -81% in liver, -80% in spleen, and -91% in lung, vs -9% in breast). In addition, similar to the hemoglobin band between 540 and 580nm, the spectral effect between 600 and 650nm was retained after PBS rinsing. However, at this point, no clear evidence or explanation is available.

3.4.8 *Summary*

The feasibility of using the relative change in optical transmittance to gauge the level of fixation was presented by categorizing each phase of formalin diffusion, initial crosslinking, and the saturation of crosslinking, as shown in Fig. 3.13. Because of a lack of relative studies, a comparable study for the spectral change of optical property due to formalin fixation is unavailable. However, it is clearly shown that the effect of formalin fixation, regardless of physical or chemical changes, can be monitored by the optical transmittance change. In addition to formalin fixation (crosslinking), the effect of formalin diffusion and PBS rinsing were also represented in terms of the optical transmittance. Those effects were shown within a short period time (diffusion in 30 minutes, rinsing in 90minutes). Hence, our results of the change of transmittance over a time course of hours (time to plateau shown in Fig. 3.4, Fig. 3.6, and Fig. 3.12) could be associated with the effects of tissue crosslinking rather than formalin diffusion.

Our 3D printed optical station was tested with a 14G CNB, which has an equal or less than 1.6mm in diameter, and the formalin fixation monitoring feature was successfully demonstrated as shown in the proof-of-concept experiments with a 3mm tissue sample. The test results were from three

different porcine breast CNBs, shown in Fig. 3.12, in the most consistent way; visually sorted intact CNBs that are mostly consisting of fat, without connective or glandular tissue.

The purpose of this modular optical system is to provide a fixation monitoring function for an individual CNB, which holds unique geometry and content. Based on our results, our optical transmittance measurement approach shows great potential to monitor the formalin fixation of 3mm-sized tissues. Further, the 3D printed optical device was fabricated, and tested feasible to reproduce the experiments with a 14G porcine breast CNB, that measures the expected shorter fixation time (< 2 hour). With our new non-contact all-optical fixation monitoring system, a CNB is completely enclosed in the millifluidic chamber, therefore, manual CNB handling and hazardous formaldehyde exposure can be avoided. In addition, the significant cost saving (from a few thousands of dollars to less than a hundred dollars) and the compact form factor (less than $15\times15\times15$ cm^3) of the system can be achieved by using cost-effective 3D printing technique and basic electronic and optical components when compared to our previous approaches with an OCT system [11] and a SW-LSI system [18].

3.5 CONCLUSION

We have examined the effect of 10-hour formalin fixation on the optical properties of gelatin tissue phantoms and porcine tissues of the size that is relevant to CNB specimens. The preliminary testing for the spectral optical transmittance changes during the formalin fixation showed the irreversible hemoglobin denaturation and the decrease of the optical transmittance in the overall VIS-NIR spectral range. Then, we designed and fabricated a 3D printed optical fixation monitoring system that can be integrated to the automated CNB millifluidic system for point-of-care pathology assessments. Our new simplified low-cost system which is all-optical was tested with porcine breast CNBs (14-gauge), which clearly showed similar fixation level profile within a shorter time than the 3mm samples. We believe the automated CNB millifluidic device will process CNB more accurately, rapidly, and consistently for pathologists to diagnose a disease and determine further therapeutic decisions. Finally, the proposed 3D printed optical monitoring system will bring a reliable monitoring module to optimize the tissue preparation process as part of the millifluidic

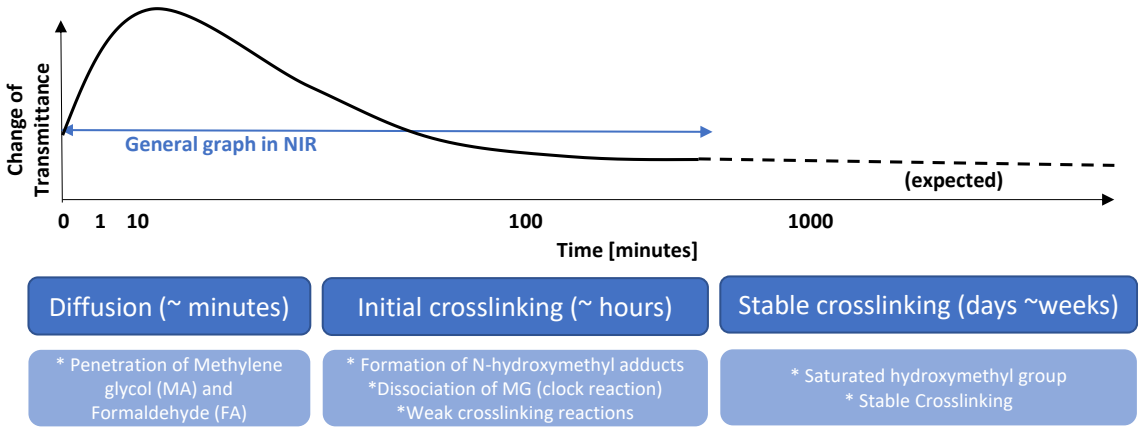

Fig. 3.13 A typical graph of the change of transmittance for a small biopsy < 3mm or CNB. Time is log-scaled for visual demonstration.

system under development. Rapid and well-controlled CNB processing without professional manual handling will enable a step forward into point-of-care testing. In addition, in the future design, a standalone battery-powered CNB monitoring system will show a great potential for the safe and secure CNB transport and storage.

Chapter 4. DESIGN OF NEW MILLIFLUIDIC SYSTEMS FOR POINT-OF-CARE PATHOLOGY USING CORE NEEDLE BIOPSY

In this chapter, the innovative design and operational approaches of our new formalin fixation monitoring system presented in Chapter 3 are proposed to enhance its integration and operation with the automated millifluidic system ("CoreView millifluidic system") [19] for pathology. The automated millifluidic system, CoreView, still requires manual CNB procurement and shipping: from a patient to a biopsy needle, from the needle to a millifluidic chamber, and from the chamber to a millifluidic device. For some situations, the CNB may be even stored in formalin while shipping to laboratory sites. Thus, the time recording and CNB monitoring should be initiated from the time of tissue collection to control and standardize the tissue preparation. The novel feature of the CoreView system is to automate the CNB processes for the accurate and rapid on-site evaluation. While rapid tissue fixation using coagulative fixatives (e.g., ethanol) for some analyses, such as flow cytometry, can be an option to reduce the turn-around time at the PoC, formalin fixation is still the gold standard in biopsy studies. And the importance of the archived formalin fixation paraffin embedded (FFPE) tissue specimens for therapeutic and proteomic studies has been raised [16,17]. In the following section, the end-to-end protocols of CNB procurement, transporting, and formalin fixation monitoring are discussed with the goal of future integration with the CoreView system.

4.1 CNB PROCUREMENT AND REMOVAL

A CNB is taken from a patient using a biopsy gun, by which a cylindrically cut CNB is obtained in the hollow needle. The biopsy needle is inserted to a millifluidic tube where a push bar manually

removes the CNB from the needle and locates it in the millifluidic chamber, as shown in Fig. 4.1 (a). Another CNB removal approach is to make use of millifluidic flow [19]. The fixation monitoring system includes a diaphragm millifluidic pump for formalin circulation, and the CoreView system uses the controlled pulsatile flow for CNB transport within the millifluidic channels. Therefore, the CNB can be removed and transported to the monitoring areas by those sources of the millifluidic flow pressure, as illustrated in Fig. 4.1 (b). The CNB collection kit is filled with fresh formalin 20 times more volume than the CNB. Once a CNB is placed at the

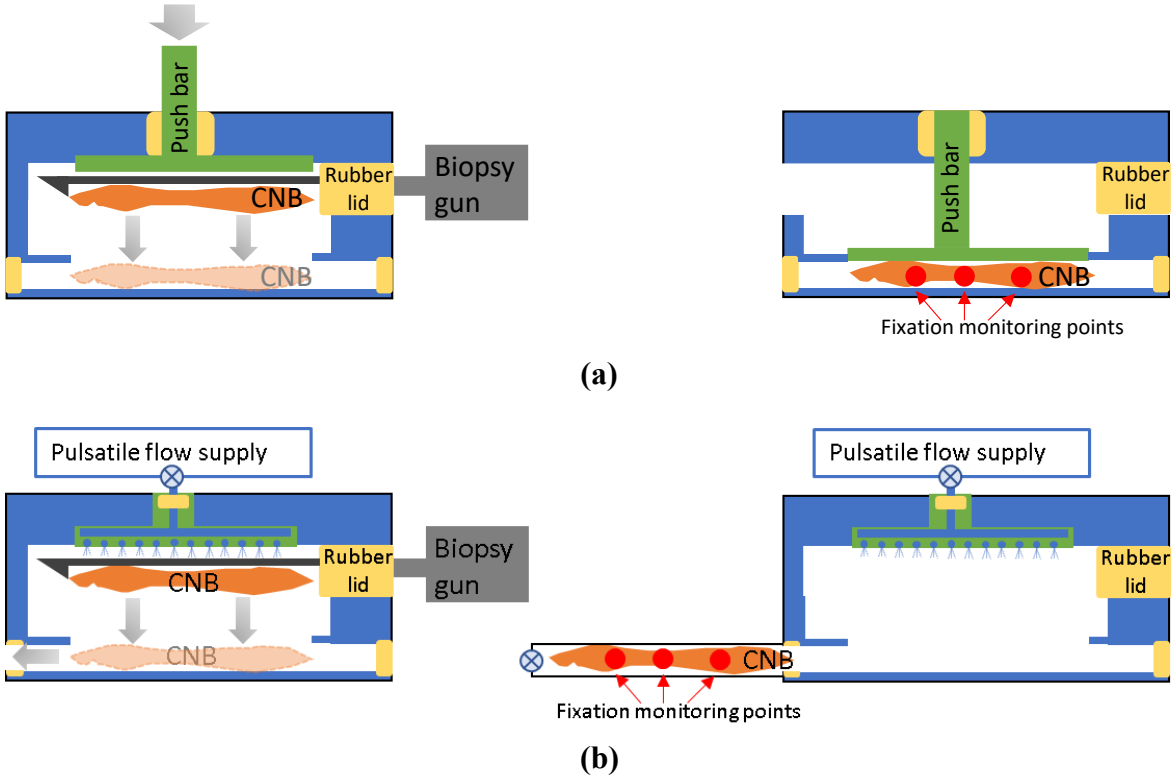

Fig. 4.1 CNB removal methods (a) A manual push bar positions the CNB to the millifluidic channel (b) Pulsatile flow transports the CNB to fixation monitoring area. Illumination fixation monitoring begins after the biopsy needle is removed from the CNB collection kit.

millifluidic channel area, the collection kit is installed in the 3D printed fixation monitoring system, shown in Chapter 3 Fig. 3.3.

4.2 TIMELY DISTRIBUTION AND RECOLLECTION OF A CNB FOR POINT-OF-CARE

Monitoring formalin fixation of a CNB for the PoC diagnosis provided by the CoreView system can be achieved by integrating the modular fixation monitoring system with the CoreView. Multiple CNBs can be simultaneously processed in each modular millifluidic chamber while the time and level of CNB fixation are monitored (Fig. 4.2). The millifluidic flow delivers the CNBs which are ready for further processes in the CoreView system. The modular fixation monitoring

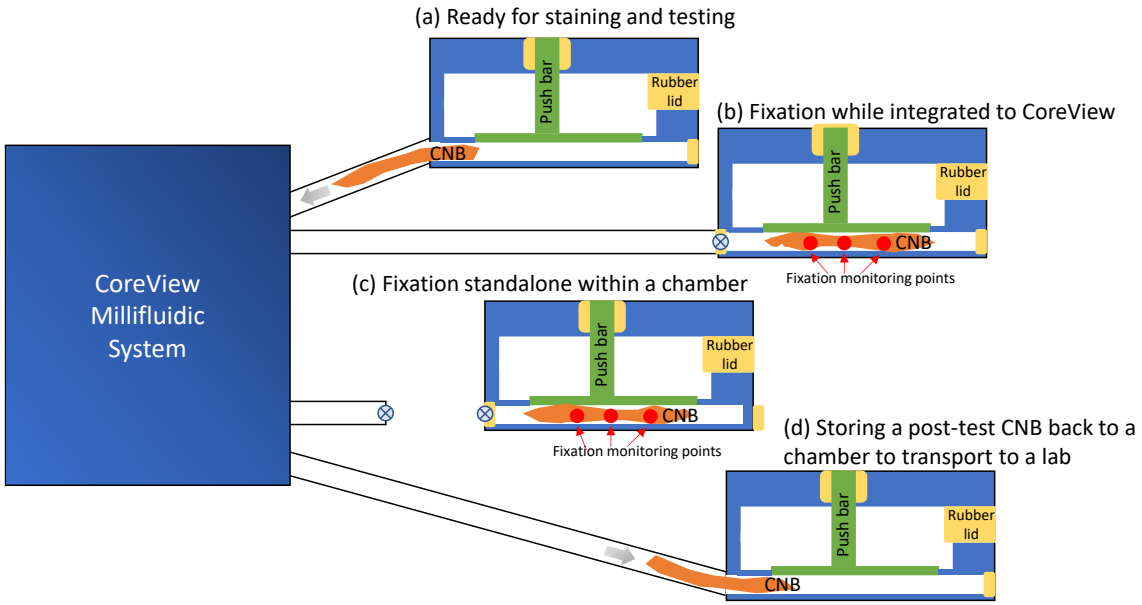

Fig. 4.2 Schematic of the CNB fixation monitoring system. (a) An optimally fixed CNB is transported to the CoreView via millifluidic channels. (b) A CNB is being fixed in the monitoring system which is integrated with the CoreView. (c) A CNB is being fixed in the monitoring system in a standalone mode. (d) After PoC testing, the processed CNB is stored back in the modular millifluidic system to deliver to a lab.

system can also process a CNB in a standalone mode, allowing an independent CNB fixation and storage protocols (Fig. 4.2 (c)). And the CNB after the PoC testing of the CoreView can be transported back to the modular system to be archived in a lab (Fig. 4.2 (d)). The CNB can be either kept in formalin for long-term storage, or in the preservative solution to maintain the optimized CNB preparation condition. Our modular system for CNB fixation monitoring will provide more flexibility to high-throughput PoC testing environment by fixing and preserving the CNB at appropriate time based on the clinical guidelines.

4.3 Optimizing formalin fixation of a CNB

Improper formalin fixation, under-fixation and over-fixation, is one of the well-known preanalytical errors causing a detrimental effect on histologic results [28,29]. Our all-optical millifluidic formalin monitoring system provides controlling of the formalin fixation time based on the optical transmittance change of a CNB. This ensures the optimally fixed CNB for further diagnostic imaging and testing, eliminating the errors from the various dimensions and tissue contents of CNBs in addition to under- and over-fixation. After the level of formalin fixation reaches to the desired point, the post-fixation processing varies by clinical setting and practices. In case of PoC diagnosis, the fixation monitoring system is integrated with the CoreView system, therefore, the fixed CNB can be transported via the millifluidic channels without any time delay. When the CoreView system meets the maximum capability of CNB testing or when the CNB is well fixed during shipment to a lab, formalin fixation is stopped by replacing formalin with other solutions which are used in staining or preserving steps. Another possible approach is to employ a thermoelectric cooling module to pause the formalin fixation by lowering formalin temperature to

or below 4 degC during the shipment provided that additional battery capacity and thermal insulation for the millifluidic chamber are applied.

4.4 MODULAR SHIPPING SYSTEM FOR OPTIMIZED FIXATION AND PRESERVATION OF A CNB

The CNB fixation monitoring system is designed to advance the PoC testing of the Coreview system. In addition to monitoring fixation level of a CNB, the modular portable platform of the CNB formalin fixation system also enables the secure shipping and storage for CNBs. Regardless of the novel PoC diagnosis of the CoreView system, archiving valuable human tissue biopsies is indispensable for other medical purposes, such as therapeutic research and treatment development. Therefore, we believe that this new CNB handling approach has great potential for use in various clinical settings. First, in the current histopathology lab environment, a consistent preanalytical tissue preparation will be available across different laboratories, where a lack of standardized protocols results in different ischemic time (time to fixation), time of sectioning and transfer to

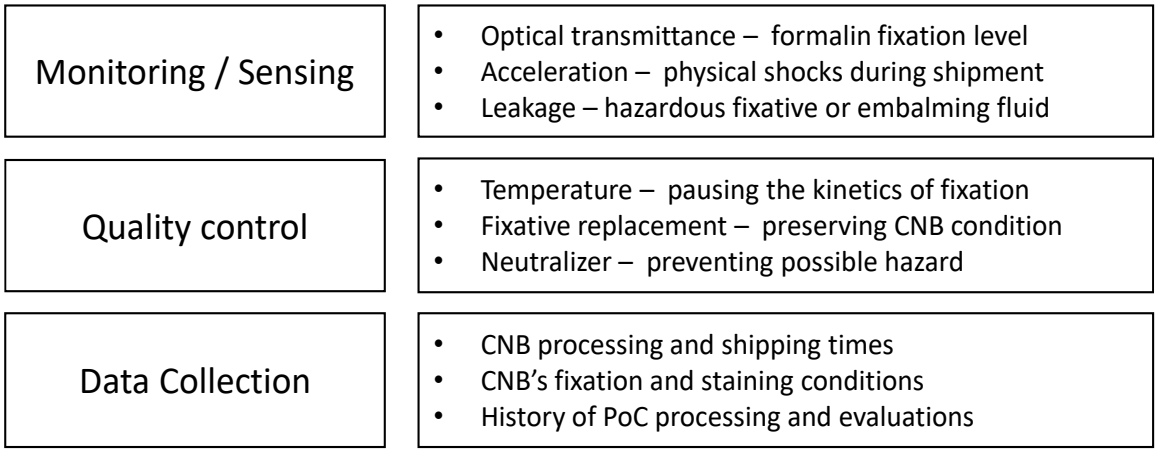

Fig. 4.3 Integrated features and functions of a CNB millifluidic shipping system

cassettes, and minimum and maximum fixation times [10,42]. Any human handling errors can also be reduced during the tissue processing and lab-to-lab transport. Second, for the up-and-coming rapid on-site evaluation, the CNB after PoC testing will be shipped to a lab in a safe and secure environment that ensures the optimized preanalytical processing of the CNB. The CNB will be properly fixed and preserved timely or will be maintained in desired solutions at a controlled temperature if necessary. The real-time processing history and time-track of the CNB will be recorded for a seamless translation into a clinical lab. Fig. 4.3 summarizes the forthcoming features for the CNB shipping system. Another promising application can be found in a mobile health clinic in rural setting. Whether or not our novel CoreView millifluidic system is outreached to the rural and remote areas, the CNB shipping system can deliver the pre- and post-processing CNBs in a well-controlled fashion that does not compromise the histopathological data necessary for disease diagnosis.

Our all-optical formalin fixation monitoring system consisting of minimal components can be fitted less than 15×15×15 cm^3, including the CNB collection kit, illumination measurement setup, and data processing and storage systems. A small battery power, e.g., a single 18650 battery, is expected to operate the system up to a week in a standalone mode, which suffice for shipping the CNB within a country. The major challenge will be any strong vibration or shock during shipping that may causes monitoring errors. Although more performance tests to simulate the potential risks will be required, the relative change analysis would be robust as the overall trend of change in optical transmittance is more significant than incidental short-term errors.

To properly process a CNB and preserve the sensitive biomarkers, such as immunohistochemical stains, is not a simple task even in a clinical lab environment. Our all-optical fixation monitoring system which can be shipped for days while recording the details of CNB processing and its

condition will be useful in high-throughput PoC diagnostics and will envision a new use of CNB making in-depth healthcare assessment more accessible in rural areas.

4.5 ACTIVE SYSTEMS FOR RAPID FORMALIN FIXATION

While monitoring formalin fixation can suggest the optimal fixation time for an individual CNB, the rate of formaldehyde crosslinking has not been modified. While formalin fixation provides superior morphologic preservation in a consistent and economical way, its standard process is time-consuming, which has been a significant obstacle in reducing the turnaround time to expedite clinical histopathologic results. Formalin fixation is accelerated at a higher temperature, where the equilibrium concentration of formaldehyde is increased in formalin, and the crosslinking reaction is expedited. However, the quality of histologic results suffers from erratic and inconsistent fixation by heated formalin. Alternative efforts aimed at speeding up formalin fixation have therefore been explored different methods to assist formalin fixation. Microwave-assisted formalin fixation [83,84], and ultrasound-accelerated formalin fixation [85,86] have been shown to significantly reduce the time of formalin fixation from 12-24 hours of the conventional method to less than an hour. And pressure-assisted formalin fixation [37] was also reported that the diffusion of formaldehyde was increased by 5-fold. One study suggested delaying heated formalin fixation [36] to eliminate the downside of rapid heated formalin fixation, which is nonuniform fixation between the inner and outer layers of a biopsy. However, those techniques are not broadly engaged in the histopathological protocol because of a lack of standardizing the preanalytical variables, such as the fixation time and temperature for each sample [87].

We expect our fixation monitoring millifluidic device to be combined with one or more rapid formalin fixation techniques. The millifluidic device with all-optical fixation monitoring can be created as a quantitative testbed to automatically process CNBs under different protocols and

controlled conditions. The optimization of preanalytical variables for rapid formalin fixation can be defined for the type of a CNB and the selections of target biomarkers. Because the standardization of tissue processing is not likely to be achieved in such a complex workflow, it can be expected that the customization of the tissue processing steps will be determined for individual CNB. And such integration of multiple tissue processing protocols cannot be feasible unless the physical property change (i.e., bulk optical transmittance) of a CNB is sensitively monitored. In addition, microwave and ultrasound methods can be used for the antigen retrieval protocol for IHC [88,89]. Although the tissue processing steps after formalin fixation is not our immediate focus in this dissertation, the new automated millifluidic system for CNB will take advantage of the supplemental feature from rapid formalin fixation techniques.

Chapter 5. PROOF OF CONCEPT OF A SURROGATE HIGH-ADHESION MEDICAL TAPE USING PHOTO-THERMAL RELEASE FOR RAPID AND LESS PAINFUL REMOVAL

5.1 ABSTRACT

Medical tapes often hold critical devices to the skin so having high adhesion for the lifespan of this product is of great importance. However, the removal process is challenging for caregivers and patients alike, often a painful process that can cause medical adhesive-related skin injury (MARSI). By using an industrial thermally-sensitive tape, a surrogate photosensitive tape was developed that switched from the equivalent of high-adhesion medical tape to low-adhesion medical tape. This resulted in an 86% reduction in the average peel strength when heated from 45 to 55 °C using a custom test apparatus. To photo-release the prototype tape, a near-infrared (NIR) absorbing layer was painted on a visibly clear thermal-sensitive tape and a NIR optical wand using 15-LEDs (940nm) with thermal feedback control was designed and tested. Preliminary performance of photo-to-thermal conversion was numerically modeled with transient results matching experimental measurements with 96.8% correspondence. Using the verified energy conversion model of the surrogate photosensitive tape, a new NIR optical wand was designed for rapid and non-contact release of a future medical tape at 10-degrees lower than the release temperature of the custom adhesive, which is called UnTape. Numerical simulations compared to the thermal skin pain threshold of 45°C predicts photo-release within 1.1-seconds of NIR exposure (85.5% absorption in prototype tape at < 1.3 W/cm2). The unique properties of the multifunctional UnTape system (tape and portable NIR wand) may allow even stronger skin adhesion for critical

medical devices while concurrently reducing the risk of MARSI upon photo release and easy removal.

5.2 INTRODUCTION

Medical adhesive tapes are a class of ubiquitous medical devices that consist of a plastic or fabric backing, coated on one side with an adhesive layer. According to the FDA Code of Federal Regulations Title 21 Section 880.5240 [90], “The device is used to cover and protect wounds, to hold together the skin edges of a wound, to support an injured part of the body, or to secure objects to the skin." Adhesion to the skin is the primary objective of these functions. However, a stronger and more stable adhesive bond to the skin requires a more laborious and often painful removal process, which can lead to anxiety for patient and caregiver [91] and medical adhesive-related skin injuries (MARSI) [92].

MARSI is defined as an occurrence of erythema or cutaneous abnormality (including blister, erosion, tear, etc.) that persists 30 minutes or more after adhesive removal [92]. The prevalence rates of MARSI vary significantly between studies for patient populations and the type and location of the medical adhesive. One study reported a total MARSI incidence of 29.83% at the peripherally inserted central catheter insertion sites of oncology patients [93]. Another study reported a MARSI incidence of 5.8% with 207 patient visits in an outpatient vascular clinic over three months [94]. MARSI is potentially underreported in many areas of care, as it is not considered an unexpected or adverse injury [95]. From one study in a pediatric intensive care unit, 76.3% of MARSI was caused by the securements of tracheal intubation, vascular access, and electrocardiogram monitor [96]. Because accidental dislocation of those critical medical devices can result in serious events, the problems resulting from limited choices in medical tape are

expected to be well beyond MARSI prevalence. Although the probability of MARSI is based on the combination of various risk factors, it is highest with neonatal patients [92], as neonatal skin is nearly 50% thinner than adult skin, and with geriatric patients [94] who often have compromised skin. In a study published in 2015, the daily MARSI prevalence ranged from 3.4% to 25.0% with a mean of 13.0% and a patient median age of 58 years [97]. In a pilot study with pediatric patients who required central venous access devices secured by clear medical tape, skin injuries were a substantial issue affecting 9% of patients and causing an additional 4% to withdraw due to skin irritation [98].

In the United States, nurses are aware of MARSI risk and take responsibility for choosing the type of medical tape needed for the patient given the specific task required [99]. To reduce the incidence of MARSI, 3M™ introduced a silicone-based adhesive tape for patients most at risk of MARSI. This was compared to standard acrylate-based plastic tape over a two-week period by over 200 nurses [100]. More than half of the nurses surveyed were dissatisfied with the current tapes when used on patients with fragile or at-risk-skin. Unlike the acrylate-based adhesives which have higher skin adhesion over time, the silicone-based adhesive remains consistent over time, but adherence may be unreliable with silicone products or critical tubing [92]. As such, low tack and low adhesion silicone adhesives that provide easy and rapid removal should not be used in the securement of central or peripheral venous catheters even for neonatal and geriatric patients. To obtain high initial tack and strong skin adhesion, chemical solvents are used to slowly remove the adhesive to avoid the increased risk of damaging the epidermal layer of the skin [91]. Tape selection based on the patient's condition and clinical need is crucial as current single adhesive products do not serve a wide range of situations. [99].

There is a need for high adhesion pressure sensitive tapes that can transition to a lower adhesion at the time of removal. Reported mechanisms to achieve this quick-release range from a multi-layer adhesive/antiadhesive transition layer [101], adhesives with thermally activated components that exhibit phase transitions [102–104], and light-sensitive components [105]. Temperature variation by light absorption (photothermal release) offers the opportunity for localized activation using moderate optical power sources. Light absorption additives applied to the backing or adhesive layer can enable the transfer of energy from the light source to the adhesive for temperature switching. The commercial availability of efficient near-infrared (NIR) light-emitting-diodes (LEDs) enables the design of an adhesive removal device with desirable features such as visible light transparency and chemical-free release. This novel approach to activating a thermally switched adhesive may lead to a clinically relevant system that allows painless skin release without the harmful MARSI side-effects.

We used a surrogate system to demonstrate the mechanism of rapid and gentle removal of a NIR photothermal sensitive tape (UnTape), and propose the future design of a medical tape system based on experiments and numerical analyses. The overall procedure of this study consists of following steps: (1) Experimental verification that an industrial thermal-release tape can be a medical tape surrogate based on a comparative study of the peel strengths of commercially available products, (2) Develop a prototype tape (*PT*) demonstrating the rapid and non-contact photothermal release by applying a NIR absorbing dye to the outer layer of the thermal-release tape, (3) Fabricate a NIR light source device with a temperature control feature, (4) Numerically model the adhesive thermal switching using a realistic skin substrate, (5) Compare the experimental and modeling results and establish a relationship of energy flow from the electrical

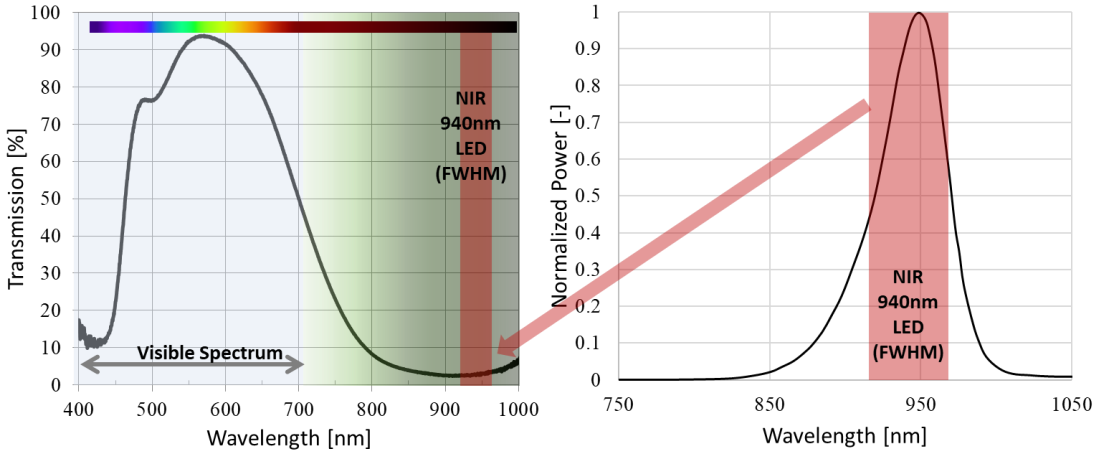

Fig. 5.1 (left) Transmission spectrum of a multi-layer NIR dye coating. The coating was applied to an *IT* and the transmission spectrum measurement was calibrated with a reference spectrum taken from a clear *IT*. (right) Spectral power emission of the Luxeon NIR LED [114]. The NIR dye coating shows significant transmission in the visible spectrum, while the NIR light, especially at the LED's peak wavelength of 940 nm (shade area), is 95% absorbed by the NIR dye coating. The transmission spectrum of the *IT* is not presented as it shows a typical transmission spectrum of a polyester (PET or Mylar) film, 90-95% in VIS-NIR region.

input to thermal heating of the *PT*, (6) Determine the design parameters for a future clinical UnTape system.

5.3 METHODS

5.3.1 Adhesion-switchable Medical Tape

The UnTape system consists of a photothermal sensitive tape (named UnTape) and a NIR light source (named NIR wand). For the proof-of-concept investigation of the UnTape system, we used the combination of two off-the-shelf products as a *PT*, (1) thermal-switchable tape with clear backing and (2) NIR-absorbing liquid coating. The commercial adhesive film, used in the

electronics industry, offers decreased adhesion when heated, which is marketed as Intelimer® Tape (*IT*), manufactured by Nitta Corporation under license from the Landec Corporation. The adhesion strength of *IT* is significantly reduced near the switch temperature (STemp) of 50°C. The maximum peel strength decreases from 90% (45°C) to 10% (55°C).

To increase the temperature of the *IT* using NIR light, we applied a NIR dye coating (LD920C, Clearweld®, Gentex Corporation) on the top surface of the *IT* backing. The NIR dye coating efficiently converts the NIR (940 - 1100 nm) optical power into thermal energy. Our measurements showed that a thick layer of the NIR dye coating (4 strokes of a dye applicator) could reduce the *IT* light transmission near 900 nm by more than 95%, while retaining transmission in the visible spectrum (Fig. 5.1), providing NIR dye coating transmittance results similar to those in related references [106,107]. Light transmission in the visible region (400 - 700 nm) is a necessary feature of medical tape used to secure intravenous devices to allow for monitoring of proper fluid delivery. The absorption of the NIR light depends on the amount of dye material deposited on the *IT* backing surface. However, the low viscosity, acetone-based NIR dye coating solution uses a marker pen type dispenser which hindered the deposition of a uniform coating with a consistent thickness. To combat this, a single batch of PT was fabricated with two strokes of the dye applicator, providing a more uniform dye layer. This was used for experimental testing, which reduced the *PT* transmission near 900 nm to 46%.

One study reported that the temperature threshold of heat-induced pain for human skin is approximately 45°C based on a study with 106 people who were tested on the radial side of the palm and the top of foot [108]. The skin's pain sensation and thermal damage depends on the contact temperature and the duration of exposure [109]. When the contact temperature was 45°C,

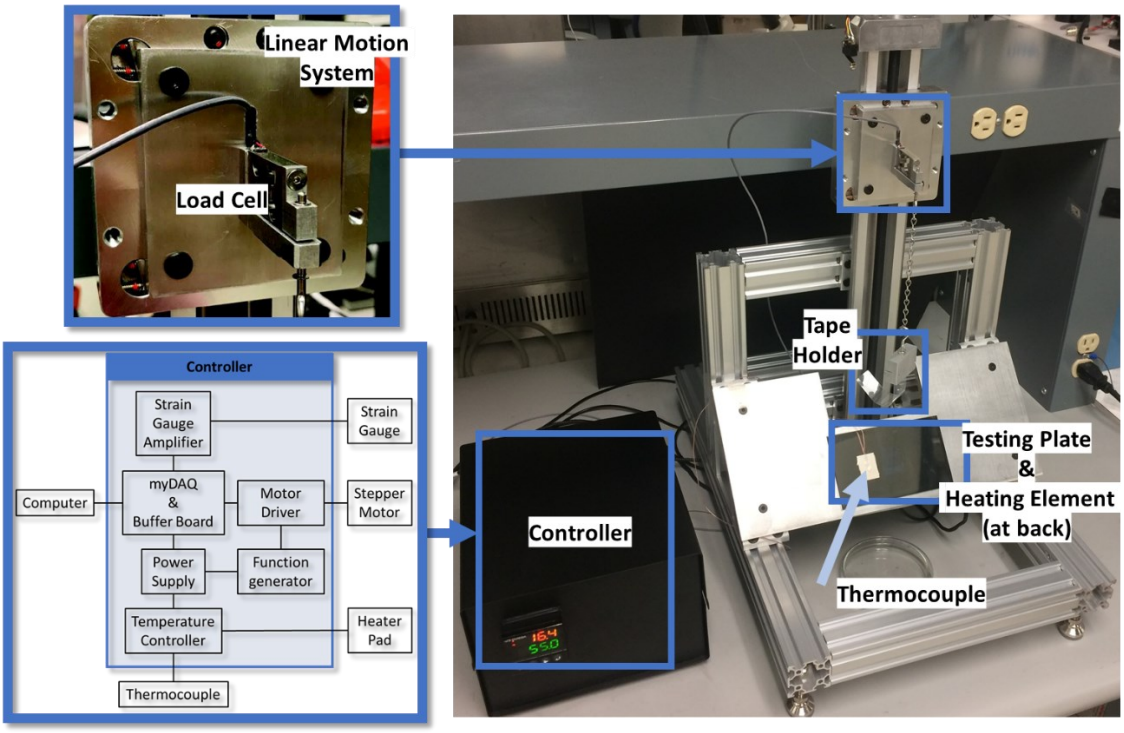

Fig. 5.2 Peel strength test apparatus with the controller box. The apparatus has an aluminum structure that contains a linear motion system, a load cell, a heating and temperature sensing platform, and a clamp for holding the tape. The stainless testing plate was at the 135° peeling position.

the results showed that it took more than 30 minutes to induce skin injury [110,111], indicating that the threshold temperature of skin pain at 45°C for a NIR exposure time of less than 10 seconds is a conservative estimate for our analyses. However, due to the lack of a commercial source of a lower STemp adhesive tape, the higher STemp Nitta *IT* with NIR dye coating on its backing was used as the *PT* throughout the preliminary *in vitro* testing.

5.3.2 Peel Strength Measurement

To assess the peel strength of the *PT* in comparison to other medical pressure-adhesive tapes, we constructed a peel strength test apparatus with a temperature-controlled plate, shown in Fig. 5.2.

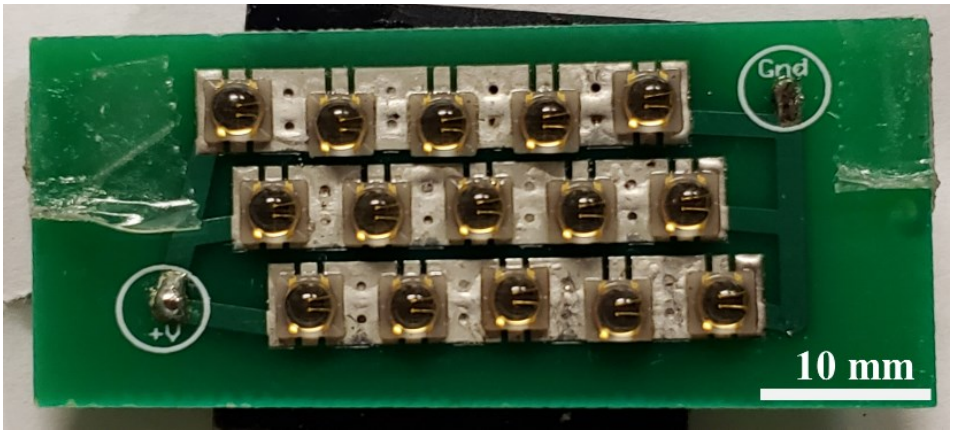

Fig. 5.3 NIR 15-LED array board. Each is capable of emitting 1450mW radiometric power at a nominal current of 1.0 A with a forward voltage of 2.9V. The LED array has three 5-LED rows in parallel which are positioned 5.5mm apart and offset 2 mm with another row. The average optical power (measured with Newport 1830-C and Newport 818-IR, Newport, Irvine, CA) at 20 mm is approximately 1.4806 W/cm^2.

Table 5.1. Thermal properties of skin [113], acrylic, and 304 stainless steel

	Skin (Epidermis+dermis)	Acrylic	304 Stainless steel
Thermal conductivity, k [W/(m·K)]	0.343	0.190	160
Density, ρ [kg/m^3]	1200	1200	7800
Specific heat, C_p [kJ/(kg·K]]	3.44	1.47	0.480
Thermal inertia, I [kJ/(m^2·K·s$^{1/2}$)]	37.6	18.1	244.8

The apparatus was designed based on Test Method F of ASTM D 3330/D 3330M [112]. The peel strength test apparatus was framed with aluminum extrusion components and the main components are a linear motion system, a load cell, a heating and temperature sensing platform, and a clamp for holding the tape. The bright annealed 304 stainless steel testing plate is horizontally located under the tape holder, setting an adjustable peeling angle of 90-135°. The testing has a controllable heating system on the backside. A proportional–integral–derivative (PID) controller and solid-

state relay were used to modulate power to the thin film heater. A thermocouple (SA1 Type T, Omega, Inc.) was affixed to the testing plate alongside the tape to monitor the temperature of the adhesion surface.

To measure the peel strength, a tape sample is attached on the testing plate with one end of the tape clamped with the tape holder. The peeling speed is set to 50 mm/min for the peeling distance of 18 mm.

5.3.3 NIR Light Source

The NIR dye coating converts optical energy to heat energy leading to reduced adhesion of the *PT*. Thus, the adhesive heating mechanism depends on the optical power of the NIR light source, which is a function of the radiometric power, beam angle, and illumination area. To avoid overheating the substrate, the light source needs to sense and monitor the temperature of the *PT* in real-time. While using the NIR wand on the *PT*, the temperature is monitored, and when it hits the target temperature (i.e., 55°C) the user is alerted to initiate the peeling process in order to avoid excess heat application. 15 NIR (940nm) LEDs (Lumileds L1I0-0940060000000) were used in the prototype NIR light source (shown in Fig. 5.3), and an infrared (IR) thermometer (MLX90614, Melexis) was used to monitor the target surface temperature. An Arduino Nano platform was used to manage the custom-made LED driver, *IR* thermometer, and PID controller. The LED optical power was modulated by the PID controller to maintain the target temperature as sensed by the *IR* sensor with minimal latency. The prototype NIR light source was later packaged with a 3D printed case.

5.3.4 Heat Transfer Experiments and Finite Element Simulation

Acrylic Substrate as a Test Model

The UnTape photothermal heating mechanism by NIR light exposure was evaluated using an acrylic substrate as a test model for heat transfer analysis. The averaged thermal properties of skin [113], acrylic (Polymethlymethacrylate, PMMA), and 304 stainless steel are listed in Table 5.1. Because of the lower conductivity and specific heat of acrylic, the thermal inertia ($I = \sqrt{k\rho c_p}$) of acrylic is approximately one half of the averaged skin thermal inertia. The standard for testing adhesive tapes uses 304 stainless steel as the substrate which has a thermal inertia 3X higher than skin. This significantly higher thermal inertia of stainless steel prevents temperature increases on the illumination surface. Thus, the 6mm thick acrylic substrate was used for NIR heating experiments since it has comparable thermal conductivity to skin and also has well characterized thermal properties that work well with finite element analysis. In addition, the low thermal inertia of acrylic adds additional safety factors in future human skin experiments, because the sensible temperature at the skin surface is expected to be lower than at the acrylic surface.

NIR Heating Experiments

To examine the performance of the NIR LED arrays and proposed operating specifications, experimental temperature measurements were conducted with the acrylic substrate and *PT*. For each LED, a constant-current driver supplied three different input currents of 500.0, 666.7, and 833.3 mA, and the corresponding forward voltages of 2.67, 2.78, and 2.83 V, respectively. The threshold temperature in the PID controller was set to 55°C, which is the release temperature (RTemp) of the *PT*. When the temperature reading reached the threshold, the pulse width

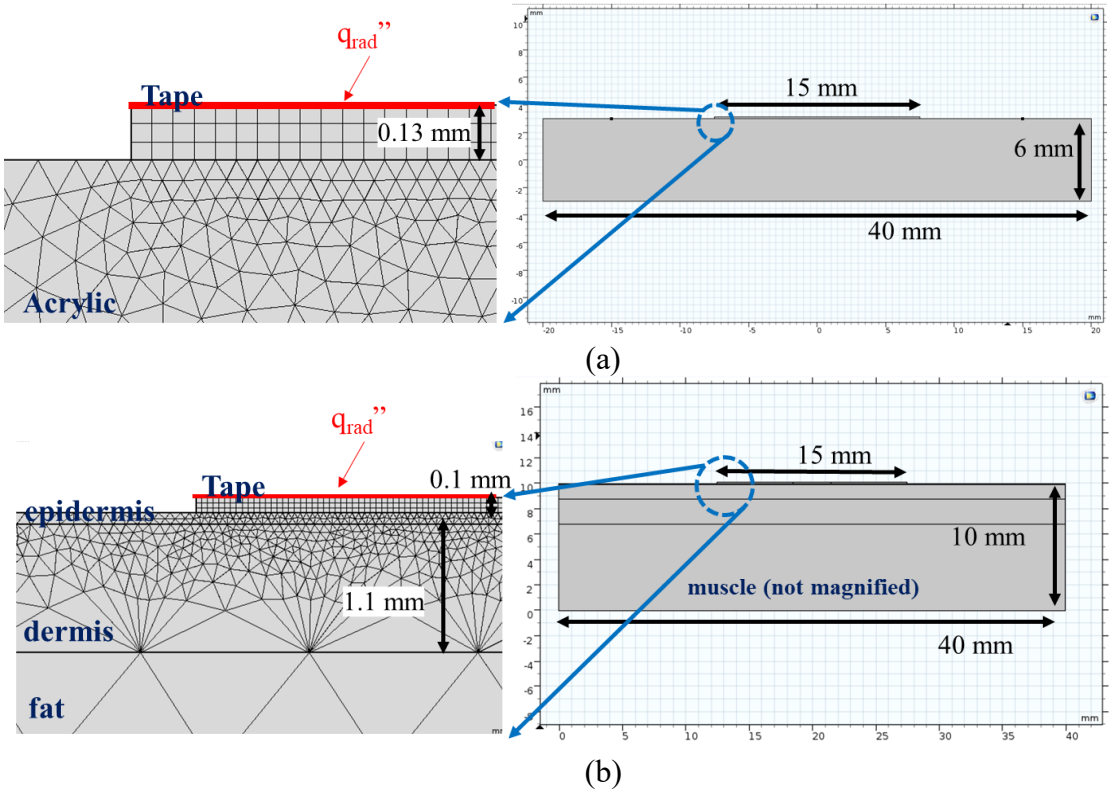

Fig. 5.4 Geometry and local meshing grid of (a) *PT* - acrylic model and (b) UnTape - skin model. The upper surface of the tapes receives the heat flux. Both tapes are modeled as a single material (PET) for simplicity; thus, an adhesive layer and a NIR dye coating layer were not included. The properties of the layers are presented in Table 5.2.

modulation output from the microcontroller modulated the light intensity to maintain a constant temperature at this threshold value.

COMSOL Simulations

The numerical modeling was performed to establish the correlation of energy conversion between the experimental measurements and the simulation. After the correlation is established, the future photothermal sensitive tape with a lower adhesion STemp of 40°C and a higher NIR absorption can be designed based on the numerical model.

Table 5.2. Thermophysical properties of the components in the COMSOL models: PET, Acrylic, Epidermis, Dermis, Fat, and Muscle (human skin properties are from Okabe et al., [113]).

			PET	Acrylic	Epidermis	Dermis	Fat	Muscle
Thickness	d	mm	0.13	6	0.1	1.1	2	6.8
Thermal conductivity	k	W/(m·K)	0.155	0.19	0.235	0.445	0.185	0.51
Density	rho	kg/m^3	1390	1200	1200	1200	1085	1030
Heat capacity	Cp	kJ/(kg·K)	1.17	1.47	3.59	3.30	2.67	3.80

The finite element method simulations using COMSOL Multiphysics® Version 5.4 platform was conducted to analyze the NIR heating experimental results and to adjust the performance of the NIR LED board and control system for human skin. Fig. 5.4 (a) shows the geometry and mesh of the *PT* and acrylic substrate model. The thermophysical properties of the materials are included in Table 5.2. A 2D time dependent study for was performed for 5 seconds for the parameter sweep of q_{rad}, the radiative heat flux on the surface of the *PT*, between 0.3 and 1.0 W/cm^2. This heat flux was equivalent to the net NIR exposure converted to heat energy after subtracting the reflection and transmittance of NIR from the *PT*. Meshing consists of a linearly mapped mesh for the *PT* domain and a triangular mesh for the acrylic domain. All surfaces were set to a diffusive surface to adjust to the room temperature, 22°C.

5.4 RESULTS

5.4.1 Peel Strength Measurement Using Acrylic Substrate

Fig. 5.5 shows the peel strength force comparison between the *IT* and other medical tapes on the market. 3M™ Durapore™ surgical tape and 3M™ Kind removal silicon tape were chosen to represent the highest and lowest adhesive forces among common medical pressure-adhesive tapes.

Using the peel strength test apparatus, five measurements at the 90˚ peeling angle were collected for each tape sample attached on the acrylic substrate and were averaged to evaluate the required peel forces per unit width. The comparison clearly shows that the selected commercial surrogate thermal-sensitive *IT* has an adhesion strength equivalent to the 3M™ Durapore™ high-tack tape at 45°C. After the temperature increases to 55°C, the adhesion force drops by 86% ($\text{Percentage of drop} = \frac{(0.1429-0.0198)}{0.1429} \times 100 = 86.14\%$), which is comparable to the low adhesive strength of the 3M™ Kind tape.

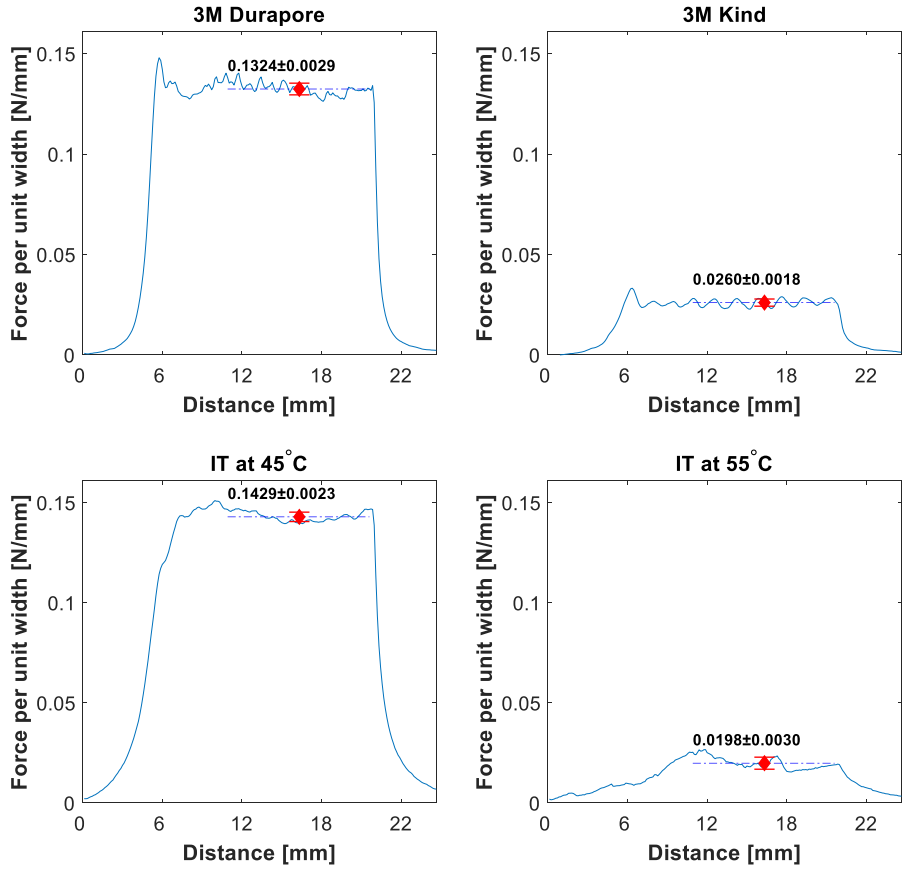

Fig. 5.5 Peel strength comparison: 3M™ Durapore, 3M™ Kind, and *IT* at 45°C and 55°C. The *IT* has a STemp at 50°C and shows the adhesion force drop by an average of 86% between 45°C and 55°C. The adhesion force of the *IT* at 45°C is stronger than 3M™ Durapore but also becomes as low as 3M™ Kind at 55°C. The bars and marks represent the average and standard deviation of the peel strength between 12 and 20 mm in the peeling distance.

5.4.2 NIR Heating Experiments with an Acrylic Substrate

Fig. 5.6 shows the temperature profiles of the *PT* during the NIR light irradiation. The elapsed times for the threshold temperature, 55˚C, at each forward current are shown. The input currents at 1500, 2000, 2500 mA were applied to three 5-LED rows so that each LED was operated at 500, 666.7, and 833.3 mA, respectively. The heating profile and operating conditions at 2000 mA were exploited to estimate the effective optical power of the NIR light source in conjunction with MATLAB and COMSOL simulations.

The emissivity compensation for the *IR* temperature measurement was not predetermined because of the design flexibility for various surface measurement. Therefore, the emissivity compensation based on the reference emissivity (ε = 0.94) of polyethylene terephthalate (PET) and the room temperature ($T_{ambient}$= 22˚C) was followed. The corrected temperature of 56.79˚C was obtained by the following Eq. (1),

$$T_{target} = \sqrt[4]{\frac{{T_{sensor}}^4 - (1-\varepsilon)\cdot {T_{ambient}}^4}{\varepsilon}} \quad (1)$$

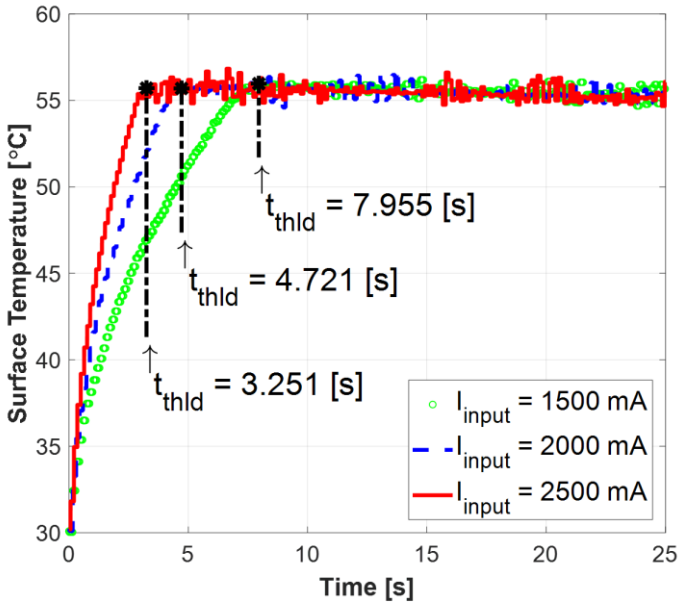

Fig. 5.6 Transient temperature changes of the *PT* by NIR exposure. Various currents (1500, 2000, and 2500 mA) were applied to the LED array, and the higher input lead to the shorter times to reach the threshold temperature. The time to threshold temperature was marked with black stars. After that point, the surface temperatures were maintained by the PID controller. Because the power supply of the prototype NIR wand was set to the current of 2A, the experimental data fitting with the COMSOL simulation shown in Fig. 5.7 was based on the NIR heating time of 4.72 seconds at 2A.

5.4.3 Comparison of NIR Optical Power Intensities

From the COMSOL simulation model, the temperature profiles of the *PT* with various heat fluxes are plotted in Fig. 5.7. As we have the experimental results of the threshold temperature of the *PT* surface and the time to reach the threshold temperature, those values are overlaid in the figure: the black-dotted line represents the threshold temperature measured from the experiments and the red-dotted line represents the elapsed time to reach the threshold temperature. The data point of 0.6442 W/cm^2 in the simulation was interpolated as the best-fit heat flux based on the experimental results.

The heat flux applied to the COMSOL model did not include optical power conversion parameters, such as the reflectance and transmittance of the *PT*. Therefore, the estimated heat flux is the net light energy absorbed by the *PT* backing.

From the LED specification data [114], the optical intensity of the LED arrays, I, can be estimated as follows,

$$I_{\text{est}} = \frac{n \cdot \Phi_{LED,1A} \cdot \eta_{F.A.} \cdot \eta_{area} \cdot \eta_{temp} \cdot (1-\gamma-\tau)}{A_{illumination}} \quad (2)$$

where n is the number of LEDs, $\Phi_{LED,1A}$ is the nominal radiometric power at the input current of 1.0 A, $\eta_{F.A.}$ is the proportionality of radiant power at a different input current, η_{area} is the radiant power ratio for the effective illumination area, η_{temp} is the output variation by the LED case temperature, γ is the surface reflectance, τ is the object transmittance, and $A_{illumination}$ is the area of illumination. From the specification data, the $\Phi_{LED,1A}$ is 1450 mW, and $\eta_{F.A.}$ is linearly proportional to input current (e.g., $\eta_{F.A.}$ = 0.8 if the input current is 0.8 A). At the illumination distance of 20 mm between the LED board and the *PT*, η_{area} was approximately 0.536 for the window size is 31mm × 16mm. The reflectance, γ, and transmittance, τ, at 940nm were directly measured from the *IT* and *PT*, respectively, using the optical power meter (Newport 1830-C and 818-IR): γ = 10.5 % and τ = 46.0 % based on the *PT* that was coated twice with the Clearweld NIR dye. We assume that the reflectance of the *PT* and the *IT* are the same, so the net absorption of the *PT* coating layer, α , can be estimated as follows: $\alpha = (1 - \gamma - \tau) = 0.435$. As predefined in the prototype NIR wand design, $A_{illumination}$ and the window are considered the same size.

The net NIR optical intensity delivered by the NIR LED array was measured by the optical power meter (Newport 1830-C and 818-IR) independently from the numerical simulation and the specification calculation.

The COMSOL results were based on the heat energy released on the surface of the *PT* backing, which assumes that the net NIR optical power was absorbed only by the NIR dye coating. On the other hand, the NIR LED optical power measurement (using the optical power meter) corresponds to the raw radiant flux before hitting the *PT*. Therefore, in order to juxtapose the optical power measurement (using the optical power meter) with the values from NIR LED optical power calculation (using the LED specification data) and COMSOL results, the measurement from the optical power meter was further corrected by the absorption of the *PT*.

$$I_{\text{exp}} = I_{\text{measured}} \cdot \alpha = I_{\text{measured}} \cdot (1 - \gamma - \tau) \qquad (3)$$

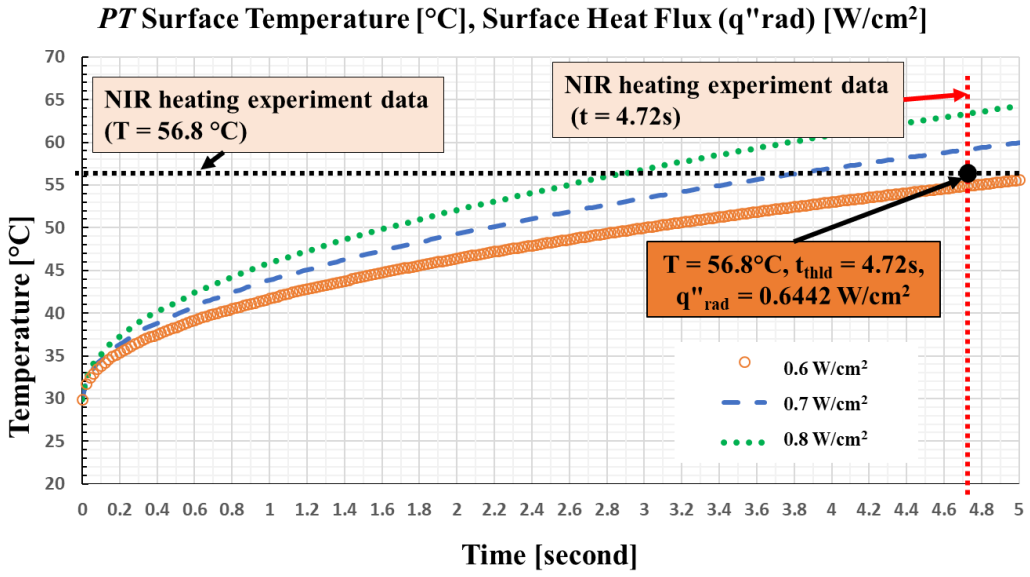

Fig. 5.7 COMSOL result from the tape-acrylic model in Fig. 5.4 (a). Time-dependent temperature increase by the surface heat flux at 0.6, 0.7, and 0.8 W/cm^2 are plotted. The threshold temperature and the elapsed time of NIR heating from the NIR heating experiment is overlaid; a round dot is the crossing point between the horizontal dotted line (the threshold temperature at 56.8˚C) and the vertical dotted line (the elapsed time to reach the threshold temperature). The heat flux of 0.6442 W/cm^2 at the crossing point was interpolated from the COMSOL temperature profiles.

Table 5.3. Comparison of the heat or NIR radiant fluxes required to increase the temperature of the *PT* up to 55˚C. I_{est} was estimated from the LED specification data, I_{COMSOL} was evaluated from the COMSOL of a *PT*-acrylic model fitting the NIR heating experiment, I_{exp} was measured using the optical power meter and converted to the optical intensity. I_{est} and I_{exp} were calibrated by the NIR dye absorption of the *PT* in order to compare NIR intensity and heat flux absorbed at the NIR dye layer. The error is calculated based on the optical power measurement.

Method	Estimation from LED specification	NIR testing with COMSOL simulation	Optical power measurement
	I_{est}	I_{COMSOL}	I_{exp}
q''_{net} [W/cm^2]	0.6821	0.6442	0.6651
Error [%]	+2.5	-3.2	N/A

Thus, the I_{COMSOL}, from the numerical simulations, can be compared with the I_{est}, the estimated optical power based on the LED specification sheet, and I_{exp}, from the optical meter experiments. Table 5.3 shows the comparison of the results from three independent calculations and measurements, which were all based on the experimental conditions of a 2A input current, 4.72 second illumination time, and the 20mm distance between the LED board and the *PT*. The radiant flux from the optical power meter measurement can be considered as the actual NIR optical power from the LEDs. All three optical power intensities are within the error range of less than 5%.

5.4.4 Skin Model Simulation

At this stage of development, the *PT* and NIR lighting source are not ready for human testing. However, we estimated the required thermal heat flux to reach the RTemp at 55˚C from the NIR light source device based on the simulation and NIR *PT in vitro* measurements. Thus, the estimated heat flux can be used as a NIR heating simulation for human skin based on the current NIR light

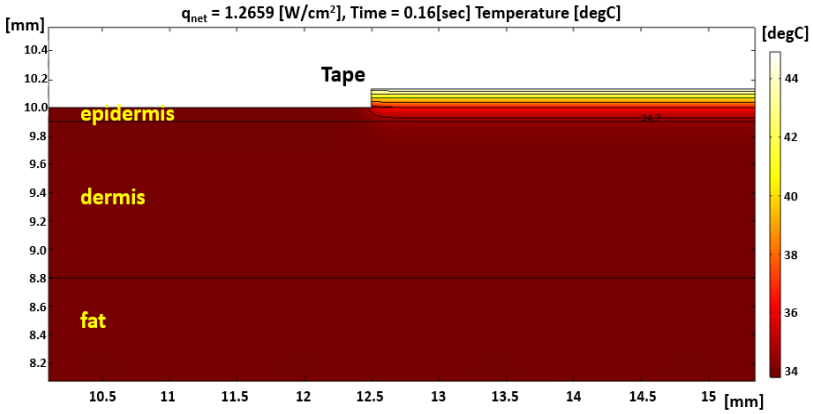

(a)

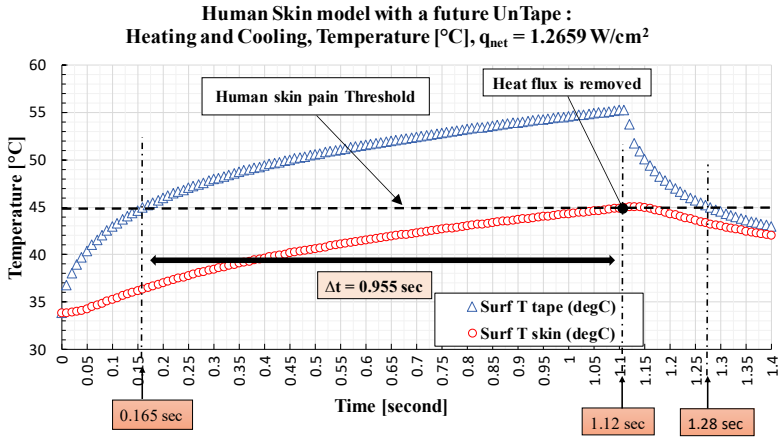

(b)

Fig. 5.8 Simulation result of a skin - UnTape model (RTemp at 45˚C and NIR absorption of 0.855). Due to the high NIR absorption of the UnTape, the effective heat flux is 1.2659 W/cm^2 estimated from the NIR radiant power of the prototype NIR wand and the NIR absorption. (a) Temperature distribution of human skin model at t=0.16s. Epidermis, dermis, and fat layers with different properties from top to bottom (the skin properties are presented in Table 5.2). (b) Temperature profiles on the surface of the UnTape and the interface between the UnTape and the skin surfaces. The pain threshold temperature of human skin (horizontal dotted line at 45˚C), and the heating times for the tape surface and skin surface to reach 45˚C are presented; 0.165s and

1.12s (vertical dotted lines). Cooling profiles are also shown after the heating is stopped at the human skin pain threshold, t=1.12s.

Table 5.4. Simulation settings and the results of the human skin – UnTape model

RTemp [˚C]	45˚C
NIR absorption of a tape	0.855
Incident NIR optical intensity [W/cm^2]	1.4806
Effective Heat flux input [W/cm^2] (absorbed by the tape)	1.2659
Elapsed time for RTemp at tape surface [sec]	0.165
Elapsed time for RTemp at skin surface [sec]	1.12

source design. The transient heating effect on the skin model to RTemp at 45˚C was considered and the effective heat flux by NIR absorption was set to 1.2659 W/cm^2. Fig. 5.8 and Table 5.4 summarize the setting parameters and results of the human skin model simulation. As the UnTape has a higher NIR absorption than that of the *PT*, the elapsed time to reach 45˚C at the outer surface was an estimated 0.165 seconds and 1.12 seconds for the UnTape tape and skin, respectively. If heating continues to the human skin pain threshold (45˚C), the UnTape surface temperature reaches 55˚C and cooling occurs relatively quickly (< 0.2 second). This significant temperature difference (10˚C) across the small thickness of the tape (130 μm) will be reduced in future UnTape designs, in which the NIR absorbing dye is embedded in the backing, an intermediate layer, or the adhesive layer.

5.5 DISCUSSION

This study investigated the feasibility of a photothermal mechanism for rapid and gentle removal of high-tack adhesive tape and yielded thermal properties for future UnTape development. Commercially available NIR absorbing dye was coated on the outer surface of a commercially

available thermal-sensitive tape. Our tests demonstrated that using the absorbed optical energy supplied by the NIR LEDs (Fig. 5.3), the tape adhesion force dropped an average of 86% at the RTemp (55°C). This has demonstrated that the NIR light source can efficiently increase the tape's bulk and surface temperature to ease removal. Additionally, the industrial thermal-release film tape (*IT*) successfully acted as a surrogate for comparing medical tape adhesion levels. The peel strength test showed that the *PT* can have stronger adhesion than high-tack surgical tape (3M™ Durapore) while exhibiting release properties at the RTemp equivalent to extra gentle silicone-base medical tape (3M™ Kind). Retaining the *PT* visible light transparency ensures that the medical staff can view the skin beneath the dressing, allowing the applicator to accurately attach the taped device to the skin and to observe any skin damage or irritation.

In this study, an adhesion RTemp of 55˚C is considered higher than the 45˚C [108] threshold of human skin pain level. The application of the NIR absorbing dye solution on the backing of the *IT* was done without professional coating techniques, which produced a nonuniform coating layer, possibly leading to irregular NIR absorbing on the *PT* surface area. Despite this variation, the preliminary measurements with the engineered prototype tape and light source device provided valuable insight for the design of a future UnTape system. This system will consist of a flashlight-like NIR light source and NIR sensitized medical tape that efficiently switches adhesion at 40˚C, allowing for the future UnTape to achieve full release at 45 ˚C.

5.5.1 Experimental-Theoretical Correlation

We investigated the prototype NIR light source optical power intensity and heat flux required to heat the *PT* to RTemp (55˚C), as shown in Table 5.3. Based on the optical power measurement, the estimated NIR optical power intensities from the LED specification data and the numerical simulation were in agreement to within 5%. The NIR energy conversion can be attributed to

multiple factors including NIR reflection, transmission, and NIR dye coating absorption. Additionally, other operating conditions in NIR LEDs, such as case temperature and power stability, may cause the variations in calculations. Furthermore, every experimental factor cannot be precisely controlled, estimated, or measured due to the nature of our prototype fabrication and the dependence of these parameters upon the NIR dye absorption.

Detailed information of the model (tape backing and adhesive layer) may improve the COMSOL models. These simulations were based on reference material properties and simple modeling assumptions. For example, the adhesive layer was defined as part of the tape backing, eliminating the thermal resistance within the adhesive interface among skin, adhesive, trapped air, and tape backing. The *IR* temperature meter measured the temperature of the surface of the tape and the emissivity compensation for the temperature calibration was based on the bulk emissivity of PET, which is 0.94. However, a recent study showed the emissivity of a PET film is as low as 0.8 [115]. Therefore, proper *IR* wavelength of a thermometer sensor and the thickness and surface condition of the tape backing will be important design factors for future UnTape designs to avoid temperature measurement errors.

The NIR dye absorption depended significantly on the amount of dye coating. The twice coated *PT* was used to provide consistent NIR dye coating, but the high NIR transmittance of the *PT*, 46%, was not desirable. Adding more layers of the NIR dye coating only slightly increases absorbance above 95%, with diminishing returns due to surface reflection, as shown in

Fig. 5.1. Although we need more information about the photo-thermal transduction mechanism, including multiple reflections in a multi-layer NIR dye coating structure with various illumination angles on different skin conditions and pigmentation, for this analysis we will assume that the dye

layer absorbs 95% of the NIR incident illumination around 940 nm without significant reduction of visible light transparency.

5.5.2 Skin Model Discussion

We investigated the temperature change on a human skin model based on the heat flux value and fitting data from the experiments and simulations using the acrylic substrate. Using the NIR light source, it took only 1.12 seconds to heat UnTape to the human skin pain threshold. The one second NIR exposure for medical tape removal is a promising result for the future UnTape system, which will have an optimized tape design and NIR illumination approach. However, the rapid heating near the skin will require strict temperature control that may extend the heating time to reduce the risk of overheating.

When pursuing future product design, we will investigate how and where the target temperature of the tape will be measured and how deep the NIR absorbing layer will be embedded in the tape. Additionally, this skin model may need adjustments, such as the thickness of epidermis/dermis for neonate or geriatric patients.

The environmental temperature is also an important variable as it affects tape adhesion. At this stage, we are assuming a controlled environment in hospitals or caregiving facilities. Additional experiments and simulations are needed to understand the stability of the product during transportation and storage at extreme temperatures. Regardless, once applied, the tape temperature is regulated by body temperatures, as the heat conduction rate is significantly higher than the convection rate.

5.5.3 Future UnTape System Product Design

UnTape aims to create a new medical tape that provides strong adhesion and rapid and gentle removal upon application of NIR by a portable NIR light device in order to avoid MARSI. We believe that the UnTape project will not only limit MARSI, pain, lifelong scars, and potential emotional stress [96], but also will improve the quality of care when adhering critical devices to the skin. Although our system adds cost with the addition of NIR light absorbing dye and the LED NIR wand, limiting MARSI cases and reducing clinical workloads will save the healthcare system

Table 5.5. Power consumption calculation. General operating parameters, LED driving conditions, NIR optical power, and possible battery-powered plan are presented.

Operating Parameters		
Illumination Area	25.4 × 5	w×h [mm×mm]
# Of LED in Wand	4	[each]
Release Temperature	45	[°C]
Example Tape Size	25.4×50	w×h [mm×mm]
Time for Single Tape Removal	5	[sec]
LED Driving Parameters		
Rated Current	1.3	[A]
Rated Voltage	2.8	[V]
Required Electrical Power	3.640	[W]
Estimated Optical Power	1.885	[W]
NIR Illumination		
Required Optical Power	1.880	[W]
Required Optical Intensity	1.481	[W/cm^2]
Single 18650 Battery		
Rated Capacity	2500	[mAh]
Continuous Running Time	115.4	[minute]
Tape Removal Cycle	1384	[cycle]
Double 18650 Batteries		
Rated Capacity	5000	[mAh]
Continuous Running Time	230.8	[minute]
Tape Removal Cycle	2769	[cycle]

significant capital [95]. Based on the *PT* experiments and numerical analyses for NIR heating, we propose the future UnTape product design, described below.

Photothermal Sensitive Tape, UnTape

The new photothermal sensitive tape, named UnTape, will have a lower adhesive STemp and RTemp, and a higher NIR light absorption, leading to improved heat conversion. The NIR absorbing dye will be uniformly distributed in the UnTape adhesion layer. The tape will not exceed the human skin pain threshold. The temperature dependence of the adhesive will allow for higher adhesion forces without the difficult removal process. The adhesive layer can be designed in different ways based on the target patients. For example, retention of a peripheral intravenous catheter on the skin provides stabilization and avoids risk of infection [116]. As UnTape can have high adhesion, it can be highly perforated for other medical functions. A highly perforated tape

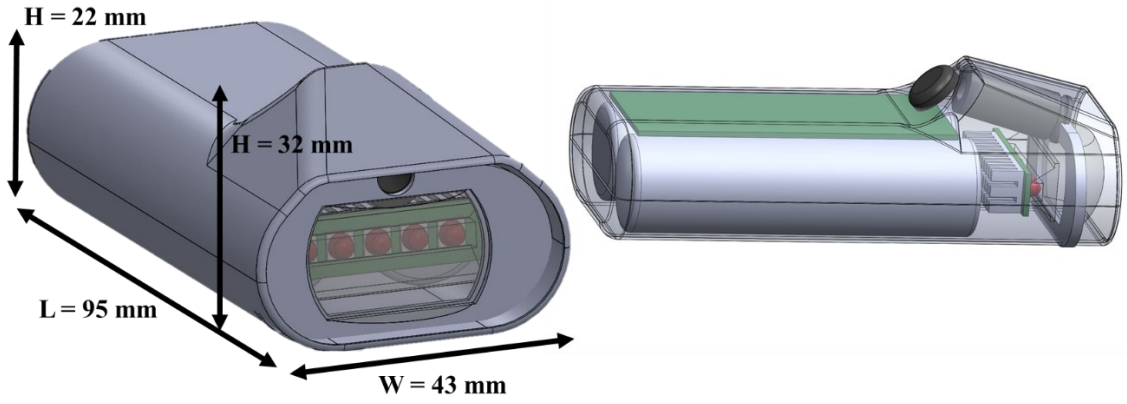

Fig. 5.9 3D rendering of a future NIR wand using a line of NIR LEDs with the central one being a visible targeting beam. Above the LEDs creating a narrow area of NIR illumination is an angled window to a thermal sensor. The device is powered by two batteries for expected multiday use without recharging. The dimension of the device is also presented.

with a hydrophobic backing layer may allow for breathability, elasticity, and water resistance. Perforated UnTape will disperse the heat over the skin surface, minimizing the risk of skin pain.

NIR Wand

Power consumption is an important consideration for the NIR light source design. Due to the inefficient conversion process from electrical energy to heat energy, the input power for the wand was often as high as 30W. In addition, energy was lost due to unfocused NIR illumination and the limited window size of the wand. An improved NIR wand design is based on the optical intensity value estimated from the NIR LED specification data, which is a conservative approach because of the highest power requirement (See Table 5.3).

The same NIR LED specification was considered and all other calculations were also adapted with these potential improvements. The new illumination approach is 'hand scanning'. A user holds the NIR wand by hand and manually sweeps over UnTape. A 18mm × 65mm rechargeable lithium-ion battery was considered as a power source. This 3000 mAh battery has a nominal voltage of 3.6V and an end-of-discharge voltage of 2.8V. This design suffices to show the proper intensity of NIR illumination in a battery powered system without any further improvements on the NIR absorbing dye coating or the industrial tape backing.

Table 5.5 presents the power consumption based on the experimental results and numerical simulations. One or two 18650 batteries were considered, and continuous running times of >30 minutes and >60 are expected, respectively. The battery capacity was conservatively applied at the end-of-discharge voltage. Therefore, incorporating a voltage regulator will operate the LEDs more efficiently. In addition to the current *IR* thermometer sensor, the improved NIR wand will have a red guiding light located between the two NIR LEDs so that the lens-focused NIR illumination beams can be visualized. The power consumption of the *IR* thermometer and guiding LED are less

than 30mA, and the sizes are small enough to be embedded in the LED board. The feedback signal for the temperature alert can be included. Color change on a LED indicator, an alarm, or a tactile signal can tell the user when the temperature has been reached.

Fig. 5.9 shows the 3D rendering of the double-battery powered model of the future NIR wand using a single row of 4 NIR LEDs with a central red LED. The visible red LED will illuminate the target so the operator can easily see the NIR exposure area. A diffuser and reflector will uniformly focus the illumination from the 4 NIR LEDs.

5.5.4 Skin Safety

Based on the previous *in vitro* and *in vivo* studies, the perception of skin pain in adult occurs at skin temperatures above 43°C, and thermal damage occurs when the temperature of the basal layer (the innermost layer of epidermis) reaches 44°C [109]. The dependence of skin pain and injury on the temperature and duration of exposure is commonly accepted. Durations of exposure to induce reversible thermal skin damage have been reported as 45 minutes at 46.5°C, 60 minutes at 46°C [117], and 60 minutes at 44°C [110].

According to the ASTM guide C1055-99 [118], epidermis damage (first degree burns, reversible with no permanent damage) occurs approximately 44˚C after 6 hours of thermal contact, and the exposure time to skin damage is reduced by 50% for each 1˚C increase, up to around 51˚C. The guideline also included the recommendation of a 1-min exposure limit for infants, elderly, or infirmed, who have slow reaction times. An independent study by Diller [111] presents a specific suggestion for the maximum delivery temperature of domestic tap water, of which a safety standard was based on adult skin thickness. Diller found that the skin thickness ratio between a child and adult is 0.72, and showed the skin injury induced by 10 seconds of exposure to hot water at 48.9˚C corresponds to the same exposure at 46.7˚C with a child. Exposure to hot water may

result in a worse burn injury than the NIR exposure, in which is relatively small area is covered. Thus, safety guidelines and *in vitro*/*vivo* studies imply that the UnTape removal process, which increases the temperature of the adhesive to 45˚C for 1-5 seconds in the local skin area, would not result in any skin burn. Human testing could not be done with the prototype system which has a higher adhesion STemp at 55˚C. We expect human subject testing can occur once the lower STemp tape is developed and experimentally measured *in vitro*.

5.6 CONCLUSION

A prototype photothermal tape release system was demonstrated using NIR LEDs and temperature switching high-tack adhesive tape coated with an NIR absorbing dye. This combination of an optical energy source coupled to a matched light absorption coating provided a test bed for forecasting the feasibility of developing a clinically useful system that will lower the incidence of medical adhesive related skin injuries. Reasonable agreement between the experimentally measured results and a numerical model provides a sound foundation for the design of a next generation UnTape system.

Chapter 6. SUMMARY AND PUBLICATIONS

Fig. 6.1 summarizes the research aims presented in this dissertation. The flowchart represents the typical engineering design processes. The research aims are separately overlaid based on the research achievements.

Project 1, that is to design and develop the opto-mechanical formalin fixation monitoring systems, consists of three aims: two preliminary studies and two main studies. Two preliminary studies (Aim 1a and Aim 1b) were to evaluate the feasibility of the millifluidic CNB transport and the

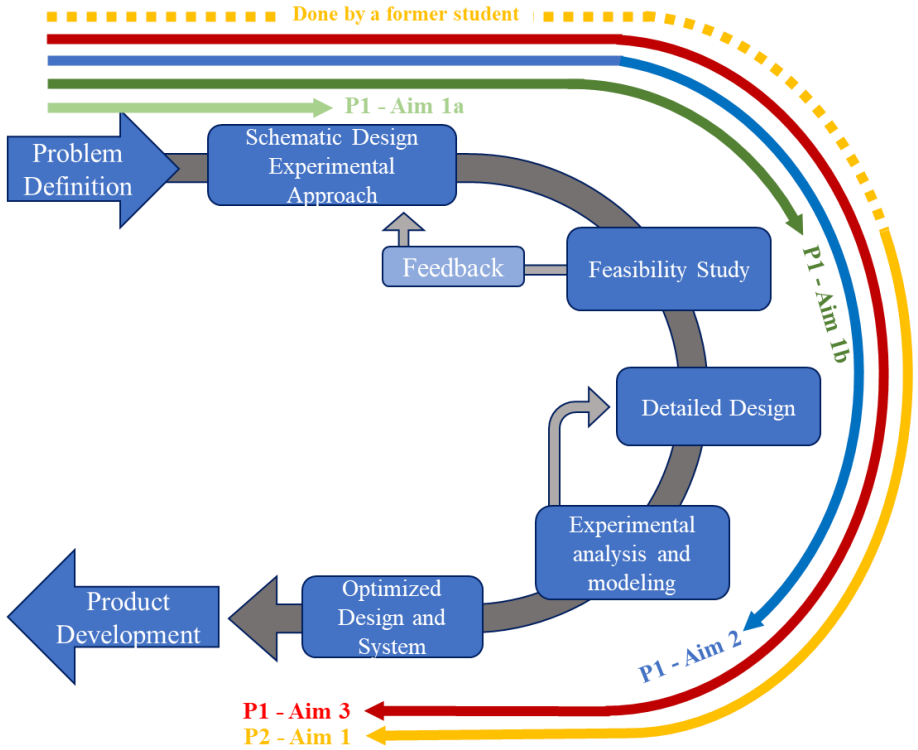

Fig. 6.1 Overview of dissertation research. P1: Project 1 – Design and development of formalin fixation monitoring systems for CNB, P2: Project 2 – Product design of a novel photo-sensitive medical tape (UnTape)

CNB stiffness measurement in millifluidic channels, respectively. Under guidance of two postdoctoral researchers, the foundation of the main research topics was established. Chapter 1.3.2 briefly describes those research works of which more details are available in the proceedings papers [12,14]. The first main study of Project 1 (P1 – Aim2) was to design, build, and test the SW elastography system for the formalin fixation level of a submerged biopsy in a millifluidic chamber. This topic presented in Chapter 2 was published in Journal of Translational Engineering in Health and Medicine (JTEHM) [18]. The second main study of Project 1 (P1 – Aim3) was to design, test, and prototype the formalin monitoring system that measures the optical transmittance of a CNB. In Chapter 3, the design and development of the all-optical fixation monitoring system are presented, and the manuscript is prepared for submission to the JTEHM. Chapter 4 envisions the potential development and applications of a novel millifluidic device that could open a new era of rapid point-of-care testing with a CNB.

Project 2 (P2 – Aim1) was to establish the product design framework for a novel photo-sensitive medical tape and its removal system to reduce the risk of MARSI. Chapter 5 presents the analysis of a proof-of-concept system and the engineering design suggestion for the product-level development. The research work was published in ASME Journal of Medical Devices [119], and the suggested product design is currently under fabrication and testing by a new Ph.D students in our lab.

BIBLIOGRAPHY

[1] Silverstein, M. J., Recht, A., Lagios, M. D., Bleiweiss, I. J., Blumencranz, P. W., Gizienski, T., Harms, S. E., Harness, J., Jackman, R. J., Klimberg, V. S., Kuske, R., Levine, G. M., Linver, M. N., Rafferty, E. A., Rugo, H., Schilling, K., Tripathy, D., Whitworth, P. W., and Willey, S. C., 2009, "Image-Detected Breast Cancer: State-of-the-Art Diagnosis and Treatment," J. Am. Coll. Surg., **209**(4), pp. 504–520.

[2] Loeb, S., Carter, H. B., Berndt, S. I., Ricker, W., and Schaeffer, E. M., 2011, "Complications after Prostate Biopsy: Data from SEER-Medicare," J. Urol., **186**(5), pp. 1830–1834.

[3] Dean, D. S., and Gharib, H., 2000, *Fine-Needle Aspiration Biopsy of the Thyroid Gland. [Updated 2015 Apr 26]*, MDText.com, Inc., South Dartmouth (MA).

[4] Finn, W. G., 2007, "Diagnostic Pathology and Laboratory Medicine in the Age of 'Omics': A Paper Fron the 2006 William Beaumont Hospital Symposium on Molecular Pathology," J. Mol. Diagnostics, **9**(4), pp. 431–436.

[5] Calhoun, K. E., and Anderson, B. O., 2014, "Needle Biopsy for Breast Cancer Diagnosis: A Quality Metric for Breast Surgical Practice," J. Clin. Oncol., **32**(21), pp. 2191–2192.

[6] McGhee, J. D., and von Hippel, P. H., 1977, "Formaldehyde as a Probe of DNA Structure. 4. Mechanism of the Initial Reaction of Formaldehyde with DNA," Biochemistry, **16**(15), pp. 3276–3293.

[7] Thavarajah, R., Mudimbaimannar, V., Rao, U., Ranganathan, K., Elizabeth, J., Thippeswamy, R., Mudimbaimannar, V., Elizabeth, J., Rao, U., and Ranqanathan, K., 2012, "Chemical and Physical Basics of Routine Formaldehyde Fixation," J. Oral Maxillofac. Pathol., **16**(3), pp. 400–405.

[8] Werner, M., Chott, A., Fabiano, A., and Battifora, H., 2000, "Effect of Formalin Tissue Fixation and Processing on Immunohistochemistry," Am. J. Surg. Pathol., **24**(7), pp. 1016–1019.

[9] Hewitt, S. M., Lewis, F. A., Cao, Y., Conrad, R. C., Cronin, M., Danenberg, K. D., Goralski, T. J., Langmore, J. P., Raja, R. G., Williams, P. M., Palma, J. F., and Warrington, J. A., 2008, "Tissue Handling and Specimen Preparation in Surgical Pathology," Arch. Pathol., **132**(December).

[10] Yaziji, H., Taylor, C. R., Goldstein, N. S., Dabbs, D. J., Hammond, E. H., Hewlett, B., Floyd, A. D., Barry, T. S., Martin, A. W., Badve, S., Baehner, F., Cartun, R. W., Eisen, R. N., Swanson, P. E., Hewitt, S. M., Vyberg, M., and Hicks, D. G., 2008, "Consensus Recommendations on Estrogen Receptor Testing in Breast Cancer by Immunohistochemistry.," Appl. Immunohistochem. Mol. Morphol., **16**(6), pp. 513–520.

[11] Das, R., Burfeind, C. W., Kramer, G. M., and Seibel, E. J., 2014, "Pathology in a Tube: Step 1. Fixing, Staining, and Transporting Pancreatic Core Biopsies in a Microfluidic Device for 3D Imaging," *Proc. SPIE 8976, Microfluidics, BioMEMS, and Medical Microsystems XII*, p. 89760R.

[12] Das, R., Burfeind, C. W., Lim, S. D., Patle, S., and Seibel, E. J., 2018, "Pathology in a Tub Step 2: Simple, Rapid Fabrication of Curved, Circular Cross Section Millifluidic Channels for Biopsy Preparation/3D Imaging towards Pancreatic Cancer Detection and Diagnosis," *Microfluidics, BioMEMS, and Medical Microsystems XVI*, p. 43.

[13] Das, R., Murphy, R. G., and Seibel, E. J., 2015, "Beyond Isolated Cells: Microfluidic Transport of Large Tissue for Pancreatic Cancer Diagnosis," **9320**, p. 93200N.

[14] Das, R., Nguyen, T. T.-M., Lim, S. D., O'Donnell, M., Wang, R. K. R. K., and Seibel, E. J. E. J., 2014, "Feasibility of a Hybrid Elastographic-Microfluidic Device to Rapidly Process and Assess Pancreatic Cancer Biopsies for Pathologists," *Health Innovations and Point-of-Care Technologies Conference*, Seattle, WA, pp. 271–275.

[15] Bussolati, G., Annaratone, L., Medico, E., D'Armento, G., and Sapino, A., 2011, "Formalin Fixation at Low Temperature Better Preserves Nucleic Acid Integrity," PLoS One, **6**(6).

[16] Qin, X. J., and Ling, B. X., 2012, "Proteomic Studies in Breast Cancer (Review)," Oncol. Lett., **3**(4), pp. 735–743.

[17] Hughes, C. S., Mcconechy, M. K., Cochrane, D. R., Nazeran, T., Karnezis, A. N., Huntsman, D. G., and Morin, G. B., 2016, "Quantitative Profiling of Single Formalin Fixed Tumour Sections: Proteomics for Translational Research," Sci. Rep., **6**(September), pp. 1–14.

[18] Lim, S. D., Huang, Q., and Seibel, E. J., 2019, "Evaluation of Formalin Fixation for Tissue Biopsies Using Shear Wave Laser Speckle Imaging System," IEEE J. Transl. Eng. Heal. Med., **7**(March).

[19] Cooper, D. J., Fauver, M. E., Dintzis, S. M., and Seibel, E. J., 2020, "Rapid Needle Biopsy Assessment at Point of Care to Advance Personalized Cancer Therapy," *AACR ANNUAL MEETING*.

[20] Fox, C. H., Johnson, F. B., Whiting, J., and Roller, P. P., 1985, "Formaldehyde Fixation.," J. Histochem. Cytochem., **33**(8), pp. 845–853.

[21] Boon, M. E., Gerrits, P. O., Moorlag, H. E., Nieuwenhuis, P., and Kok, L. P., 1988, "Formaldehyde Fixation and Microwave Irradiation.," Histochem. J., **20**(6–7), pp. 313–322.

[22] Wolff, A. C., Hammond, M. E. H., Allison, K. H., Harvey, B. E., Mangu, P. B., Bartlett, J. M. S., Bilous, M., Ellis, I. O., Fitzgibbons, P., Hanna, W., Jenkins, R. B., Press, M. F., Spears, P. A., Gail, H., Viale, G., Mcshane, L. M., and Dowsett, M., 2018, "Human Epidermal Growth Factor Receptor 2 Testing in Breast Cancer: American Society of Clinical Oncology/College of American Pathologists Clinical Practice Guideline Focused Update," Arch Pathol Lab Med.

[23] Sathyanarayana, U. G., Birch, C., Nagle, R. B., Tomlins, S. A., Palanisamy, N., Zhang, W., Hubbard, A., Brunhoeber, P., Wang, Y., and Tang, L., 2015, "Determination of Optimum Formalin Fixation Duration for Prostate Needle Biopsies for Immunohistochemistry and Quantum Dot FISH Analysis.," Appl. Immunohistochem. Mol. Morphol., **23**(5), pp. 364–373.

[24] Ibarra, J. a., and Rogers, L. W., 2010, "Fixation Time Does Not Affect Expression of HER2/Neu: A Pilot Study," Am. J. Clin. Pathol., **134**(4), pp. 594–596.

[25] Sujoy, V., Nadji, M., and Morales, A. R., 2014, "Brief Formalin Fixation and Rapid Tissue Processing Do Not Affect the Sensitivity of ER Immunohistochemistry of Breast Core Biopsies," Am. J. Clin. Pathol., **141**(4), pp. 522–526.

[26] Halilovic, A., Bulte, J., Jacobs, Y., Braam, H., van Cleef, P., Schlooz-Vries, M., Werner, A., Boelens, O., Nagtegaal, I., de Wilt, H., and Bult, P., 2017, "Brief Fixation Enables Same-Day Breast Cancer Diagnosis with Reliable Assessment of Hormone Receptors, E-Cadherin and HER2/Neu," J. Clin. Pathol., p. jclinpath-2017-204362.

[27] Gown, A. M., 2009, "Tweaking and Nudging toward Improved-IHC Quality," Appl. Immunohistochem. Mol. Morphol., **17**(5), pp. 363–365.

[28] Goldstein, N. S., Ferkowicz, M., Odish, E., Mani, A., and Hastah, F., 2003, "Minimum

Formalin Fixation Time for Consistent Estrogen Receptor Immunohistochemical Staining of Invasive Breast Carcinoma," Am. J. Clin. Pathol., **120**(1), pp. 86–92.

[29] Yaziji, H., and Barry, T., 2006, "Diagnostic Immunohistochemistry: What Can Go Wrong?," Adv. Anat. Pathol., **13**(5), pp. 238–246.

[30] Webster, J. D., Miller, M. a, Dusold, D., and Ramos-Vara, J., 2009, "Effects of Prolonged Formalin Fixation on Diagnostic Immunohistochemistry in Domestic Animals.," J. Histochem. Cytochem., **57**(8), pp. 753–761.

[31] Agrawal, L., Engel, K. B., Greytak, S. R., and Moore, H. M., 2017, "Understanding Preanalytical Variables and Their Effects on Clinical Biomarkers of Oncology and Immunotherapy," Semin. Cancer Biol., (December).

[32] Susman, S., Berindan-Neagoe, I., Petrushev, B., Pirlog, R., Florian, I. S., Mihu, C. M., Berce, C., Craciun, L., Grewal, R., and Tomuleasa, C., 2018, "The Role of the Pathology Department in the Preanalytical Phase of Molecular Analyses," Cancer Manag. Res., **10**, pp. 745–753.

[33] Farkona, S., Diamandis, E. P., and Blasutig, I. M., 2016, "Cancer Immunotherapy: The Beginning of the End of Cancer?," BMC Med., **14**(1), pp. 1–18.

[34] Lindfors, K. K., and Rosenquist, C. J., 1994, "Needle Core Biopsy Guided with Mammography: A Study of Cost- Effectiveness," Radiology, **190**(1), pp. 217–222.

[35] Ganott, M. A., Zuley, M. L., Abrams, G. S., Lu, A. H., Kelly, A. E., Sumkin, J. H., Chivukula, M., Carter, G., Austin, R. M., and Bandos, A. I., 2014, "Ultrasound Guided Core Biopsy versus Fine Needle Aspiration for Evaluation of Axillary Lymphadenopathy in Patients with Breast Cancer.," ISRN Oncol., **2014**, p. 703160.

[36] Chafin, D., Theiss, A., Roberts, E., Borlee, G., Otter, M., and Baird, G. S., 2013, "Rapid Two-Temperature Formalin Fixation.," PLoS One, **8**(1), p. e54138.

[37] Chesnick, I. E., Mason, J. T., Leary, T. J. O., and Fowler, C. B., 2010, "Elevated Pressure Improves the Rate of Formalin Penetration While Preserving Tissue Morphology," pp. 178–183.

[38] Zou, N., Liang, Q., He, H., Liu, J., Ji, A., Nelson, a M., and Chu, W. S., 2011, "Ultrasound-Facilitated Formalin Fixation of Biological Specimens.," Biotech. Histochem., **86**(6), pp. 413–20.

[39] Bulte, J. P., Polman, L., Schlooz-Vries, M., Werner, A., Besselink, R., Sessink, K., Mus,

R., Lardenoije, S., Imhof-Tas, M., Bulten, J., Van Engen-Van Grunsven, A. C. H., Schaafsma, E., Strobbe, L. J. A., Bult, P., and De Wilt, J. H. W., 2013, "One-Day Core Needle Biopsy in a Breast Clinic: 4 Years Experience," Breast Cancer Res. Treat., **137**(2), pp. 609–616.

[40] Moelans, C. B., Oostenrijk, D., Moons, M. J., and Van Diest, P. J., 2011, "Formaldehyde Substitute Fixatives: Effects on Nucleic Acid Preservation," J. Clin. Pathol., **64**(11), pp. 960–967.

[41] Boissiere-Michot, F., Denouel, A., Boulle, N., Guillaume, C., Orsetti, B., Lopez-Crapez, E., Chateau, M.-C., and Bibeau, F., 2013, "The Non-Crosslinking Fixative RCL2(R)-CS100 Is Compatible with Both Pathology Diagnosis and Molecular Analyses.," Pathol. Oncol. Res., **19**(1), pp. 41–53.

[42] Chung, J. Y., Song, J. S., Ylaya, K., Sears, J. D., Choi, L., Cho, H., Rosenberg, A. Z., and Hewitt, S. M., 2018, "Histomorphological and Molecular Assessments of the Fixation Times Comparing Formalin and Ethanol-Based Fixatives," J. Histochem. Cytochem., **66**(2), pp. 121–135.

[43] Perry, C., Chung, J. Y., Ylaya, K., Choi, C. H., Simpson, A., Matsumoto, K. T., Smith, W. A., and Hewitt, S. M., 2016, "A Buffered Alcohol-Based Fixative for Histomorphologic and Molecular Applications," J. Histochem. Cytochem., **64**(7), pp. 425–440.

[44] Seibel, E. J., Miao, Q., Coe, R. L., and Reinhall, P. G., 2014, "Optical Projection Tomography Microscopy(OPTM) for Large Specimen Sizes."

[45] Bauer, D. R., Stevens, B., Chafin, D., Theiss, A. P., and Otter, M., 2016, "Active Monitoring of Formaldehyde Diffusion into Histological Tissues with Digital Acoustic Interferometry," J. Med. Imaging, **3**(1), p. 017002.

[46] Sarvazyan, A. P., Urban, M. W., and Greenleaf, J. F., 2013, "Acoustic Waves in Medical Imaging and Diagnostics," Ultrasound Med. Biol., **39**(7), pp. 1133–1146.

[47] Daoudi, K., Boccara, A. C., and Bossy, E., 2009, "Detection and Discrimination of Optical Absorption and Shear Stiffness at Depth in Tissue-Mimicking Phantoms by Transient Optoelastography," Appl. Phys. Lett., **94**(15), pp. 3–7.

[48] Elson, D. S., Li, R., Dunsby, C., Eckersley, R., and Tang, M.-X., 2011, "Ultrasound-Mediated Optical Tomography: A Review of Current Methods," Interface Focus, **1**(4), pp. 632–648.

[49] Chao, P., and Li, P., 2015, “Three-Dimensional Shear Wave Imaging Based on Full-Field Optical-Sectioned Laser Speckle Contrast Imaging,” pp. 3–5.

[50] Hall, T. J., Bilgen, M., Insana, M. F., and Krouskop, T. A., 1997, “Phantom Materials for Elastography,” IEEE Trans. Ultrason. Ferroelectr. Freq. Control, **44**(6), pp. 1355–1365.

[51] Kirkpatrick, S. J., Duncan, D. D., and Wells-Gray, E. M., 2008, “Detrimental Effects of Speckle-Pixel Size Matching in Laser Speckle Contrast Imaging,” Opt. Lett., **33**(24), p. 2886.

[52] Riccio, M., Breglio, G., Irace, A., and Spirito, P., 2007, “An Equivalent Time Temperature Mapping System with a 320×256pixels Full-Frame 100kHz Sampling Rate,” Rev. Sci. Instrum., **78**(10), p. 106106.

[53] Amador Carrascal, C., Chen, S., Manduca, A., Greenleaf, J. F., and Urban, M. W., 2017, “Improved Shear Wave Group Velocity Estimation Method Based on Spatiotemporal Peak and Thresholding Motion Search,” IEEE Trans. Ultrason. Ferroelectr. Freq. Control, **64**(4), pp. 660–668.

[54] Cheng, Y., Li, S., Eckersley, R. J., Elson, D. S., and Tang, M. X., 2015, “Detecting Tissue Optical and Mechanical Properties with an Ultrasound Modulated Optical Imaging System in Reflection Detection Geometry,” Biomed. Opt. Express, **6**(1), pp. 63–71.

[55] Chao, P.-Y., and Li, P.-C., 2016, “Three-Dimensional Shear Wave Imaging Based on Full-Field Laser Speckle Contrast Imaging with One-Dimensional Mechanical Scanning,” Opt. Express, **24**(17), p. 18860.

[56] Orescanin, M., and Insana, M., 2010, “Shear Modulus Estimation with Vibrating Needle Stimulation,” IEEE Trans. Ultrason. Ferroelectr. Freq. Control, **57**(6), pp. 1358–1367.

[57] Manapuram, R. K., Aglyamov, S., Menodiado, F. M., Mashiatulla, M., Wang, S., Baranov, S. A., Li, J., Emelianov, S., and Larin, K. V., 2012, “Estimation of Shear Wave Velocity in Gelatin Phantoms Utilizing PhS-SSOCT,” Laser Phys., **22**(9), pp. 1439–1444.

[58] Ling, Y., Li, C., Feng, K., Duncan, R., Eisma, R., Huang, Z., and Nabi, G., 2016, “Effects of Fixation and Preservation on Tissue Elastic Properties Measured by Quantitative Optical Coherence Elastography (OCE),” J. Biomech., **49**(7), pp. 1009–1015.

[59] Srinivasan, M., and Sedmak, D., 2002, “Effect of Fixatives and Tissue Processing on the Content and Integrity of Nucleic Acids,” Am. J. Pathol., **161**(6), pp. 1961–1971.

[60] Kennedy, B. F., Wijesinghe, P., and Sampson, D. D., 2017, “The Emergence of Optical

Elastography in Biomedicine," Nat. Photonics, **11**(4), pp. 215–221.

[61] Ambroziński, Ł., Song, S., Yoon, S. J., Pelivanov, I., Li, D., Gao, L., Shen, T. T., Wang, R. K., and O'Donnell, M., 2016, "Acoustic Micro-Tapping for Non-Contact 4D Imaging of Tissue Elasticity," Sci. Rep., **6**(December), p. 38967.

[62] Anand, S., Cicchi, R., Martelli, F., Giordano, F., Buccoliero, A. M., Guerrini, R., and Pavone, F. S., 2015, "Effects of Formalin Fixation on Tissue Optical Properties of In-Vitro Brain Samples," p. 93210Z.

[63] Zhang, H., Salo, D., Kim, D. M., Komarov, S., Tai, Y.-C., and Berezin, M. Y., 2016, "Penetration Depth of Photons in Biological Tissues from Hyperspectral Imaging in Shortwave Infrared in Transmission and Reflection Geometries," J. Biomed. Opt., **21**(12), p. 126006.

[64] Ash, C., Dubec, M., Donne, K., and Bashford, T., 2017, "Effect of Wavelength and Beam Width on Penetration in Light-Tissue Interaction Using Computational Methods," Lasers Med. Sci., **32**(8), pp. 1909–1918.

[65] Lerch, M. L., Bauer, D. R., Chafin, D., Theiss, A., Otter, M., and Baird, G. S., 2016, "Precision Medicine Starts With Preanalytics : Real-Time Assessment of Tissue Fixation Quality by Ultrasound Time-of-Flight Analysis," Appl Immunohistochem Mol Morphol, **00**(00), pp. 1–8.

[66] Cates, J. M. M., and Troutman, K. A., 2015, "Quality Management of the Immunohistochemistry Laboratory: A Practical Guide," Appl. Immunohistochem. Mol. Morphol., **23**(7), pp. 471–480.

[67] Dietel, M., Bubendorf, L., Dingemans, A.-M. C., Dooms, C., Elmberger, G., García, R. C., Kerr, K. M., Lim, E., López-Ríos, F., Thunnissen, E., Van Schil, P. E., and von Laffert, M., 2016, "Diagnostic Procedures for Non-Small-Cell Lung Cancer (NSCLC): Recommendations of the European Expert Group," Thorax, **71**(2), pp. 177–184.

[68] Shabihkhani, M., Lucey, G. M., Wei, B., Mareninov, S., Lou, J. J., Vinters, H. V., Singer, E. J., Cloughesy, T. F., and Yong, W. H., 2014, "The Procurement, Storage, and Quality Assurance of Frozen Blood and Tissue Biospecimens in Pathology, Biorepository, and Biobank Settings," Clin. Biochem., **47**(4–5), pp. 258–266.

[69] 2020, "Current CAP Guidelines," Coll. Am. Pathol. [Online]. Available: https://www.cap.org/protocols-and-guidelines/current-cap-guidelines.

[70] Sato, M., Kojima, M., Nagatsuma, A. K., Nakamura, Y., Saito, N., and Ochiai, A., 2014, "Optimal Fixation for Total Preanalytic Phase Evaluation in Pathology Laboratories. A Comprehensive Study Including Immunohistochemistry, DNA, and MRNA Assays," Pathol. Int., **64**(5), pp. 209–216.

[71] Leong, A. S. Y., and Leong, T. Y. M., 2011, "Standardization in Immunohistology.," *Formalin-Fixed Paraffin-Embedded Tissues*, Humana Press, pp. 37–68.

[72] Bauer, D. R., Stevens, B., Taft, J., Chafin, D., Petre, V., Theiss, A. P., and Otter, M., 2014, "Dynamic Subnanosecond Time-of-Flight Detection for Ultra-Precise Diffusion Monitoring and Optimization of Biomarker Preservation," J.G. Bosch, and M.M. Doyley, eds., p. 90400B.

[73] Guan, G., Li, C., Ling, Y., Yang, Y., Vorstius, J. B., Keatch, R. P., Wang, R. K., and Huang, Z., 2013, "Quantitative Evaluation of Degenerated Tendon Model Using Combined Optical Coherence Elastography and Acoustic Radiation Force Method," J Biomed Opt, **18**(11), p. 111417.

[74] Sarvazyan, A. P. A., Rudenko, O. O. V, Swanson, S. D., Fowlkes, J. B., and Emelianov, S. Y., 1998, "Shear Wave Elasticity Imaging: A New Ultrasonic Technology of Medical Diagnostics," Ultrasound Med. Biol., **24**(9), pp. 1419–1435.

[75] Hsiung, P.-L., Nambiar, P. R., and Fujimoto, J. G., 2005, "Effect of Tissue Preservation on Imaging Using Ultrahigh Resolution Optical Coherence Tomography," J. Biomed. Opt., **10**(6), p. 064033.

[76] Wood, M. F. G., Vurgun, N., Wallenburg, M. a, and Vitkin, I. a, 2011, "Effects of Formalin Fixation on Tissue Optical Polarization Properties.," Phys. Med. Biol., **56**(8), pp. N115–N122.

[77] Pitzschke, A., Lovisa, B., Seydoux, O., Haenggi, M., Oertel, M. F., Zellweger, M., Tardy, Y., and Wagnières, G., 2015, "Optical Properties of Rabbit Brain in the Red and Near-Infrared: Changes Observed under *in Vivo* , Postmortem, Frozen, and Formalin-Fixated Conditions," J. Biomed. Opt., **20**(2), p. 025006.

[78] Layton, C., Bancroft, J. D., Suvana, S. K., and Wolfe, D., 2019, *Fixation of Tissues*, Elsevier Health Sciences.

[79] Dapson, R. W., 2007, "Macromolecular Changes Caused by Formalin Fixation and Antigen Retrieval," Biotech. Histochem., **82**(3), pp. 133–140.

[80] Helander, K. G., 1994, “Kinetic Studies of Formaldehyde Binding in Tissue,” Biotech. Histochem., **69**(3), pp. 177–9.

[81] Palmer, K. F., and Williams, D., 1974, “OPTICAL PROPERTIES OF WATER IN THE NEAR INFRARED.,” J Opt Soc Am, **64**(8), pp. 1107–1110.

[82] Querry, M. R., Cary, P. G., and Waring, R. C., 1978, “Split-Pulse Laser Method for Measuring Attenuation Coefficients of Transparent Liquids: Application to Deionized Filtered Water in the Visible Region,” Appl. Opt., **17**(22), p. 3587.

[83] Giberson, R. T. ., and Elliott, D. E., 2005, “Rapid Microwave-Assisted Fixation of Fresh Tissue.”

[84] Giberson, R. T. . D. E. E., 2001, “Microwave-Assisted Formalin Fixation of Fresh Tissue,” *Microwave Techniques and Protocols*, Humana Press, pp. 191–208.

[85] Chu, W.-S., 2010, “Ultrasound-Mediated High-Speed Biological Reaction and Tissue Processing.”

[86] Chu, W.-S., Furusato, B., Wong, K., Sesterhenn, I. a, Mostofi, F. K., Wei, M. Q., Zhu, Z., Abbondanzo, S. L., and Liang, Q., 2005, “Ultrasound-Accelerated Formalin Fixation of Tissue Improves Morphology, Antigen and MRNA Preservation.,” Mod. Pathol., **18**(6), pp. 850–63.

[87] Tripathi, M., Bansal, R., Gupta, M., and Bharat, V., 2013, “Comparison of Routine Fixation of Tissues with Rapid Tissue Fixation,” J. Clin. Diagnostic Res., **7**(12), pp. 2768–2773.

[88] Shi, S. R., Shi, Y., and Taylor, C. R., 2011, “Antigen Retrieval Immunohistochemistry: Review and Future Prospects in Research and Diagnosis over Two Decades,” J. Histochem. Cytochem., **59**(1), pp. 13–32.

[89] Portiansky, E. L., and Gimeno, E. J., 1996, “A New Epitope Retrieval Method for the Detection of Structural Cytokeratins in the Bovine Prostatic Tissue,” Appl. Immunohistochem. Mol. Morphol., **4**(3), pp. 208–214.

[90] United States Food and Drug Administration Department of Health and Human Services, 2017, *Code of Federal Regulations Title 21, Section 880.5240: Medical Adhesive Tape and Adhesive Bandage*, 21CFR880.5240.

[91] van Schaik, R., and Rovekamp, M. H., 2011, “Fact or Myth? Pain Reduction in Solvent-Assisted Removal of Adhesive Tape,” J. Wound Care, **20**(8), pp. 380–383.

[92] McNichol, L., Lund, C., Rosen, T., and Gray, M., 2013, "Medical Adhesives and Patient Safety: State of the Science: Consensus Statements for the Assessment, Prevention, and Treatment of Adhesive-Related Skin Injuries," J. Dermatol. Nurses. Assoc., **5**(6), pp. 323–338.

[93] Zhao, H., He, Y., Huang, H., Ling, Y., Zhou, X., Wei, Q., Lei, Y., and Ying, Y., 2018, "Prevalence of Medical Adhesive-Related Skin Injury at Peripherally Inserted Central Catheter Insertion Site in Oncology Patients," J. Vasc. Access, **19**(1), pp. 23–27.

[94] Ratliff, C. R., 2017, "Descriptive Study of the Frequency of Medical Adhesive–Related Skin Injuries in a Vascular Clinic," J. Vasc. Nurs., **35**(2), pp. 86–89.

[95] Ousey, K., Cooper, K., Fumarola, S., and Hitchcock, J., 2017, "Findings from a Multidisciplinary Focus Group Meeting to Discuss the Issue of Medical Adhesive-Related Skin Injury (MARSI) in the UK: The Way Forward," Wounds UK, **13**(4), pp. 141–145.

[96] Wang, D., Xu, H., Chen, S., Lou, X., Tan, J., and Xu, Y., 2019, "Medical Adhesive-Related Skin Injuries and Associated Risk Factors in a Pediatric Intensive Care Unit," Adv. Ski. Wound Care, **32**(4), pp. 176–182.

[97] Farris, M. K., Petty, M., Hamilton, J., Walters, S.-A. A., and Flynn, M. A., 2015, "Medical Adhesive-Related Skin Injury Prevalence Among Adult Acute Care Patients," J. Wound, Ostomy Cont. Nurs., **42**(6), pp. 589–598.

[98] Ullman, A. J., Kleidon, T., Gibson, V., McBride, C. A., Mihala, G., Cooke, M., and Rickard, C. M., 2017, "Innovative Dressing and Securement of Tunneled Central Venous Access Devices in Pediatrics: A Pilot Randomized Controlled Trial," BMC Cancer, **17**(595).

[99] Taroc, A.-M., 2015, "Staying out of Sticky Situations: How to Choose the Right Tape for Your Patient," Wound Care Advis., **4**(6), pp. 21–26.

[100] Manriquez, S., Loperfido, B., and Smith, G., 2014, "Evaluation of a New Silicone Adhesive Tape among Clinicians Caring for Patients with Fragile or At-Risk Skin," Adv. Ski. Wound Care, **27**(4), pp. 163–170.

[101] Laulicht, B., Langer, R., and Karp, J. M., 2012, "Quick-Release Medical Tape," Proc. Natl. Acad. Sci., **109**(46), pp. 18803–18808.

[102] De Crevoisier, G., Fabre, P., Corpart, J. M., and Leibler, L., 1999, "Switchable Tackiness and Wettability of a Liquid Crystalline Polymer," Science (80-.)., **285**(5431), pp. 1246–

1249.

[103] Chivers, R. A., 2001, “Easy Removal of Pressure Sensitive Adhesives for Skin Applications,” Int. J. Adhes. Adhes., **21**(5), pp. 381–388.

[104] Kamperman, M., and Synytska, A., 2012, “Switchable Adhesion by Chemical Functionality and Topography,” J. Mater. Chem., **22**(37), pp. 19390–19401.

[105] Boyne, J. ., Millan, E. ., and Webster, I., 2001, “Peeling Performance of a Novel Light Switchable Pressure-Sensitive Adhesive,” Int. J. Adhes. Adhes., **21**(1), pp. 49–53.

[106] Clearweld, “Clearweld 900 Series Product Guide” [Online]. Available: http://www.clearweld.com/cms-assets/documents/Clearweld_900_Series_Coatings_Guide-web.pdf.

[107] Klein, R., 2012, *Laser Welding of Plastics: Materials, Processes and Industrial Applications*, John Wiley & Sons.

[108] Yarnitsky, D., Sprecher, E., Zaslansky, R., and Hemli, J. A., 1995, “Heat Pain Thresholds: Normative Data and Repeatability,” Pain, **60**(3), pp. 329–332.

[109] Martin, N. A., and Falder, S., 2017, “A Review of the Evidence for Threshold of Burn Injury,” Burns, **43**(8), pp. 1624–1639.

[110] Dewey, W. C., 2009, “Arrhenius Relationships from the Molecule and Cell to the Clinic,” Int. J. Hyperth., **25**(1), pp. 3–20.

[111] Diller, K. R., 2006, “Adapting Adult Scald Safety Standards to Children,” J. Burn Care Res., **27**(3), pp. 314–322.

[112] ASTM, 2010, *D3330/D330M: Standard Test Method for Peel Adhesion of Pressure-Sensitive Tape*.

[113] Okabe, T., Fujimura, T., Okajima, J., Aiba, S., and Maruyama, S., 2018, “Non-Invasive Measurement of Effective Thermal Conductivity of Human Skin with a Guard-Heated Thermistor Probe,” Int. J. Heat Mass Transf., **126**, pp. 625–635.

[114] Lumileds Holding B.V., “LUXEON IR Domed Line Specification Data” [Online]. Available: https://www.lumileds.com/uploads/685/DS191-pdf.

[115] Okada, T., Ishige, R., and Ando, S., 2016, “Analysis of Thermal Radiation Properties of Polyimide and Polymeric Materials Based on ATR-IR Spectroscopy,” J. Photopolym. Sci. Technol., **29**(2), pp. 251–254.

[116] Weinstein, S., and Hagle, M. E., 2014, *Plumer’s Principles & Practice of Infusion*

Therapy, Lippincott Williams & Wilkins, pp. 320-321.

[117] Henriques, F. C., 1947, "Studies of Thermal Injury V. The Predictability and the Significance of Thermally Induced Rate Processes Leading to Irreversible Epidermal Injury," Am. J. Pathol., **43**(5), pp. 489–502.

[118] ASTM C1055-99, 1999, *Standard Guide for Heated System Surface Conditions That Produce Contact Burn Injuries*, West Conshohocken, PA.

[119] Lim, S. D., Fauver, M. E., Svanevik, C. C., Nelson, L. Y., Taroc, A.-M., Emery, A. F., and Seibel, E. J., 2019, "Proof of Concept of a Surrogate High-Adhesion Medical Tape Using Photo-Thermal Release FOR RAPID and Less Painful Removal," J. Med. Device., (c).

VITA

Saniel D. Lim

Education

Ph.D. in Mechanical Engineering, University of Washington, Seattle, WA — June 2020
- Biomechanics Modeling GAANN Fellowship (2014, 2015, and 2016)
- Served as a co-instructor for Introduction to Biomechanics, and as a teaching assistant for Thermodynamics, Heat Transfer, and System Dynamics

M.S. in Mechanical Engineering, North Carolina State University, Raleigh, NC — May 2013
B.S. in Mechanical Engineering, Ajou University, Suwon, South Korea — February 2006

Publications

- ***Lim, S. D.***, Fauver, M. E., Svanevik, C. C., Nelson, L. Y., Taroc, A. M., Emery, A. F., & Seibel, E. J. (2019). Proof of Concept of a Surrogate High-adhesion Medical Tape Using Photo-thermal Release FOR RAPID and Less Painful Removal. Journal of Medical Devices.
- ***Lim, S. D.***, Huang, Q., & Seibel, E. J. (2019). Evaluation of Formalin Fixation for Tissue Biopsies Using Shear Wave Laser Speckle Imaging System. IEEE journal of translational engineering in health and medicine, 7, 1-10.
- Das, R., Burfeind, C. W., ***Lim, S. D.***, Patle, S., & Seibel, E. J. (2018, February). Pathology in a tube step 2: Simple rapid fabrication of curved circular cross section millifluidic channels for biopsy preparation/3D imaging towards pancreatic cancer detection and diagnosis. In Microfluidics, BioMEMS, and Medical Microsystems XVI (Vol. 10491, p. 1049118). International Society for Optics and Photonics.
- Taparia, N., Realmuto, J., ***Lim, S. D.***, Canton G., & Borgford-Parnell J., Cooperative Teaching as an Effective Training Mechanism for Future Instructors, in 2017 PNW ASEE Conference: Teaching for Inclusion: Diversity in the Classroom and Beyond, 2017.
- Das, R., Nguyen, T. M., ***Lim, S. D.***, O'Donnell, M., Wang, R. K., & Seibel, E. J. (2014, October). Feasibility of a hybrid elastographic-microfluidic device to rapidly process and assess pancreatic cancer biopsies for pathologists. In 2014 IEEE Healthcare Innovation Conference (HIC) (pp. 271-275). IEEE.
- ***Lim, S. D.***, Mazzoleni, A. P., Park, J. K., Ro, P. I., & Quinlan, B. (2013). Conceptual design of ocean compressed air energy storage system. Marine Technology Society Journal, 47(2), 70-81.
- Park, J. K., Ro, P. I., ***Lim, S. D.***, Mazzoleni, A. P., & Quinlan, B. (2012, October). Analysis and optimization of a quasi-isothermal compression and expansion cycle for ocean compressed air energy storage (OCAES). In 2012 Oceans (pp. 1-8). IEEE.